

Super*B* Progress Reports

Physics
Accelerator
Detector
Computing

June 30, 2010

Abstract

This report describes the present status of the detector design for Super*B*. It is one of four separate progress reports that, taken collectively, describe progress made on the Super*B* Project since the publication of the Super*B* Conceptual Design Report in 2007 and the Proceedings of Super*B* Workshop VI in Valencia in 2008.

E. Grauges,
Universitat De Barcelona, Fac. Fisica. Dept. ECM Barcelona E-08028, Spain

G. Donvito, V. Spinoso
INFN Bari and Università di Bari, Dipartimento di Fisica, I-70126 Bari, Italy

M. Manghisoni, V. Re, G. Traversi
INFN Pavia and Università di Bergamo Dipartimento di Ingegneria Industriale, I-24129 Bergamo, Italy

G. Eigen, D. Fehlker, L. Helleve
University of Bergen, Institute of Physics, N-5007 Bergen, Norway

A. Carbone, R. Di Sipio, A. Gabrielli, D. Galli, F. Giorgi, U. Marconi, S. Perazzini, C. Sbarra,
V. Vagnoni, S. Valentinetti, M. Villa, A. Zoccoli
INFN Bologna and Università di Bologna, Dipartimento di Fisica, I-40127 Bologna, Italy

C. Cheng, A. Chivukula, D. Doll, B. Echenard, D. Hitlin, P. Ongmongkolkul, F. Porter,
A. Rakitin, M. Thomas, R. Zhu
California Institute of Technology, Pasadena, California 91125, USA

G. Tatishvili
Carleton University, Ottawa, Ontario, Canada K1S 5B6

R. Andreassen, C. Fabby, B. Meadows, A. Simpson, M. Sokoloff, K. Tomko
University of Cincinnati, Cincinnati, Ohio 45221, USA

A. Fella
INFN CNAF I-40127 Bologna, Italy

M. Andreotti, W. Baldini, R. Calabrese, V. Carassiti, G. Cibinetto, A. Cotta Ramusino,
A. Gianoli, E. Luppi, M. Munerato, V. Santoro, L. Tomassetti
INFN Ferrara and Università di Ferrara, Dipartimento di Fisica, I-44100 Ferrara, Italy

D. Stoker
University of California, Irvine Irvine, California 92697, USA

O. Bezshyyko, G. Dolinska
Taras Shevchenko National University of Kyiv Kyiv, 01601, Ukraine

N. Arnaud, C. Beigbeder, F. Bogard, D. Breton, L. Burmistrov, D. Charlet, J. Maalmi,
L. Perez Perez, V. Puill, A. Stocchi, V. Tocut, S. Wallon, G. Wormser
Laboratoire de l'Accélérateur Linéaire, IN2P3/CNRS, Université Paris-Sud 11, F-91898 Orsay, France

D. Brown
Lawrence Berkeley National Laboratory, University of California, Berkeley, California 94720, USA

A. Calcaterra, R. de Sangro, G. Felici, G. Finocchiaro, P. Patteri, I. Peruzzi, M. Piccolo,
M. Rama

Laboratori Nazionali di Frascati dell'INFN, I-00044 Frascati, Italy

S. Fantinel, G. Maron

Laboratori Nazionali di Legnaro dell'INFN, I-35020 Legnaro, Italy

E. Ben-Haim, G. Calderini, H. Lebbolo, G. Marchiori

**Laboratoire de Physique Nucléaire et de Hautes Energies, IN2P3/CNRS, Université
Pierre et Marie Curie-Paris 6, F-75005 Paris, France**

R. Cenci, A. Jawahery, D.A. Roberts

University of Maryland, College Park, Maryland 20742, USA

D. Lindemann, P. Patel, S. Robertson, D. Swersky

McGill University, Montréal, Québec, Canada H3A 2T8

P. Biassoni, M. Citterio, V. Liberali, F. Palombo, A. Stabile, S. Stracka

INFN Milano and Università di Milano, Dipartimento di Fisica, I-20133 Milano, Italy

A. Aloisio, S. Cavaliere, G. De Nardo, A. Doria, R. Giordano, A. Ordine, S. Pardi, G. Russo,
C. Sciacca

**INFN Napoli and Università di Napoli Federico II, Dipartimento di Scienze Fisiche,
I-80126, Napoli, Italy**

A.Y. Barniakov, M.Y. Barniakov, V.E. Blinov, V.P. Druzhinin, V.B. Golubev, S.A. Kononov,
E. Kravchenko, A.P. Onuchin, S.I. Serednyakov, Y.I. Skovpen, E.P. Solodov

Budker Institute of Nuclear Physics, Novosibirsk 630090, Russia

M. Bellato, M. Benettoni, M. Corvo, A. Crescente, F. Dal Corso, C. Fanin, E. Feltresi,

N. Gagliardi, M. Morandin, M. Posocco, M. Rotondo, R. Stroili

INFN Padova and Università di Padova, Dipartimento di Fisica, I-35131 Padova, Italy

C. Andreoli, L. Gaioni, E. Pozzati, L. Ratti, V. Speziali

INFN Pavia and Università di Pavia, Dipartimento di Elettronica, I-27100 Pavia, Italy

D. Aisa, M. Bizzarri, C. Cecchi, S. Germani, P. Lubrano, E. Manoni, A. Papi, A. Piluso, A. Rossi

INFN Perugia and Università di Perugia, Dipartimento di Fisica, I-06123 Perugia, Italy

M. Lebeau

INFN Perugia, I-06123 Perugia, Italy, and

California Institute of Technology, Pasadena, California 91125, USA

C. Avanzini, G. Batignani, S. Bettarini, F. Bosi, M. Ceccanti, A. Cervelli, A. Ciampa,
F. Crescioli, M. Dell'Orso, D. Fabiani, F. Forti, P. Giannetti, M. Giorgi, S. Gregucci, A. Lusiani,
P. Mammini, G. Marchiori, M. Massa, E. Mazzoni, F. Morsani, N. Neri, E. Paoloni, E. Paoloni,
M. Piendibene, A. Profeti, G. Rizzo, L. Sartori, J. Walsh, E. Yurtsev

**INFN Pisa, Università di Pisa, Dipartimento di Fisica, and Scuola Normale Superiore,
I-56127 Pisa, Italy**

D.M. Asner, J. E. Fast, R.T. Kouzes,
Pacific Northwest National Laboratory, *Richland, Washington 99352, USA*

A. Bevan, F. Gannaway, J. Mistry, C. Walker
Queen Mary, *University of London, London E1 4NS, United Kingdom*

C.A.J. Brew, R.E. Coath, J.P. Crooks, R.M. Harper, A. Lintern, A. Nichols, M. Staniztki,
R. Turchetta, F.F. Wilson
Rutherford Appleton Laboratory, *Chilton, Didcot, Oxon, OX11 0QX, United Kingdom*

V. Bocci, G. Chiodi, R. Faccini, C. Gargiulo, D. Pinci, L. Recchia, D. Ruggieri
INFN Roma and Università di Roma La Sapienza, *Dipartimento di Fisica, I-00185 Roma, Italy*

A. Di Simone
INFN Roma Tor Vergata and Università di Roma Tor Vergata, *Dipartimento di Fisica, I-00133 Roma, Italy*

P. Branchini, A. Passeri, F. Ruggieri, E. Spiriti
INFN Roma Tre and Università di Roma Tre, *Dipartimento di Fisica, I-00154 Roma, Italy*

D. Aston, M. Convery, G. Dubois-Felsmann, W. Dunwoodie, M. Kelsey, P. Kim, M. Kocian,
D. Leith, S. Luitz, D. MacFarlane, B. Ratcliff, M. Sullivan, J. Va'vra, W. Wisniewski, W. Yang
SLAC National Accelerator Laboratory *Stanford, California 94309, USA*

K. Shougaev, A. Soffer
School of Physics and Astronomy, Tel Aviv University *Tel Aviv 69978, Israel*

F. Bianchi, D. Gamba, G. Giraud, P. Mereu
INFN Torino and Università di Torino, *Dipartimento di Fisica Sperimentale, I-10125 Torino, Italy*

G. Dalla Betta, G. Fontana, G. Soncini
INFN Padova and Università di Trento, *ICT Department, I-38050 Trento, Italy*

M. Bomben, L. Bosisio, P. Cristaudo, G. Giacomini, D. Jugovaz, L. Lanceri, I. Rashevskaya,
G. Venier, L. Vitale
INFN Trieste and Università di Trieste, *Dipartimento di Fisica, I-34127 Trieste, Italy*

R. Henderson
TRIUMF *Vancouver, British Columbia, Canada V6T 2A3*

J.-F. Caron, C. Hearty, P. Lu, R. So
University of British Columbia, *Vancouver, British Columbia, Canada V6T 1Z1*

P. Taras
Université de Montréal, *Physique des Particules, Montréal, Québec, Canada H3C 3J7*

A. Agarwal, J. Franta, J.M. Roney
University of Victoria, *Victoria, British Columbia, Canada V8W 3P6*

Contents

1	Introduction	1
1.1	The Physics Motivation	1
1.2	The Super <i>B</i> Project Elements	1
1.3	The Detector Design Progress Report	2
2	Overview	3
2.1	Physics Performance	3
2.2	Challenges on Detector Design	6
2.3	Open Issues	7
2.4	Detector R&D	8
3	Silicon Vertex Tracker	10
3.1	Detector Concept	10
3.1.1	SVT and Layer0	10
3.1.2	Performance Studies	10
3.1.3	Background Conditions	12
3.2	Layer0 Options Under Study	13
3.2.1	Triplets	13
3.2.2	Hybrid Pixels	14
3.2.3	MAPS	14
3.2.4	Pixel Module Integration	15
3.3	A MAPS-based All-pixel SVT Using a Deep P-well Process	16
3.4	R&D Activities	17
4	Drift Chamber	20
4.1	Backgrounds	20
4.2	Drift Chamber Geometry	21
4.3	Mechanical Structure	21
4.4	Gas Mixture	22
4.5	Cell Design and Layout	22
4.6	R&D Work	23
5	Particle Identification	25
5.1	Detector Concept	25
5.1.1	Charged Particle Identification at Super <i>B</i>	25
5.1.2	<i>BABAR</i> DIRC	25
5.2	Barrel PID at Super <i>B</i>	26
5.2.1	Performance Optimization	26
5.2.2	Design and R&D Status	28
5.3	Forward PID at Super <i>B</i>	29
5.3.1	Motivation for a Forward PID Detector	29
5.3.2	Forward PID Requirements	31
5.3.3	Status of the Forward PID R&D Effort	31
6	Electromagnetic Calorimeter	34
6.1	Barrel Calorimeter	34

6.2	Forward Endcap Calorimeter	35
6.2.1	Mechanical Structure	36
6.2.2	Readout System	36
6.2.3	Calibration and Beam Test	36
6.2.4	Performance Studies	36
6.3	Backward Endcap Calorimeter	38
6.4	R&D	40
6.4.1	Barrel Calorimeter	40
6.4.2	Forward Calorimeter	40
6.4.3	Backward Calorimeter	40
7	Instrumented Flux Return	42
7.1	Performance Optimization	42
7.1.1	Identification Technique	42
7.1.2	Baseline Design Requirements	42
7.1.3	Design Optimization and Performance Studies	43
7.2	R&D Work	44
7.2.1	R&D Tests and Results	44
7.2.2	Prototype	45
7.3	Baseline Detector Design	46
7.3.1	Flux Return	46
8	Electronics, Trigger, DAQ and Online	48
8.1	Overview of the Architecture	48
8.1.1	Trigger Strategy	48
8.1.2	Trigger Rates and Event Size Estimation	49
8.1.3	Dead Time and Buffer Queue Depth Considerations	49
8.2	Electronics, Trigger and DAQ	50
8.2.1	Fast Control and Timing System	51
8.2.2	Clock, Control and Data Links	52
8.2.3	Common Front-End Electronics	53
8.2.4	Readout Module	53
8.2.5	Experiment Control System	54
8.2.6	Level 1 Hardware Trigger	55
8.3	Online System	56
8.3.1	ROM Readout and Event Building	56
8.3.2	High Level Trigger Farm	57
8.3.3	Data Logging	57
8.3.4	Event Data Quality Monitoring and Display	57
8.3.5	Run Control System	57
8.3.6	Detector Control System	57
8.3.7	Other Components	58
8.3.8	Software Infrastructure	58
8.4	Front-End Electronics	58
8.4.1	SVT Electronics	58
8.4.2	DCH Electronics:	59
8.4.3	PID Electronics:	60
8.4.4	EMC Electronics:	61

8.4.5	IFR Electronics:	63
8.5	R&D	63
8.6	Conclusions	64
9	Software and Computing	66
9.1	The Super <i>B</i> baseline model	66
9.1.1	The requirements	67
9.1.2	Super <i>B</i> offline computing development	67
9.2	Computing tools and services for the Detector and Physics TDR studies	68
9.2.1	Fast simulation	68
9.2.2	Bruno: the Super <i>B</i> full simulation tool	71
9.2.3	The distributed production environment	72
9.2.4	The software development and collaborative tools	75
9.2.5	Code packaging and distribution	76
10	Mechanical Integration	77
10.1	Introduction	77
10.1.1	Magnet and Instrumented Flux Return	77
10.2	Component Extraction	78
10.3	Component Transport	79
10.4	Detector Assembly	80
11	Budget and Schedule	81
11.1	Detector Costs	81
11.2	Basis of Estimate	85
11.3	Schedule	86

1 Introduction

1.1 The Physics Motivation

The Standard Model successfully explains the wide variety of experimental data that has been gathered over several decades with energies ranging from under a GeV up to several hundred GeV. At the start of the millennium, the flavor sector was perhaps less explored than the gauge sector, but the PEP-II and KEK-B asymmetric B Factories, and their associated experiments *BABAR* and *Belle*, have produced a wealth of important flavor physics highlights during the past decade [1]. The most notable experimental objective, the establishment of the Cabibbo-Kobayashi-Maskawa phase as consistent with experimentally observed CP-violating asymmetries in *B* meson decay, was cited in the award of the 2008 Nobel Prize to Kobayashi & Maskawa [2].

The B Factories have provided a set of unique, over-constrained tests of the Unitarity Triangle. These have, in the main, been found to be consistent with Standard Model predictions. The B factories have done far more physics than originally envisioned; *BABAR* alone has published more than 400 papers in refereed journals to date. Measurements of all three angles of the Unitarity Triangle – α and γ , in addition to $\sin 2\beta$; the establishment of $D^0\bar{D}^0$ mixing; the uncovering of intriguing clues for potential New Physics in $B \rightarrow K^{(*)}l^+l^-$ and $B \rightarrow K\pi$ decays; and unveiling an entirely unexpected new spectroscopy, are some examples of important experimental results beyond those initially contemplated.

With the LHC now beginning operations, the major experimental discoveries of the next few years will probably be at the energy frontier, where we would hope not only to complete the Standard Model by observing the Higgs particle, but to find signals of New Physics which are widely expected to lie around the 1 TeV energy scale. If found, the New Physics phenomena will need data from very sensitive heavy fla-

vor experiments if they are to be understood in detail. Determining the flavor structure of the New Physics involved requires the information on rare b, c and τ decays, and on CP violation in b and c quark decays that only a very high luminosity asymmetric B Factory can provide [3]. On the other hand, if such signatures of New Physics are not observed at the LHC, then the excellent sensitivity provided at the luminosity frontier by a next generation super B-factory provides another avenue to observing New Physics at mass scales up to 10 TeV or more through observation of rare processes involving *B* and *D* mesons and studies of lepton flavour violation (LFV) in τ decays.

1.2 The SuperB Project Elements

It is generally agreed that the physics being addressed by a next-generation B factory requires a data sample that is some 50–100 times larger than the existing combined sample from *BABAR* and *Belle*, or at least 50–75 ab^{-1} . Acquiring such an integrated luminosity in a 5 year time frame requires that the collider run at a luminosity of at least $10^{36} \text{ cm}^{-2}\text{s}^{-1}$.

For a number of years, an Italian led, INFN hosted, collaboration of scientists from Canada, Italy, Israel, France, Norway, Spain, Poland, UK and USA have worked together to design and propose a high luminosity 10^{36} asymmetric B Factory project, called *SuperB*, to be built at or near the Frascati laboratory [4]. The project, which is managed by a project board, includes divisions for the accelerator, the detector, the computing, and the site & facilities.

The accelerator portion of the project employs lessons learned from modern low-emittance synchrotron light sources and ILC/CLIC R&D, and an innovative new idea for the intersection region of the storage rings [5], called crab waist, to reach luminosities over 50 times greater than those obtained by earlier B factories at KEK and SLAC. There is now an attractive, cost-effective accelerator design, including polarized beams, which is being further refined and optimized [6]. It is designed to incorporate many PEP-II

components. This facility promises to deliver fundamental discovery-level science at the luminosity frontier.

There is also an active international proto-collaboration working effectively on the design of the detector. The detector team draws heavily on its deep experience with the *BABAR* detector, which has performed in an outstanding manner both in terms of scientific productivity and operational efficiency. *BABAR* serves as the foundation of the design of the Super*B* detector.

To date, the Super*B* project has been very favorably reviewed by several international committees. This international community now awaits a decision by the Italian government on its support of the project.

1.3 The Detector Design Progress Report

This document describes the design and development of the Super*B* detector, which is based on a major upgrade of *BABAR*. This is one of several descriptive “Design Progress Reports (DPR)” being produced by the Super*B* project during the first part of 2010 to motivate and summarize the development, and present the status of each major division of the project (Physics, Accelerator, Detector, and Computing) so as to present a snapshot of the entire project at an intermediate stage between the CDR, which was written in 2007, and the TDR that is being developed during the next year.

This “Detector DPR” begins with a brief overview of the detector design, the challenges involved in detector operations at the luminosity frontier, the approach being taken to opti-

mize the remaining general design choices, and the R&D program that is underway to develop and validate the system and subsystem designs. Each of the detector subsystems and the general detector systems are then described in more detail, followed by a description of the integration and assembly of the full detector. Finally, the paper concludes with a discussion of detector costs and a schedule overview.

References

- [1] C. Amsler *et al.* (Particle Data Group), *Phys. Lett. B* **667**, 1 (2008).
- [2] http://nobelprize.org/nobel_prizes/physics/laureates/2008/press.html; and <http://www-public.slac.stanford.edu/babar/Nobel2008.htm>.
- [3] D. Hitlin *et al.*, *Proceedings of SuperB Workshop VI: New Physics at the Super Flavor Factory*, arXiv:0810.1312v2 [hep-ph].
- [4] M. Bona *et al.*, *SuperB: A High-Luminosity Heavy Flavour Factory. Conceptual Design Report*, arXiv:0709.0451v2 [hep-ex], INFN/AE-07/2, SLAC-R-856, LAL 07-15, also available at <http://www.pi.infn.it/SuperB/CDR>.
- [5] P. Raimondi in *2nd LNF Workshop on SuperB*, Frascati, Italy, March 16-18 2006 <http://www.lnf.infn.it/conference/superb06/>; and in *Proceedings of Particle Accelerator Conference (PAC 07)*, Albuquerque, New Mexico, USA, June 25-29, 32 (2007).
- [6] *Design Progress Report for the SuperB Accelerator*, (2010), in preparation.

2 Overview

The Super*B* detector concept is based on the *BABAR* detector, with those modifications required to operate at a luminosity of 10^{36} or more, and with a reduced center-of-mass boost. Further improvements needed to cope with higher beam-beam and other beam-related backgrounds, as well as to improve detector hermeticity and performance, are also discussed, as is the necessary R&D required to implement this upgrade. Cost estimates and the schedule are described in Section 11.

The current *BABAR* detector consists of a tracking system with a five layer double-sided silicon strip vertex tracker (SVT) and a 40 layer drift chamber (DCH) inside a 1.5T magnetic field, a Cherenkov detector with fused silica bar radiators (DIRC), an electromagnetic calorimeter (EMC) consisting of 6580 CsI(Tl) crystals and an instrumented flux-return (IFR) comprised of both limited streamer tube (LST) and resistive plate chamber (RPC) detectors for K_L^0 detection and μ identification.

The Super*B* detector concept reuses a number of components from *BABAR*: the flux-return steel, the superconducting coil, the barrel of the EMC and the fused silica bars of the DIRC. The flux-return will be augmented with additional absorber to increase the number of interaction lengths for muons to roughly 7λ . The DIRC camera will be replaced by a twelve-fold modular camera using multi-channel plate (MCP) photon detectors in a focusing configuration using fused silica optics to reduce the impact of beam related backgrounds and improve performance. The forward EMC will feature cerium-doped LYSO (lutetium yttrium orthosilicate) crystals, which have a much shorter scintillation time constant, a lower Molière radius and better radiation hardness than the current CsI(Tl) crystals, again for reduced sensitivity to beam backgrounds and better position resolution.

The tracking detectors for Super*B* will be new. The current SVT cannot operate at $\mathcal{L} = 10^{36}$, and the DCH has reached the end of its

design lifetime and must be replaced. To maintain sufficient proper-time difference (Δt) resolution for time-dependent *CP* violation measurements with the Super*B* boost of $\beta\gamma = 0.24$, the vertex resolution will be improved by reducing the radius of the beam pipe, placing the innermost layer of the SVT at a radius of roughly 1.2 cm. This innermost layer of the SVT will be constructed of either silicon stripsets or Monolithic Active Pixel Sensors (MAPS) or other pixelated sensors, depending on the estimated occupancy from beam-related backgrounds. Likewise, the design of the cell size and geometry of the DCH will be driven by occupancy considerations. The hermeticity of the Super*B* detector, and, thus, its performance for certain physics channels will be improved by including a backwards “veto-quality” EMC detector comprising a lead-scintillator stack. The physics benefit from the inclusion of a forward PID remains under study. The baseline design concept is a fast Cherenkov light based time-of-flight system.

The Super*B* detector concept is shown in Fig. 1., The top portion of this elevation view shows the minimal set of new detector components, with substantial reuse of elements of the current *BABAR* detector; the bottom half shows a configuration with additional new components that would cope with higher beam backgrounds and achieve greater hermeticity.

2.1 Physics Performance

The Super*B* detector design, as described in the Conceptual Design Report [1], left open a number of issues that have a large impact on the overall detector geometry. These include the physics impact of a PID device in front of the forward EMC; the need for an EMC in the backward region; the position of the innermost layer of the SVT; the SVT internal geometry and the SVT-DCH transition radius; and the amount and distribution of absorber in the IFR.

These issues have been addressed by evaluating the performance of different detector configurations in reconstructing charged and neutral particles as well as the overall sensitivity of each

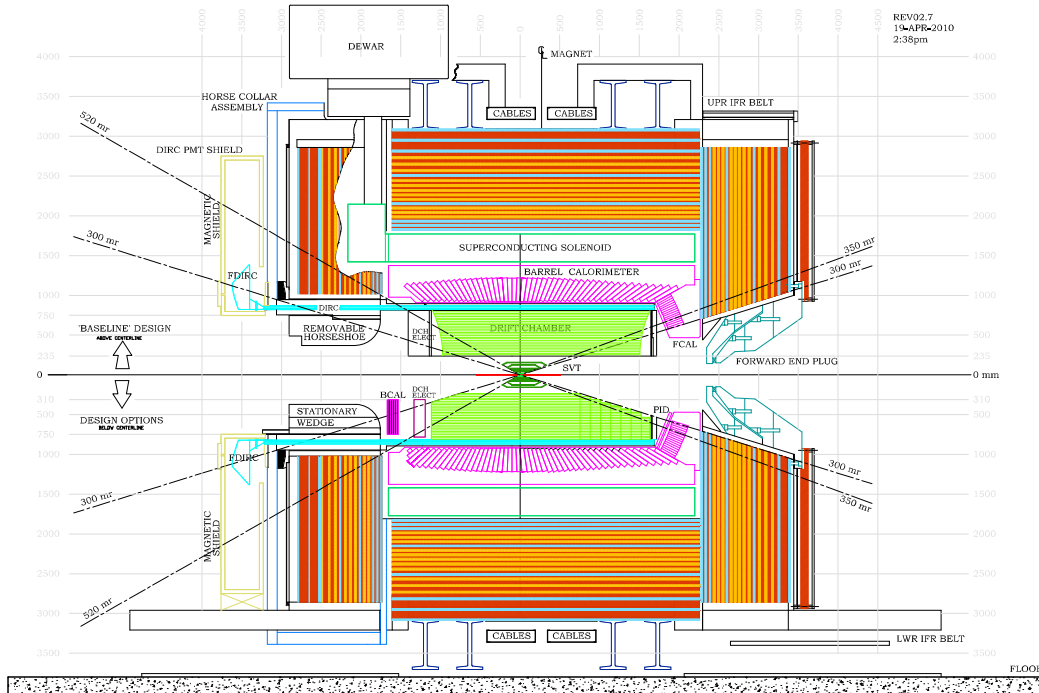


Figure 1: Concept for the Super B detector. The upper half shows the baseline concept, and the bottom half adds a number of optional detector configurations.

configuration to a set of benchmark decay channels. To accomplish this task, a fast simulation code specifically developed for the Super B detector has been used (see Section 9), combined with a complete set of analysis tools inherited, for the most part, from the $BABAR$ experiment. Geant4-based code has been used to simulate the primary sources of backgrounds – including both machine-induced and physics processes – in order to estimate the rates and occupancies of various sub-detectors as a function of position. The main results from these ongoing studies are summarized in this section.

Time-dependent measurements are an important part of the Super B physics program. In order to achieve a Δt resolution comparable to that at $BABAR$, the reduced boost at Su-

per B must be compensated by improving the vertex resolution. This requires a thin beam pipe plus SVT Layer0 that is placed as close as possible to the IP. The main factor limiting the minimum radius of Layer0 is the hit rate from $e^+e^- \rightarrow e^+e^-e^+e^-$ background events. Two candidate detector technologies with appropriate characteristics, especially in radiation length (X_0) and hit resolution, for application in Layer0 are (1) a hybrid pixel detector with 1.08% X_0 , and 14 μm hit resolution, and (2) striplets with 0.40% X_0 and 8 μm hit resolution. Simulation studies of $B^0 \rightarrow \phi K_S^0$ decays have shown that with a boost of $\beta\gamma = 0.28$ the hybrid pixels (the striplets) reach a $\sin 2\beta_{\text{eff}}$ per event error equal to $BABAR$ at an inner radius of 1.5 cm (2.0 cm). With $\beta\gamma = 0.24$ the error in-

creases by 7–8%. Similar conclusions also apply to $B^0 \rightarrow \pi^+\pi^-$ decays.

The *BABAR* SVT five-layer design was motivated both by the need for standalone tracking for low- p_T tracks as well as the need for redundancy in case several modules failed during operation. The default Super*B* SVT design, consisting of a *BABAR*-like SVT detector and an additional Layer0, has been compared with two alternative configurations with a total of either five or four layers. These simulation studies, which used the decay $B \rightarrow D^*K$ as the benchmark channel, focused on the impact of the detector configuration on track quality as well as on the reconstruction efficiency for low p_T tracks. The studies have shown that, as expected, the low- p_T tracking efficiency is significantly decreased for configurations with reduced numbers of SVT layers, while the track quality is basically unaffected. Given the importance of low momentum tracking efficiency for the Super*B* physics program, these results support a six-layer layout.

Studies have also shown that the best overall SVT+DCH tracking performance is achieved if the outer radius of the SVT is kept small (14 cm as in *BABAR* or even less) and the inner wall of the DCH is as close to the SVT as possible. However, as some space between the SVT and DCH is needed for the cryostats that contain the super-conducting magnets in the interaction region, the minimum DCH inner radius is expected to be about 20–25 cm.

The impact of a forward PID device is estimated using benchmark modes such as $B \rightarrow K^{(*)}\nu\bar{\nu}$, balancing the advantage of having better PID information in the forward region with the drawbacks arising from more material in front of the EMC and a slightly shorter DCH. Three detector configurations have been compared in these simulation studies: *BABAR*, the Super*B* baseline (no forward PID device), and a configuration that includes a time-of-flight (TOF) detector between the DCH and the forward EMC. The results, presented in terms of $S/\sqrt{S+B}$, for the decay mode $B \rightarrow K\nu\bar{\nu}$ with the tag side reconstructed in the semileptonic modes, are shown in Fig. 2. In summary, while

the default Super*B* design leads to an improvement of about 7-8% in $S/\sqrt{S+B}$, primarily due to the reduced boost in Super*B* the configuration with the forward TOF provides an additional 5-6% improved sensitivity for this channel. Machine backgrounds have yet to be included in these simulations, but will be considered in our next updates.

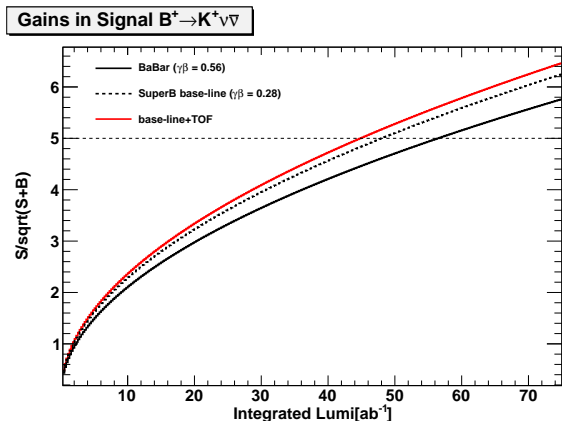


Figure 2: $S/\sqrt{S+B}$ of $B \rightarrow K\nu\bar{\nu}$ as a function of the integrated luminosity in three different detector configurations.

The backward calorimeter under consideration is designed to be used in veto mode. Its impact on physics can be estimated by studying the sensitivity of rare B decays with one or more neutrinos in the final state, which benefit from having more hermetic detection of neutrals to reduce the background contamination. One of the most important benchmark channels of this kind is $B \rightarrow \tau\nu$. Preliminary studies, not including the machine backgrounds, indicate that, when the backward calorimeter is installed, the statistical precision $S/\sqrt{S+B}$ is enhanced by about 8%. The results are summarized in Fig. 3. The top plot shows how $S/\sqrt{S+B}$ changes as a function of the cut on E_{extra} (the total energy of charged and neutral particles that cannot be directly associated with the reconstructed daughters of the signal or tag B) with or without the backward EMC. The signal is peaked at zero. The bottom plot shows the ratio of $S/\sqrt{S+B}$ for detector configurations with and without a backward EMC, again as a function of the E_{extra}

cut. This analysis will be repeated soon, including the main sources of machine backgrounds, which could affect the E_{extra} distributions significantly. The possibility of using the backward calorimeter as a PID time-of-flight device is also under study.

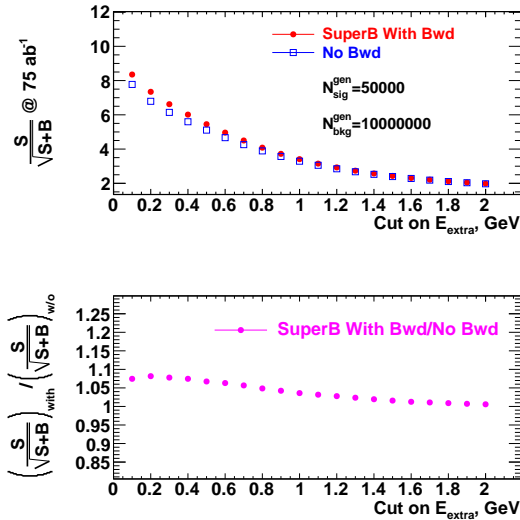


Figure 3: Top: $S/\sqrt{S+B}$ as a function of the cut on E_{extra} with (circles) and without (squares) the backward EMC. Bottom: ratio of $S/\sqrt{S+B}$ for detector configurations with or without a backward EMC as a function of the E_{extra} cut.

The presence of a forward PID or backward EMC affects the maximum extension of the DCH and therefore the tracking and dE/dx performance in those regions. The impact of a TOF PID detector is practically negligible because it only takes a few centimeters from the DCH. On the other hand, the effect of a forward RICH device (~ 20 cm DCH length reduction) or the backward EMC (~ 30 cm) is somewhat larger. For example, for tracks with polar angles $< 23^\circ$ and $> 150^\circ$, there is an increase in σ_p/p of 25% and 35%, respectively. Even in this case, however, the overall impact on the physics is generally quite limited because only a small fraction of tracks cross the extreme forward and backward regions.

The IFR system will be upgraded by replacing the *BABAR* RPCs and LSTs with layers of much faster extruded plastic scintillator coupled to WLS fibers read out by APDs operated in Geiger mode. The identification of muons and K_L^0 is optimized with a Geant4 simulation by tuning the amount of iron absorber and the distribution of the active detector layers. The current baseline design has a total iron thickness of 92 cm interspersed with eight layers of scintillator. Preliminary estimates indicate a muon efficiency larger than 90% for $p > 1.5 \text{ GeV}/c$ at a pion misidentification rate of about 2%.

2.2 Challenges on Detector Design

Machine background is one of the leading challenges of the SuperB project: each subsystem must be designed so that its performance is minimally degraded because of the occupancy produced by background hits. Moreover, the detectors must be protected against deterioration arising from radiation damage. In effect, what is required is that each detector perform as well or better than *BABAR* with similar operational lifetimes, but for two orders of magnitude higher luminosity.

Background particles produced by beam gas scattering and by the synchrotron radiation near the interaction point (IP) are expected to be manageable since the relevant SuperB design parameters (mainly the beam current) are fairly close to those in PEP-II.

Touschek backgrounds are expected to be larger than in *BABAR* because of the extremely low design emittances of the SuperB beams. Preliminary simulation studies indicate that a system of beam collimators upstream of the IP can reduce particle losses to tolerable levels.

The main source of concern arises from the background particles produced at the IP by QED processes whose cross section is $\sim 200 \text{ mb}$ corresponding at the nominal SuperB luminosity to a rate of $\sim 200 \text{ GHz}$. Of particular concern is the radiative Bhabha reaction (i.e.: $e^+e^- \rightarrow e^+e^-\gamma$), where one of the incoming beam particles loses a significant fraction of its

energy by the emission of a photon. Both the photon and the radiating beam particles emerge from the IP traveling almost collinearly with respect to the beam-line. The magnetic elements downstream of the IP over-steer these primary particles into the vacuum chamber walls producing electro-magnetic showers, whose final products are the background particles seen by the subsystems. The particles of these electromagnetic showers can also excite the giant nuclear resonances in the material around the beam line expelling neutrons from the nucleus. Careful optimization of the mechanical apertures of the vacuum chambers and the optical elements is needed to keep a large stay-clear for the off-energy primary particles, hence reducing the background rate.

A preliminary Geant4-based Monte Carlo simulation study of this process at SuperB indicates that a shield around the beamline will be required to keep the electrons, positrons, photons and neutrons away from the detector, reducing occupancies and radiation damage to tolerable levels.

The “quasi-elastic Bhabha” process has also been considered. The cross section for producing a primary particle reconstructed by the detector via this process is ~ 100 nb corresponding to a rate of about 100 kHz. It is reasonable to assume that this will be the driving term for the level one trigger rate. Single beam contributions to the trigger rate are, in fact, expected to be of the same order as in *BABAR*, given that the nominal beam currents and other relevant design parameter are comparable.

A final luminosity related background effect is the production of electron-positron pairs at the IP by the two photon process $e^+e^- \rightarrow e^+e^-e^+e^-$, whose total cross section evaluated at leading order with the Monte Carlo generator DIAG36 [2] is 7.3 mb corresponding, at nominal luminosity, to a rate of 7.3 GHz. The pairs produced by this process are characterized by very soft transverse momenta particles. The solenoidal magnetic field in the tracking volume confines most of these background particles inside the beam pipe. Those articles having a transverse momentum large enough to reach the

beam pipe ($p_T > 2.5$ MeV/c) and with a polar angle inside the Layer0 acceptance are produced at a rate of ~ 0.5 GHz. This background will be a driving factor in the design of the segmentation and the read-out architecture for SVT Layer0. The background track surface rate on the SVT Layer0 as a function of its radius is shown in Fig. 4.

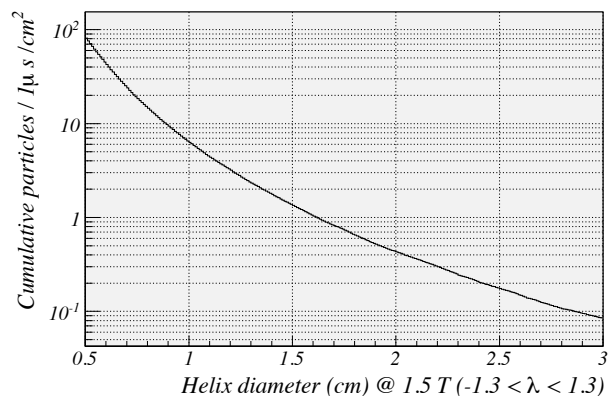


Figure 4: Pairs background track rate per unit surface as a function of the SVT Layer0 radius. Multiple track hits have not been taken into account.

An effort to improve the simulation of these background sources with a Geant4 based code is underway at present. A fairly accurate model of the detector and beam-line elements is available to the collaboration. Several configurations have been simulated and studied, providing some guidelines to the detector and machine teams. Further refinements of the interaction region and detector design will require development of the Geant4 background simulation tools on the detector response side.

2.3 Open Issues

The basic geometry, structure and physics performance of the SuperB detector is mainly predetermined by the retention of the solenoidal magnet, return steel, and the support structure from the *BABAR* detector, and a number of its largest, and most expensive, subsystems. Even though this fixes both the basic geometry,

and much of the physics performance, it does not really constrain the expected performance of the Super B detector in any important respect. *BABAR* was already an optimized B-factory detector for physics, and any improvements in performance that could come from changing the overall layout or rebuilding the large subsystems would be modest overall. The primary challenge for Super B is to retain physics performance similar to *BABAR* in the higher background environment described in Section 2.2, while operating at much higher ($\sim \times 50$) data taking rates.

Within these constraints, optimization of the geometrical layout and new detector elements for the most important physics channels remains of substantial interest. The primary tools for sorting through the options are: (1) simulation, performed under the auspices of a “Detector Geometry Working Group” (DGWG), that studies basic tracking, PID, and neutrals performance of different detector configurations, including their impact on each other, and studies the physics reach of a number of benchmark channels; and (2) detector R&D, including prototyping, developing new subsystem technologies, and understanding the costs, and robustness of systems, as well as their impacts on each other. The first item, discussed in Section 2.1, clearly provides guidance to the second, as discussed in Section 2.4 and the subsystem chapters which follow, and vice versa.

At the level of the overall detector, the immediate task is to define the sub-detector envelopes. Optimization can and will continue for some time yet within each sub-detector system. The studies performed to date leave us with the default detector proposal, with only a few open options remaining at the level of the detector geometry envelopes and technology choices. These open issues are: (1) whether there is a forward PID detector, and, if so, at what z location does the DCH end and the EMC begin; and (2) whether there is a backward EMC. These open issues are expected to be resolved by the Technical Board within the next few months following further studies by the DGWG, in collaboration with the relevant system groups.

2.4 Detector R&D

The Super B detector concept rests, for the most part, on well validated basic detector technology. Nonetheless, each of the sub-detectors has many challenges due to the high rates and demanding performance requirements with R&D initiatives ongoing in all detector systems to improve the specific performance, and optimize the overall detector design. These are described in more detail in each subsystem section.

The SVT innermost layer has to provide good space resolution while coping with high background. Although silicon stripsets are a viable option at moderate background levels, a pixel system would certainly be more robust against background. However, keeping the material in a pixel system low enough not to deteriorate the vertexing performance is challenging, and there is considerable activity to develop thin hybrid pixels or, even better, monolithic active pixels. These devices may be part of a planned upgrade path and installed as a second generation Layer0. Efforts are directed towards the development of sensors, high rate readout electronics, cooling systems and mechanical support with low material content.

In the DCH, many parameters must be optimized for Super B running, such as the gas mixture and the cell layout. Precision measurements of fundamental gas parameters are ongoing, as well as studies with small cell chamber prototypes and simulation of the properties of different gas mixtures and cell layouts. An improvement of the performance of the DCH could be obtained by using the innovative “Cluster Counting” method, in which single clusters of charge are resolved time-wise and counted, improving the resolution on the track specific ionization and the space accuracy. This technique requires significant R&D to be proven feasible in the experiment.

Though the Barrel PID system takes over major components from *BABAR*, the new camera and readout concept is a significant departure from the *BABAR* system, requiring extensive R&D. The challenges include the performance

of pixelated PMTs for DIRC, the design of the fused silica optical system, the coupling of the fused silica optics to the existing bar boxes, the mechanical design of the camera, and the choice of electronics. Many of the individual components of the new camera are now under active investigations by members of the PID group, and studies are underway with a single bar prototype located in a cosmic ray telescope at SLAC. A full scale (1/12 azimuth) prototype incorporating the complete optical design is planned for cosmic ray tests during the next two years.

Endcap PID concepts are less developed, and whether they match the physics requirements and achieve the expected detector performance remains to be demonstrated. Present R&D is centered on developing a good conceptual understanding of different proposed concepts, on simulating how their performance affects the physics performance of the detector, and on conceptual R&D for components of specific devices to validate concepts and highlight the technical and cost issues.

The EMC barrel is a well understood device at the lower luminosity of *BABAR*. Though there will be some technical issues associated with refurbishing, the main R&D needed at present is to understand the effects of pile-up in simulation, so as to be able to design the appropriate front-end shaping time for the readout.

The forward and backward EMCs are both new devices, using cutting edge technology. Both will require one or more full beam tests, hopefully at the same time, within the next year or two. Prototypes for these tests are being designed and constructed.

Systematic studies of IFR system components have been performed in a variety of bench and cosmic ray tests, leading to the present proposed design. This design will be beam tested in a full scale prototype currently being prepared for a Fermilab beam. This device will demonstrate the muon identification capabilities as a function of different iron configurations, and will also be able to study detector efficiency and spatial resolution.

At present, the Electronics, DAQ, and Trigger (ETD), have been designed for the base luminosity of $1 \times 10^{36} \text{ cm}^{-2} \text{ s}^{-1}$, with adequate headroom. Further R&D is needed to understand the requirements at a luminosity up to 4 times greater, and to insure that there is a smooth upgrade path when the present design becomes inadequate. On a broad scale, as discussed in the system chapter, each of the many components of ETD have numerous technical challenges that will require substantial R&D as the design advances.

References

- [1] M. Bona *et al.*, *SuperB: A High-Luminosity Heavy Flavour Factory. Conceptual Design Report*, arXiv:0709.0451v2 [hep-ex], INFN/AE-07/2, SLAC-R-856, LAL 07-15, also available at <http://www.pi.infn.it/SuperB/CDR>.
- [2] F. A. Berends, P. H. Daverveldt and R. Kleiss, *Monte Carlo Simulation of Two Photon Processes. 2. Complete Lowest Order Calculations for Four Lepton Production Processes in Electron Positron Collisions*, *Comput. Phys. Commun.* **40**, 285 (1986).

3 Silicon Vertex Tracker

3.1 Detector Concept

3.1.1 SVT and Layer0

The Silicon Vertex Tracker, as in *BABAR*, together with the drift chamber (DCH) and the solenoidal magnet provide track and vertex reconstruction capability for the Super*B* detector. Precise vertex information, primarily extracted from precise position measurements near the IP by the SVT, is crucial to the measurement of time-dependent CP asymmetries in B^0 decays, which remains a key element of the Super*B* physics program. In addition, charged particles with transverse momenta lower than 100 MeV/ c will not reach the central tracking chamber, so for these particles the SVT must provide the complete tracking information.

These goals have been reached in the *BABAR* detector with a five-layer silicon strip detector, shown schematically in Fig. 5. The *BABAR* SVT provided excellent performance for the whole life of the experiment, thanks to a robust design that took into account the physics requirements as well as enough safety margin, to cope with the machine background, and redundancy considerations. The Super*B* SVT design is based on the *BABAR* vertex detector layout with the addition of an innermost layer closer to the IP (Layer0). The Layer0 close-in position measurements lead to an improved vertex resolution, which is expected to largely compensate for the reduced boost at the Super*B*, thus retaining the Δt resolution for B decays achieved in *BABAR*. Physics studies and background conditions, as explained in detail in the next two sections, set stringent requirements on the Layer0 design: radius of about 1.5 cm; high granularity ($50 \times 50 \mu\text{m}^2$ pitch); low material budget (about 1% X_0); and adequate radiation resistance.

For the Technical Design Report preparation, several options are under study for the Layer0 technology, with different levels of maturity, expected performance and safety margin against background conditions. These include stripl

modules based on high resistivity sensors with short strips, and hybrid pixels and other thin pixel sensors based on CMOS Monolithic Active Pixel Sensor (MAPS).

The current baseline configuration of the SVT Layer0 is based on the stripl

The external SVT layers (1-5), with a radius between 3 and 15 cm, will be built with the same technology used for the *BABAR* SVT (double sided silicon strip sensor), which is adequate for the machine background conditions expected in the Super*B* accelerator scheme (*i.e.* with low beam currents).

The SVT angular acceptance, constrained by the interaction region design, will be 300 mrad in both the forward and backward directions, corresponding to a solid angle coverage of 95% in the center-of-mass frame.

3.1.2 Performance Studies

The ultra-low emittance beams of the Super*B* design opens up the possibility of using a small radius beam pipe (1 cm) in the detector acceptance, allowing to have the innermost layer of the SVT very close to the IP. The small radius of the pipe increases the heating from image charges and hence a water cooling channel is foreseen for the beam pipe to extract this power. The total amount of radial material of the beryllium pipe, which includes a few μm of gold foil, and the water cooling channel, is estimated to be less than 0.5% X_0 . For the

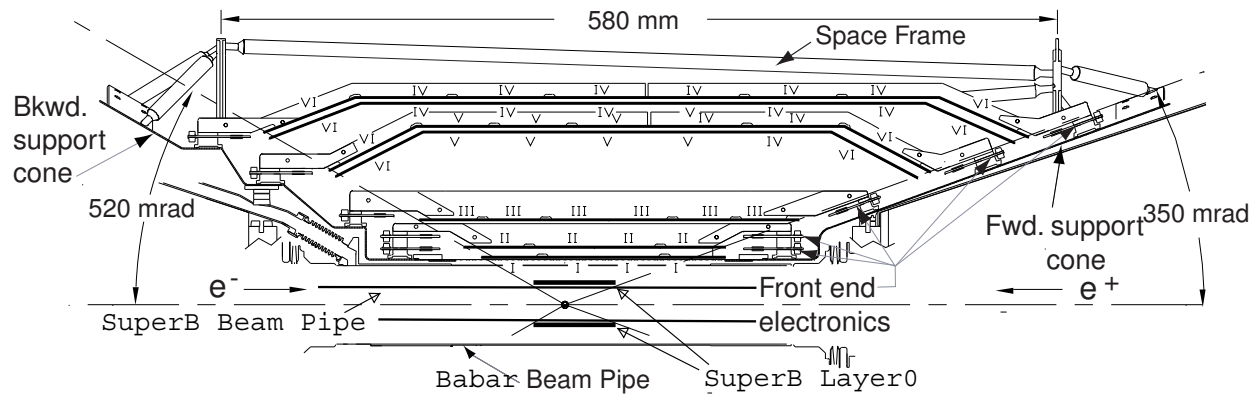


Figure 5: Longitudinal section of the SVT

proposed SuperB boost, $\beta\gamma = 0.28$ for 7 GeV e^- beam against a 4 GeV e^+ beam, the average B vertex separation along the z coordinate, $\langle\Delta z\rangle \simeq \beta\gamma c\tau_B = 125\ \mu\text{m}$, is around half of that in *BABAR*, where $\beta\gamma = 0.55$. In order to maintain a suitable resolution on Δt for time-dependent analyses, it is necessary to improve the vertex resolution (by about a factor 2) with respect to that achieved in *BABAR*: typically $50 - 80\ \mu\text{m}$ in z for exclusively reconstructed modes and $100 - 150\ \mu\text{m}$ for inclusively reconstructed modes (typical resolutions for the tagging side in CPV measurements). The six-layer SVT solution for SuperB, with the Layer0 sitting much closer to the IP than that in *BABAR*, would significantly improve track parameter determination, matching the more demanding requirements on the vertex resolution, while maintaining the stand-alone tracking capabilities for low momentum particles.

The choice among the various options under consideration for the Layer0 has to take into account the physics requirements for the vertex resolution, depending on the pitch and the total amount of material of the modules. In addition, to assure optimal performance for track reconstruction, the sensor occupancy has to be maintained under a few percent level, imposing further constraints on the sensor segmentation and on the front-end electronics. Radiation hardness is also an important factor, although

it is expected not to be particularly demanding compared to the LHC detector specifications.

The simulation program FastSim [1] has been used to study track and vertex reconstruction performance of various SVT configurations, providing estimates of the B decay vertex resolution as well as Δt resolution for time-dependent CPV measurements. We have considered several benchmark channels, including $B \rightarrow \pi^+\pi^-$, ϕK_S^0 and also decay modes where the impact of the Layer0 on the decay vertex determination is expected to be less important, such as $B \rightarrow K_S^0 K_S^0$, $K_S^0 \pi^0$. For each mode we have studied the resolution on Δt and the percent error on the quantity of physics interest, namely $\sin(2\beta_{eff})$.

The main conclusion is that the baseline SuperB SVT design – the six-layer design – leads to an improved Δt resolution over that achieved in *BABAR*, allowing for a comparable (or even better) per-event error on $\sin(2\beta_{eff})$, for the B decay modes considered in this study. This conclusion is valid for all candidate technologies that have been considered for Layer0, and for reasonable values of the Layer0 radius and amount of radial material. As an example, in Fig. 6 is reported the resolution on Δt for different Layer0 radii as a function of the Layer0 thickness (in X_0 %) compared to the *BABAR* reference value. The dashed line represents the *BABAR* reference value using the nominal value of the boost in PEP-II, $\beta\gamma = 0.55$.

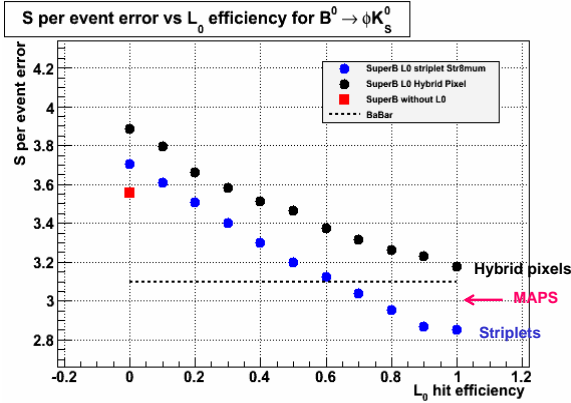


Figure 7: $\sin 2\beta_{eff}$ per event error as a function of the Layer0 efficiency for the different options (i.e. different material budget).

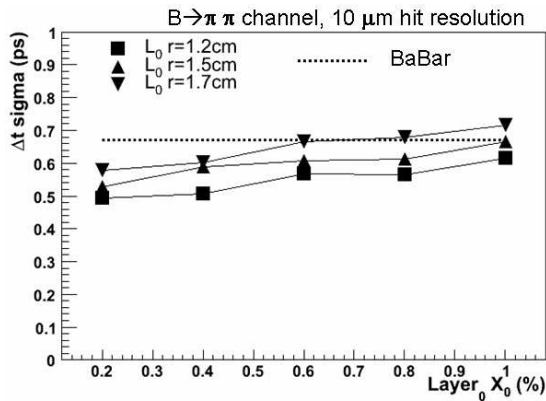


Figure 6: Resolution on the proper time difference of the two B mesons ($\beta\gamma = 0.28$), for different Layer0 radii, as a function of Layer0 thickness (in X_0 %).

We have also studied the impact of a possible Layer0 inefficiency on $\sin(2\beta)$ sensitivity. The source of inefficiency could be related to several causes, for example a much higher background rate than expected, causing dead time in the readout of the detector. In Fig. 7 is reported the $\sin(2\beta_{eff})$ per-event error for the $B \rightarrow \phi K_S^0$ decay mode as a function of the Layer0 hit ef-

iciency for different Layer0 technology options. The Layer0 radius in the study is about 1.6 cm. The results show that the triplet solution provides better performance, both with respect to *BABAR*, even for the case of some (small) hit inefficiency, and other Layer0 solutions. The main advantage of the triplet solution is the smaller material budget (about 0.5% X_0) compared to the Hybrid pixel (about 1% X_0) and the MAPS solutions (about 0.7% X_0). For particles of momenta up to a few GeV/c, the multiple scattering effect is the dominant source of uncertainty in the determination of their trajectory, thus a low material budget detector provides a clear advantage. A triplet-based Layer0 solution would also have a better intrinsic hit resolution about $8 \mu\text{m}$) with respect to the MAPS and the Hybrid Pixel (about $14 \mu\text{m}$ with a digital readout) solutions. For those reasons a Layer0 based on triplets has been chosen as the baseline solution for SuperB, able to cope with the machine background according to the present estimates.

3.1.3 Background Conditions

Background considerations influence several aspects of the SVT design: readout segmentation; electronics shaping time; data transmission rate; and radiation hardness (particularly severe for Layer0). The different sources of background have been simulated with a detailed Geant4-based detector model and beamline description to estimate their impact on the experiment [2]. The background hits expected in the external layers of the SVT (radius > 3 cm) are mainly due to processes that scale with beam currents, similar to background seen in the present *BABAR* SVT. The background at the Layer0 radius is primarily due to luminosity terms, in particular the $e^+e^- \rightarrow e^+e^-e^+e^-$ pair production, with radiative Bhabha events an order of magnitude smaller. Despite the huge cross section of the pair production process, the rate of tracks originating from this process hitting the Layer0 sensors is strongly suppressed by the 1.5 Tesla magnetic field of the SuperB detector. Particles produced with low transverse

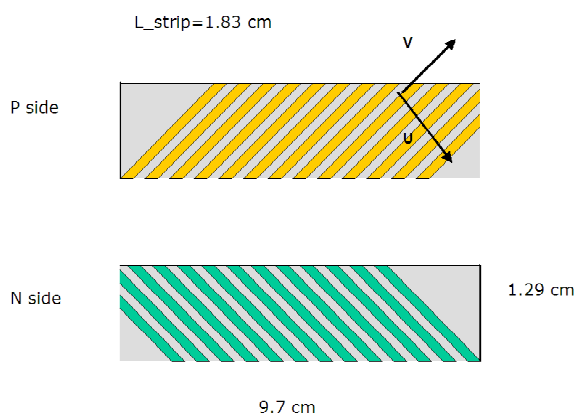


Figure 8: Schematic view of the two sides of the triplets detector.

momenta loop in the detector magnetic field, and only a small fraction reaches the SVT layers, with a strong radial dependence.

According to these studies the track rate at the Layer0 at a radius of 1.5 cm is at the level of about 5 MHz/cm^2 , mainly due to electrons in the MeV energy range. The equivalent fluence corresponds to about $3.5 \times 10^{12} \text{ n/cm}^2/\text{yr}$, corresponding to a dose rate of about 3 Mrad/yr . A safety factor of five on top of these numbers has been considered in the design of the SVT.

3.2 Layer0 Options Under Study

In this section we summarize the current status of the studies of the various Layer0 options, aimed at the eventual preparation of the SuperB Technical Design Report.

3.2.1 Striplots

Double-sided silicon strip detectors (DSSD), $200 \mu\text{m}$ thick, with $50 \mu\text{m}$ readout pitch represent a proven and robust technology, meeting the requirements on the SVT Layer0 design, as described in the CDR [2]. In this design, short strips will be placed at an angle of $\pm 45^\circ$ to the detector edge on the two sides of the sensor, as shown in Fig 8.

The strips will be connected to the readout electronics through a multilayer flexible circuit glued to the sensor. A standard technology

with copper traces is already available, although an aluminum microcable technology is being explored to reduce the impact on material of the interconnections.

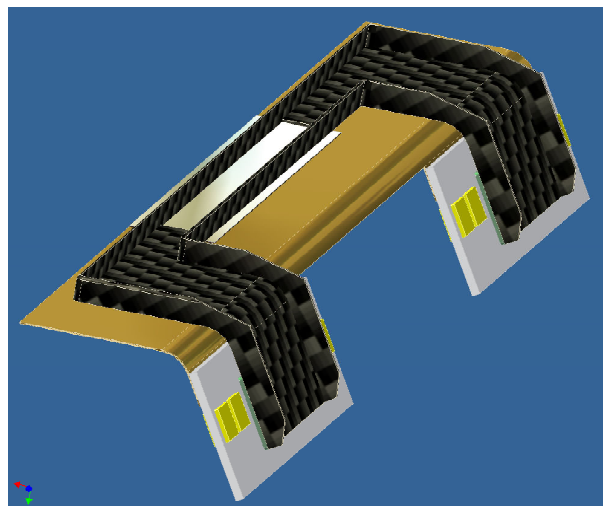


Figure 9: Mechanical structure of a triplets Layer0 module.

The data-driven, high-bandwidth FSSR2 readout chip [3], is a good match to the Layer0 strip design and is also suitable for the readout of the strip sensors in the outer layers. It has 128 analog channels providing a sparsified digital output with address, timestamp and pulse height information for all hits. The selectable shaper peaking time can be programmed down to 65 ns. The chip has been realized in a $0.25 \mu\text{m}$ CMOS technology for high radiation tolerance. The readout architecture has been designed to operate with a 132 ns clock that will define the timestamp granularity and the readout window. A faster readout clock (70 MHz) is used in the chip, with a token pass logic, to scan for the presence of hits in the digital section, and to transmit them off-chip, using a selectable number of output data lines. With six output lines, the chip can achieve an output data rate of 840 Mbits/s. With a 1.83 cm strip length the expected occupancy in the 132 ns time window is about 12%, considering a hit rate of 100 MHz/cm^2 , including the cluster multiplicity and a factor 5 safety margin on the simulated

background track rate. The FSSR2 readout efficiency has never been measured with this occupancy. First results from ongoing Verilog simulations indicate the efficiency is 90% or more. As shown in Fig. 7 the physics impact of such an inefficiency is modest. Nonetheless it may be possible to redesign the digital readout of the FSSR2 to increase the readout efficiency at high occupancy. A total equivalent noise charge of $600 e^-$ rms is expected, including the effects of the strip and flex circuit capacitance, as well as the metal series resistance. The signal to noise for a $200 \mu\text{m}$ detector is about 26, providing a good noise margin. It is also foreseen to conduct a market survey to evaluate whether different readout chips, possibly with a triggered readout architecture, may provide better performance.

Because of the unfavorable aspect ratio of the sensors, the readout electronics needs to be rotated and placed along the beam axis, outside of the sensitive volume of the detector, held by a carbon fiber mechanical structure, as shown in Fig. 9. The 8 modules forming Layer0 will be mounted on flanges containing the cooling circuits. For the baseline design with stripsets, the Layer0 material budget will be about $0.46\%X_0$ for perpendicular tracks, assuming a silicon sensor thickness of $200 \mu\text{m}$, a light module support structure ($\sim 100 \mu\text{m}$ Silicon equivalent), similar to that used for the *BABAR* SVT modules, and the multilayer flex contribution (3 flex layers/module, $\sim 45 \mu\text{m}$ Silicon equivalent/layer). A reduction in the material budget to about $0.35\%X_0$ is possible if kapton/aluminum microcable technology can be employed with a trace pitch of about $50 \mu\text{m}$.

3.2.2 Hybrid Pixels

Hybrid pixels technology represents a mature and viable solution but still requires some R&D to meet Layer0 requirements (reduction in the front-end pitch and in the total material budget, with respect to hybrid pixel systems developed for LHC experiments) A front-end chip for hybrid pixel sensors with $50 \times 50 \mu\text{m}^2$ pitch and a fast readout is under development. The adopted readout architecture has been previously devel-

oped by the SLIM5 Collaboration [4] for CMOS Deep NWell MAPS [5, 6], the data-push architecture features data sparsification on pixel and timestamp information for the hits. This readout has been recently optimized for the target Layer0 rate of $100 \text{ MHz}/\text{cm}^2$ with promising results: VHDL simulation of a full size matrix (1.3 cm^2) gives hit efficiency above 98% operating the matrix with a 60 MHz readout clock. A first prototype chip with 4k pixels has been submitted in September 2009 with the ST Microelectronics 130 nm process and is currently under test. The front-end chip, connected by bump-bonding to an high resistivity pixel sensor matrix, will be then characterized with beams in Autumn 2010.

3.2.3 MAPS

CMOS MAPS are a newer and more challenging technology. Their main advantage with respect to hybrid pixels is that they could be very thin, having the sensor and the readout incorporated in a single CMOS layer, only a few tens of microns thick. As the readout speed is another relevant aspect for application in the SuperB Layer0, we proposed a new design approach to CMOS MAPS [5] which for the first time made it possible to build a thin pixel matrix featuring a sparsified readout with timestamp information for the hits [6]. In this new design the deep N-well (DNW) of a triple well commercial CMOS process is used as charge collecting electrode and is extended to cover a large fraction of the elementary cell (Fig. 3.2.3). Use of a large area collecting electrode allows the designer to include also PMOS transistors in the front-end, therefore taking full advantage of the properties of a complementary MOS technology for the design of high performance analog and digital blocks. However, in order to avoid a significant degradation in charge collection efficiency, the area covered by PMOS devices and their N-wells, acting as parasitic collection centers, has to be small with respect to the DNW sensor area. Note, that the use of a charge preamplifier as the input stage of the channel makes the charge sensitivity independent of the

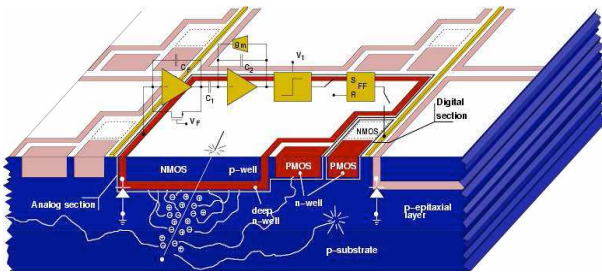


Figure 10: The DNW MAPS concept.

detector capacitance. The full signal processing chain implemented at the pixel level (charge preamplifier, shaper, discriminator and latch) is partly realized in the p-well physically overlapped with the area of the sensitive element, allowing the development of a complex in-pixel logic with similar functionalities to hybrid pixels.

Several prototype chips (the “APSEL” series) have been realized with the STMicroelectronics, 130 nm triple well technology and demonstrated that the proposed approach is very promising for the realization of a thin pixel detector. The APSEL4D chip, a 4k pixel matrix with $50 \times 50 \mu\text{m}^2$ pitch, with a new DNW cell and the sparsified readout has been characterized during the SLIM5 testbeam showing encouraging results [7]. Hit efficiency of 92% has been measured, a value compatible with the present sensor layout that is designed with a fill factor (*i.e.* the ratio of the electrode to the total n-well area) of about 90%. Margins to improve the detection efficiency with a different sensor layout are being currently investigated [8]

Several issues still need to be solved to demonstrate the ability to build a working detector with this technology, which required further R&D. Among others, the scalability to larger matrix size and the radiation hardness of the technology are under evaluation for the TDR preparation.

3.2.4 Pixel Module Integration

To minimize the detrimental effect of multiple scattering on track parameter resolution, the re-

duction of the material is crucial for all the components of the pixel module in the active area.

The pixel module support structure needs to include a cooling system to extract the power dissipated by the front-end electronics, about $2\text{W}/\text{cm}^2$, present in the active area. The proposed module support will be realized with a light carbon fiber support with integrated microchannels for the coolant fluid (total material budget for support and cooling below $0.3\%X_0$). Measurements on first support prototypes realized with this cooling technique indicate that a cooling system based on microchannels can be a viable solution to the thermal and structural problem of Layer0 [10].

The pixel module will also need a light multilayer bus (Al/kapton based with total material budget of about $0.2\%X_0$), with power/signal inputs and high trace density for high data speed to connect the front-end chips in the active area to the HDI hybrid, in the periphery of the module. With the data push architecture presently under study and the high background rate, the expected data with a 160 MHz clock need to be transferred on this bus. With triggered readout architecture (also under investigation) the complexity of the pixel bus, and material associated, will be reduced.

Considering the various pixel module components (sensor and front-end with $0.4\%X_0$, support with cooling, and multilayer bus with decoupling capacitors) the total material in the active area for the Layer0 module design based on hybrid pixel is about $1\%X_0$. For a pixel module design based on CMOS MAPS, where the contribution of the sensor and the integrated readout electronics become almost negligible, $0.05\%X_0$, the total material budget is about $0.65\%X_0$. A schematic drawing of the full Layer0 made of 8 pixel modules mounted around the beam pipe with a pinwheel arrangement is shown in Fig. 3.2.4.

Due to the high background rate at the Layer0 location, radiation-hard fast links between the pixel module and the DAQ system located outside the detector should be adopted.

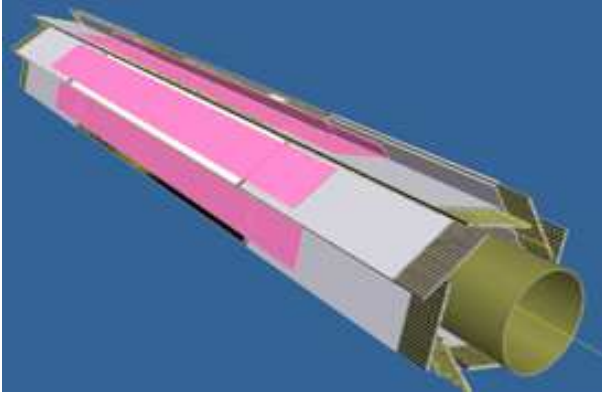


Figure 11: Schematic drawing of the full Layer0 made of 8 pixel modules mounted around the beam pipe with a pin-wheel arrangement.

For all Layer0 options (that currently share a similar data push architecture) the untriggered data rate is 16 Gbits/s per readout section, assuming a background hit rate of 100 MHz/cm^2 . Triggered data rate is reduced to about 1 Gbit/s per readout section.

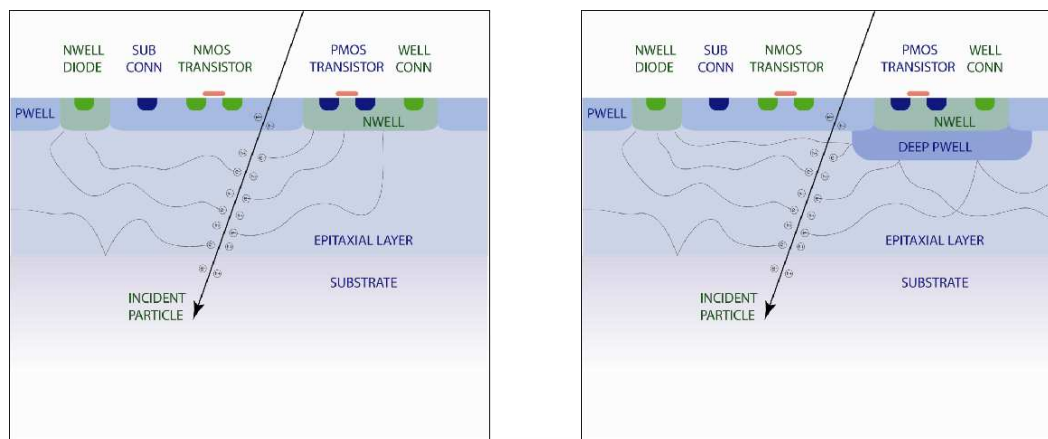
The HDI, positioned at the end of the module, outside the active area, will be designed to host several IC components: some glue logic, buffers, fast serializers, drivers. The components should be radiation hard for the application at the Layer0 location (several Mrad/yr).

The baseline option for the link between the Layer0 modules and the DAQ boards is currently based on a mixed solution. A fast copper link is foreseen between the HDI and an intermediate transition board, positioned in an area of moderate radiation levels (several tens of krad/yr). On this transition card the logic with LV1 buffers will store the data until the reception of the LV1 trigger signal and only triggered data will be sent to the DAQ boards with an optical link of 1 Gbit/s. The various pixel module interfaces will be characterized in a test set-up for the TDR preparation.

3.3 A MAPS-based All-pixel SVT Using a Deep P-well Process

Another alternative under evaluation is to have an all-pixel SVT using MAPS pixels with a pixel

size of $50 \times 50 \mu\text{m}^2$. This approach uses the 180 nm INMAPS process which incorporates a deep P-well. A perceived limitation of standard MAPS is not having full CMOS capability as the additional N-wells from the PMOS transistors parasitically collect charge, thus reducing the charge collected by the readout diode. Avoiding the usage of PMOS transistors however does limit the capability of the readout circuitry significantly. A limited use of PMOS is allowed with the DNW MAPS design (APSEL chips), which anyway accounts for a small degradation in the collection efficiency. Therefore, a special deep P-well layer was developed to overcome the problems mentioned above. The deep P-well protects charge generated in the epitaxial layer from being collected by parasitic N-wells for the PMOS. This then ensures that all charge is being collected by the readout diode and maximizes charge collection efficiency. This is illustrated in Fig. 12. This enhancement allows the use of full CMOS circuitry in a MAPS and opens completely new possibilities for in-pixel processing. The TPAC chip [11] for CALICE-UK [12, 13] has been designed using the INMAPS process. The basic TPAC pixel has a size of $50 \times 50 \mu\text{m}^2$ and comprises a preamplifier, a shaper and a comparator [11]. The pixel only stores hit information in a Hit Flag. The pixel is running without a clock and the timing information is provided by the logic querying the Hit Flag. For the SuperB application the pixel design was slightly modified. Instead of just a comparator, a peak-hold latch was added to store the analog information as well. The chip is organized in columns with a common ADC at the end of each column. The ADC is realized as a Wilkinson ADC using a 5 MHz clock rate. The simulated power consumption for each individual pixel is $12 \mu\text{W}$. The column logic constantly queries the pixels, but only digitizes the information for the pixels with a “Hit Flag”. This allows one to save both space and reduce the power usage and since the speed of the chip is limited by the ADC also increases the



(a) CMOS MAPS without a deep P-well implant

(b) CMOS MAPS with a deep P-well implant

Figure 12: A CMOS MAPS without a deep P-well implant (left) and with a deep P-well implant (right).

readout speed. Both the address of the pixel being hit and its ADC output are stored in a FIFO at the end of the column. To further increase the readout speed, the ADC uses a pipelined architecture with 4 analog input lines to increase throughput of the ADC. One of the main bottlenecks is getting the data off the chip. It is envisaged to use the Level 1 trigger information to reject most of the events and to reduce the data rate on-chip before moving it off-chip. This will significantly reduce the data rate and therefore also the amount of power and services required.

For the outer layers, the requirements are much more relaxed in terms of occupancy so, in order to reduce the power, it is planned to multiplex the ADCs to let them handle more than one column in the sensor. This is possible because of the much smaller hit rate in the outer layers and the resulting relaxed timing requirements.

An advantage of the MAPS is the elimination of a lot of readout electronics, because everything is already integrated in the sensor, which simplifies the assembly significantly. Also since we are using an industry CMOS process, there is a significant price advantage compared to standard HEP-style silicon and additional savings

due to the elimination of a dedicated readout ASIC.

In order to evaluate the physics potential of MAPS based all-pixel vertex detector, we are currently evaluating the performance of the SuperB detector with different geometries of the SVT, ranging from the SuperB baseline (Layer0 + 5 layers based on strip detectors), through to a 4 or 6 layer all-pixel detector with a realistic material budget for the support structure for all layers.

3.4 R&D Activities

The technology for the Layer0 baseline triplet design is well-established. However, the front-end chip to be used, due to the expected high background occupancy, requires some deeper investigation. Performance of the FSSR2 chip, proposed for the readout of the triplets and the outer layer strip sensors, are being evaluated as a function of the occupancy with Verilog simulation. Measurements are also possible in a testbench in preparation with real triplets modules readout with the FSSR2 chips. The design of the digital readout of the chip will be investigated to improve its efficiency. The modification of the analog part of the chip for the readout of the long module of the external lay-

ers are currently under study. The multilayer flexible circuit, to connect the stripsets sensor to the front-end electronics, may benefit from some R&D to reduce the material budget: either to reduce the minimum pitch on the Upilex circuit, or adopt kapton/aluminum microcables and Tape Automated Bonding soldering techniques with a $50\ \mu\text{m}$ pitch.

Although silicon stripsets are a viable option at moderate background levels, a pixel system would certainly be more robust against background. Keeping the material in a pixel system low enough not to deteriorate the vertexing performance is challenging, and there is considerable activity to develop thin hybrid pixels or, even better, monolithic active pixels. These devices may be part of a planned upgrade path and installed as a second generation Layer0.

A key issue for the readout of the pixels in Layer0 is the development of a fast readout architecture to cope with a hit rate of the order of $100\ \text{MHz}/\text{cm}^2$. A first front-end chip for hybrid pixel sensor with $50 \times 50\ \mu\text{m}^2$ pitch and a fast readout, data driven with timestamp for the hits, has been realized and is currently under test. A further development of the architecture is being pursued to evolve toward a triggered readout architecture, helpful to reduce the complexity of the pixel module and possibly to reduce its material budget.

The CMOS MAPS technology is very promising for an alternative design of Layer0, but extensive R&D is still needed to meet all the requirements. Key aspects to be addressed are: sensor efficiency and its radiation tolerance; power consumption; and, as in the hybrid pixel, the readout speed of the architecture implemented.

After the realization of the APSEL chips with the ST 130 nm DNW process, with very encouraging results, the Italian collaborators involved in the CMOS MAPS R&D are now evaluating the possibility to improve MAPS performance with the use of modern vertical integration technologies [9]. A first step in this direction has been the realization of a two-tier DNW MAPS by face to face bonding of two $130\ \mu\text{m}$ CMOS wafer in the Chartered/Tezzaron process. Hav-

ing the sensor and the analog part of the pixel cell in one tier and the digital part in the second tier can significantly improve the efficiency of the CMOS sensor and allow a more complex in-pixel logic. The first submission of vertically integrated DNW MAPS, now in fabrication, includes a 3D version of a 8×32 MAPS matrix with the same sparsified readout implemented in the APSEL chips. A new submission is foreseen in Autumn 2010 with a new generation of the 3D MAPS implementing a faster readout architecture under development, which is still data push but could be quite easily evolve toward a triggered architecture.

The development of a thin mechanical support structure with integrated cooling for the pixel module is continuing with promising results. Prototypes with light carbon fiber microchannels for the coolant fluid (total material down to $0.15\% X_0$) have been produced and tested and are able to evacuate specific power up to $1.5\text{W}/\text{cm}^2$ maintaining the pixel module temperature within the requirements. These supports could be used for either hybrid pixel or MAPS sensors.

References

- [1] *FastSim* program, available online at: <http://www.pi.infn.it/SuperB>.
- [2] M. Bona *et al.*, *SuperB: A High-Luminosity Heavy Flavour Factory. Conceptual Design Report*, arXiv:0709.0451v2 [hep-ex], INFN/AE-07/2, SLAC-R-856, LAL 07-15, also available at <http://www.pi.infn.it/SuperB/CDR>.
- [3] V. Re *et al.*, IEEE Trans. Nucl. Sci. **53**, 2470 (2006).
- [4] SLIM5 Collaboration, *Silicon detectors with Low Interaction with Material*, <http://www.pi.infn.it/slim5/>.
- [5] G. Rizzo for the SLIM5 Collaboration, *Development of Deep N-Well MAPS in a 130nm CMOS Technology and Beam Test Results on a 4k-Pixel Matrix with Digital Sparsified Readout*, 2008 IEEE Nuclear Science Symposium, Dresden, Germany, 19-25 October, 2008.

- [6] A. Gabrielli for the SLIM5 Collaboration, *Development of a triple well CMOS MAPS device with in-pixel signal processing and sparsified readout capability*, Nucl. Instrum. Methods Phys. Res., Sect. A **581**, 303 (2007).
- [7] M. Villa for the SLIM5 Collaboration, *Beam-Test Results of 4k pixel CMOS MAPS and High Resistivity Striplet Detectors equipped with digital sparsified readout in the Slim5 Low Mass Silicon Demonstrator*, Nucl. Instrum. Methods Phys. Res., Sect. A (2010) doi:10.1016/j.nima.2009.10.035
- [8] E. Paoloni for the VIPIX collaboration, *Beam Test Results of Different Configurations of Deep N-well MAPS Matrices Featuring in Pixel Full Signal Processing*, Proceedings of the XII Conference on Instrumentation, Vienna 2010. To be published in Nucl. Instrum. Methods Phys. Res., Sect. A.
- [9] R. Yarema, *3D circuit integration for vertex and other detectors*, Proceedings 16th International Workshop on Vertex Detectors (VERTX2007), Lake Placid (NY, USA), September 23 - 28, 2007, Proceedings of Science PoS(Vertex 2007)017.
- [10] F. Bosi and M. Massa, *Development and Experimental Characterization of Prototypes for Low Material Budget Support Structure and Cooling of Silicon Pixel Detectors, Based on Microchannel Technology*, Nucl. Instrum. Methods Phys. Res., Sect. A (2010) doi:10.1016/j.nima.2009.10.138
- [11] J. A. Ballin *et al.*, *Monolithic Active Pixel Sensors (MAPS) in a quadruple well technology for nearly 100% fill factor and full CMOS pixels*, Sensors **8**, 5336 (2008).
- [12] N. K. Watson *et al.*, *A MAPS-based readout of an electromagnetic calorimeter for the ILC*, J. Phys. Conf. Ser. **110**, 092035 (2008).
- [13] J. P. Crooks *et al.*, *A monolithic active pixel sensor for a tera-pixel ECAL at the ILC*, CERN-2008-008.

4 Drift Chamber

The Super B Drift Chamber (DCH) provides measurements of the charged particle momentum and of the ionization energy loss used for particle identification. This is the primary device in Super B to measure velocities of particles having momenta below approximately 700 MeV/ c . It is based on the $BABAR$ design, with 40 layers of centimetre-sized cells strung approximately parallel to the beamline [1]. A subset of layers are strung at a small stereo angle in order to provide measurements along z , the beam axis.

The DCH is required to provide momentum measurements with the same precision as the $BABAR$ DCH (approximately 0.4% for tracks with a transverse momentum of 1 GeV/ c), and like $BABAR$ uses a helium-based gas mixture in order to minimize measurement degradation from multiple scattering. The challenge is to achieve comparable or better performance than $BABAR$ in a high luminosity environment. Both physics and background rates will be significantly higher than in $BABAR$ and as a consequence the system is required to accommodate the 100-fold increase in trigger rate and luminosity-related backgrounds primarily composed of radiative Bhabhas and electron-pair backgrounds from two-photon processes. However, the beam current related backgrounds will only be modestly higher than in $BABAR$. The nature and spatial distributions of these backgrounds dictate the overall geometry of the DCH.

The ionization loss measurement is required to be at least as sensitive to particle discrimination as $BABAR$ which has a dE/dx resolution of 7.5% [1]. In $BABAR$, conventional dE/dx drift chamber methods were used in which the total charge deposited on each sense wire was averaged after removing the highest 20% of the measurements as a means of controlling Landau fluctuations. In addition to this conventional approach, the Super B DCH group is exploring

a *cluster counting* option [4] which, in principle, can improve the dE/dx resolution by approximately a factor of two. This technique involves counting individual clusters of electrons released in the gas ionization process. In so doing, we remove the sensitivity of the specific energy loss measurement to fluctuations in the amplification gain and in the number of electrons produced in each cluster, fluctuations which significantly limit the intrinsic resolution of conventional dE/dx measurements. As no experiment has employed *cluster counting*, this is very much a detector research and development project but one which potentially yields significant physics payoff at Super B .

4.1 Backgrounds

The dominant source of background in the Super B DCH is expected to be radiative Bhabha scattering. Photons radiated collinearly to the initial e^- or e^+ direction can bring the beams off-orbit and ultimately produce showers on the machine optic elements. This process can happen meters away from the interaction point and the hits are in general uniformly distributed over the whole DCH volume. Large-angle $e^+e^- \rightarrow e^+e^-(\gamma)$ scattering, on the other hand, has the well-known $1/\vartheta^4$ cross section dependence; simulation studies are currently underway to evaluate the need to design tapered endcaps (either conical or a with stepped shape) at small radii to keep under control the occupancy in the very forward region of the detector. The actual occupancy and its geometrical distribution in the detector depend on the details of the machine elements, on the amount and placement of shields, on the DCH geometry, and on the time needed to collect the signal in the detector. Preliminary results obtained with Geant4 simulations indicate that in a $1 \mu\text{s}$ time window at nominal luminosity ($10^{36} \text{ cm}^{-2} \text{ s}^{-1}$) the occupancy averaged over the whole DCH volume is 3.5%, and slightly larger (about 5%) in the inner layers. Intense work is presently underway to validate these results and study their dependence on relevant parameters.

4.2 Drift Chamber Geometry

The SuperB DCH will have a cylindrical geometry. The inner radius and length of the chamber are being re-optimized through detailed simulation studies with respect to *BABAR* since:

- a) in SuperB there will be no support tube connecting the machine elements between the SVT and the DCH;
- b) the possibility is being considered to add a PID device between the DCH and the forward calorimeter, and a calorimeter in the backward direction.

Simulation studies performed on several signal samples with both high (e.g. $B \rightarrow \pi^+\pi^-$), and medium-low (e.g. $B \rightarrow D^*K$) momentum tracks indicate that:

- a) due to the increased lever arm, momentum resolution improves as the minimum DCH radius R_{min} decreases, see Fig. 13; R_{min} is actually limited by mechanical integration constraints with the cryostats and the radiation shields.
- b) The momentum and especially the dE/dx resolution for tracks going in the forward or backward directions are clearly affected by the change in number of measuring samples when the chamber length is varied by 10 – 30 cm. However the fraction of such tracks is so small that the overall effect is negligible.

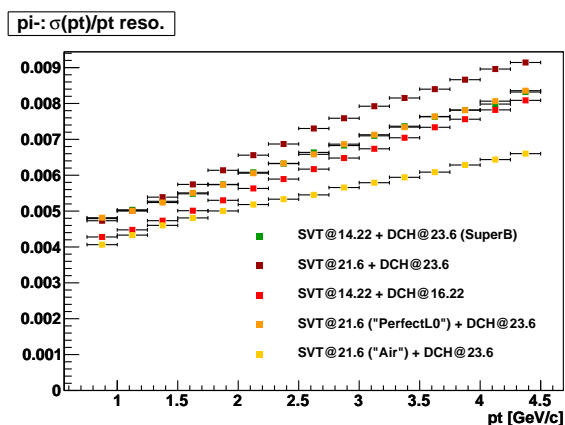


Figure 13: Track momentum resolution for different values of the drift chamber inner radius.

The DCH outer radius is constrained to 809 mm by the DIRC quartz bars. As discussed before, the DCH inner radius will be as small as possible: since a final design of the final focus cooling system is not available yet, in Fig. 14 the the nominal *BABAR* DCH inner radius of 236 mm has been used. Similarly, a nominal chamber length of 2764 mm at the outer endplate radius is used in Fig. 14: as mentioned above, this dimension has not been fixed yet, since it depends on the presence and the details of forward PID and backward EMC systems, still being discussed. Finally, as the rest of the detector, the drift chamber is shifted by the nominal *BABAR* offset (367 mm) with respect to the interaction point.

4.3 Mechanical Structure

The drift chamber mechanical structure must sustain the wire load – about 3 tons for 10 000 cells – with small deformations, while at the same time minimizing the material for the surrounding detectors. Carbon Fiber-resin composites have high elastic modulus and low density, thus offering performances superior to Aluminum-alloys based structures. Endplates with curved geometry can further reduce material thickness with respect to flat endplates for a given deformation under load. For example, the KLOE drift chamber [2] features 8 mm thick Carbon Fiber spherical endplates of 4 m diameter. Preliminary design of Carbon Fiber endplates for SuperB indicate that adequate stiffness (≤ 1 mm maximum deformation) can be obtained with 5 mm thick spherical endplates, corresponding to $0.02X_0$, to be compared with $0.13X_0$ for the *BABAR* DCH aluminum endplates.

Figure 14 shows two possible endcap layouts, respectively with spherical (a) or stepped (b) endplates. A convex spherical endplate is also considered, which would provide a better match to the geometry of the forward PID and calorimeter systems, and would reduce the impact of the endplate material on the performance of these detectors, at the cost of

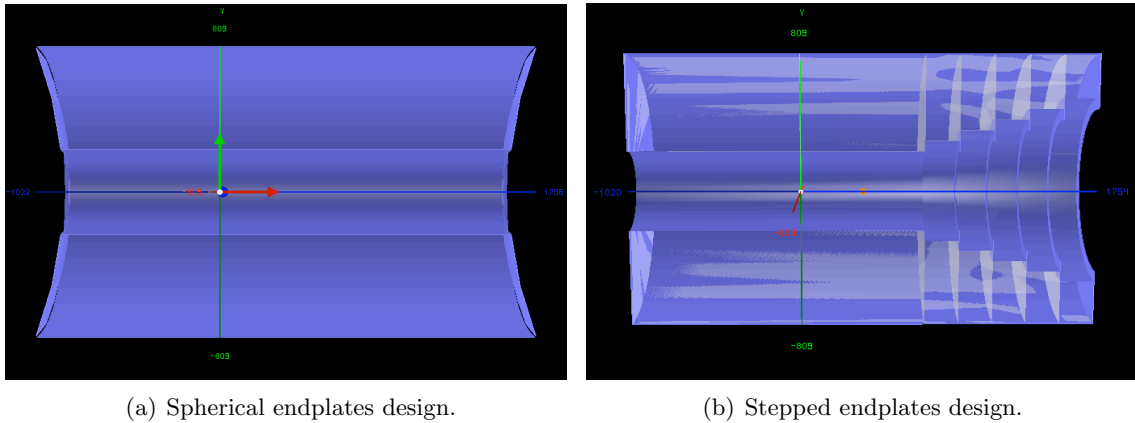


Figure 14: Two possible SuperB DCH layouts.

greater sensitivity to the large-angle Bhabha background.

4.4 Gas Mixture

The gas mixture for SuperB should satisfy the requirements which already concurred to the definition of the BABAR DCH gas mixture (80%He-20% i C₄H₁₀), *i.e.* low density, small diffusion coefficient and Lorentz angle, low sensitivity to photons with $E \sim 10$ keV. To match the more stringent requirements on occupancy rates of SuperB, it could be useful to select a gas mixture with a larger drift velocity in order to reduce ion collection times and so the probability of hits overlapping from unrelated events. The *cluster counting* option would instead call for a gas with low drift velocity and primary ionization. As detailed in Section 4.6, R&D work is ongoing to optimize the gas mixture for the SuperB environment.

4.5 Cell Design and Layout

The baseline design for the drift chamber employs small rectangular cells arranged in concentric layers about the axis of the chamber which is approximately aligned with the beam direction. The precise cell dimensions and number of layers are still to be determined, but it is expected that their side is between 10 and 20 mm and that there are approximately 40 layers as in

BABAR. The cells are grouped radially into superlayers with the inner and outer superlayers parallel to the chamber axis (axial). In BABAR the chamber also had stereo layers in which the superlayers are oriented at a small “stereo” angle relative to the axis in order to provide the z-coordinates of the track hits. The details of the stereo layer layout in SuperB is still to be determined on the basis of the cell occupancy associated with machine backgrounds.

Each cell has one 20 μ m diameter gold coated sense wire surrounded by a rectangular grid of eight field wires. The sense wires will be tensioned with a value consistent with electrostatic stability and with the yield strength of the wire. The baseline calls for a gas gain of approximately 5×10^4 which requires a voltage of approximately +2 kV to be applied to the sense wires with the field wires held at ground.

The field wires are aluminum with a diameter which will be chosen to keep the electric field on the wire surface below 20 kV/cm as a means of suppressing the Malter effect [3]. These wires will be tensioned in order to provide a gravitational sag that matches that of the sense wires.

At a radius inside the innermost superlayer the chamber has an additional layer of axially strung guard wires which serve to electrostatically contain very low momentum electrons produced from background particles showering in the DCH inner cylinder and SVT. A similarly

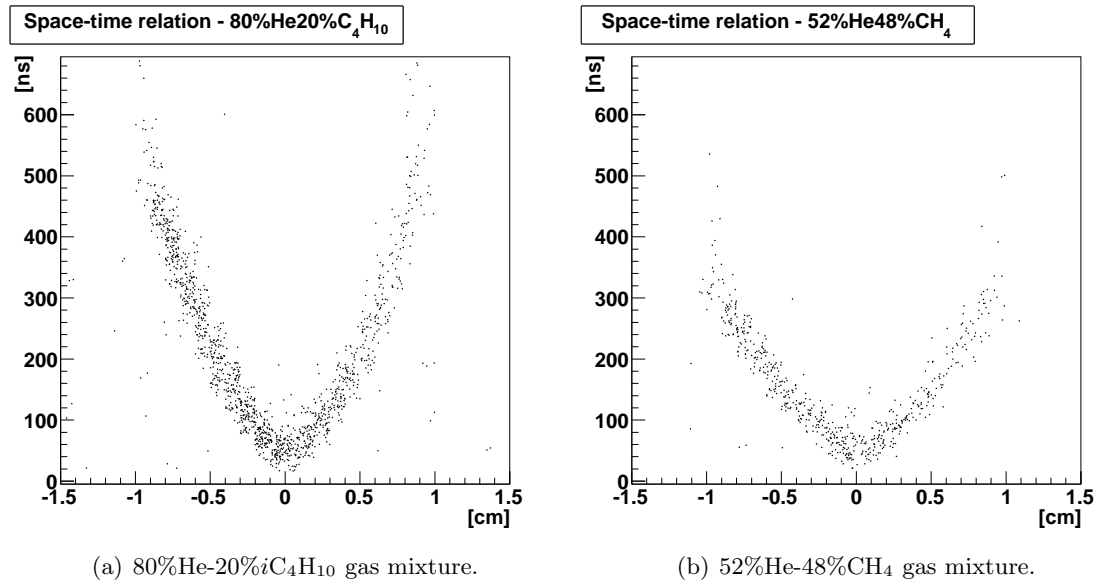


Figure 15: Examples of measured space-time relation in different He-based gas mixtures.

motivated layer will be considered at the outermost radius to contain machine background related backslash from detector material just beyond the outer superlayer.

4.6 R&D Work

Various R&D programs are underway towards the definition of an optimal DCH for SuperB, in particular: make precision measurements of fundamental parameters (drift velocity, diffusion coefficient, Lorentz angle) of potentially useful gas mixtures; study the properties of different gas mixtures and cell layouts with small DCH prototypes and simulations; and verify the potential and feasibility of the *cluster counting* option.

A precision tracker made of 3 cm diameter Aluminum tubes operating in limited streamer mode with a single tube spatial resolution of around 100 μ m has been set up. A small prototype with a cell structure resembling the one used in the BABAR DCH has also been built and commissioned. The tracker and prototype chamber have been collecting cosmic ray data since October 2009. Tracks can be extrapolated in the DCH prototype with a precision of 80 μ m

or better. Different gas mixtures have been tried in the prototype: starting with the original BABAR mixture (80%He-20% i C₄H₁₀) used as a calibration point, both different quencher proportions and different quenchers (e.g methane instead of isobutane) have been tested in order to assess the viability of lighter and possibly faster operating gas. Fig. 15a shows the space-time correlation for one prototype cell: as mentioned before, the cell structure is such as to mimic the overall structure of the BABAR DCH. Spatial resolution is consistent with what has been obtained with the original BABAR DCH. A space to time relation is depicted in Fig. 15b with a 52%He-48%CH₄ gas mixture. This gas is roughly a factor two faster and 50% lighter than the original BABAR mix: preliminary analysis shows space resolution performances comparable to the original mix; however detailed studies of the Lorentz angle have to be carried out in order to consider this mixture as a viable alternative.

To improve performances of the gas tracker a possible road could be the use of the *Cluster Counting* method. If the individual ionization cluster can be detected with high efficiency, it could in principle be possible to measure the

track specific ionization by counting the clusters themselves, providing a two-fold improvement in the resolution compared to the traditional truncated mean method. Having many independent time measurements in a single cell, the spatial accuracy could also in principle be improved substantially. Since the efficient detection of single ionization clusters requires fast risetimes (preamplifier bandwidths of the order of 1GHz) and also sampling the signal with rates of ~ 2 Gsa/s, these promises of exceptional energy and spatial resolution must however fit with the available data transfer bandwidth. A dedicate R&D effort is required to identify a gas mixture with well-separated clusters and high detection efficiency. The preamplifier noise is also an issue.

Comparisons of the traditional methods to extract spatial position and energy losses and the *cluster counting* method are being setup at the moment of writing the present report.

References

- [1] B. Aubert *et al.* (BABAR Collaboration), *The BABAR Detector*, Nucl. Instrum. Methods Phys. Res., Sect. A **479**, 1 (2002) [arXiv:hep-ex/0105044].
- [2] M. Adinolfi *et al.* (KLOE Collaboration), *The tracking detector of the KLOE experiment*, Nucl. Instrum. Methods Phys. Res., Sect. A **488**, 51 (2002).
- [3] Louis Malter, *Thin Film Emission*, Phys. Rev. **50**, 48 (1936).
- [4] See *e.g.* G. Cataldi *et al.*, Nucl. Instrum. Methods Phys. Res., Sect. A **386**, 458 (1997); L. Cerrito *et al.*, Nucl. Instrum. Methods Phys. Res., Sect. A **436**, 336 (1999), and references therein.

5 Particle Identification

5.1 Detector Concept

The DIRC (Detector of Internally Reflected Cherenkov light) [1] is an example of innovative detector technology that has been crucial to the performance of the *BABAR* science program. Excellent flavor tagging will continue to be essential for the program of physics anticipated at Super*B*, and the gold standard of particle identification in this energy region is that provided by internally reflecting ring-imaging devices (the DIRC class of ring imaging detectors). The challenge for Super*B* is to retain (or even improve) the outstanding performance attained by the *BABAR* DIRC [2], while also gaining an essential factor of 100 in background rejection to deal with the much higher luminosity.

A new Cherenkov ring imaging detector is being planned for the Super*B* barrel, called the Focusing DIRC, or FDIRC. It will use the existing *BABAR* bar boxes and mechanical support structure. This structure will be attached to a new photon “camera”, which will be optically coupled to the bar box window. The new camera design combines a small modular focusing structure that images the photons onto a focal plane instrumented with very fast, highly pixelated, photon detectors (PMTs). These elements should combine to attain the desired performance levels while being at least 100 times less sensitive to backgrounds than the *BABAR* DIRC.

Several options are also under consideration for a possible PID detector in the forward direction. The design variables being considered should include: (a) modest cost, (b) small mass in front of the LYSO calorimeter, and (c) good PID coverage at low momenta by removing the dE/dx ambiguity in π/K separation near 1 GeV/ c . Presently, we are considering the following technologies: (a) “DIRC-like” time-of-flight (TOF) [3], (b) pixelated TOF [4] and (c) Aerogel RICH [5]. The aim is to design the best possible Super*B* detector by optimizing physics,

performance and cost, while being constrained to the existing *BABAR* geometry.

5.1.1 Charged Particle Identification at Super*B*

The charged particle identification at Super*B* relies on the same framework as the *BABAR* experiment. Electrons and muons are identified by the EMC and the IFR respectively, aided by dE/dx measurements in the inner trackers (SVT and DCH). Separation for low-momentum hadrons is primarily provided by dE/dx . At higher momenta (above 0.7 GeV/ c for pions and kaons, above 1.3 GeV/ c for protons), a dedicated system, the FDIRC – inspired by the successful *BABAR* DIRC – will perform the π/K separation. This new detector, described in Section 5.2, is expected to perform well over the entire momentum range for *B*-physics. But its geometrical coverage is limited to the barrel region. As discussed above, there is an ongoing effort to determine the physics impact of a forward PID system, together with an active R&D effort on possible detector technologies.

5.1.2 *BABAR* DIRC

The *BABAR* DIRC – see Fig. 16 – is a novel ring-imaging Cherenkov detector. The Cherenkov light angular information, produced in ultra-pure synthetic fused silica bars, is preserved while propagating along the bar via internal reflections to the camera (the SOB) where an image is produced and detected.

The entire DIRC has 144 quartz bars, each 4.9 m long, which are set along the beam line and cover the whole azimuthal range. Thanks to an internal reflection coefficient of ~ 0.9997 and orthogonal bar faces, Cherenkov photons are transported to the back end of the bars with the magnitude of their angles conserved and only a modest loss of photons. They exit into a pinhole camera consisting of a large volume of purified water (a medium chosen because it is inexpensive, transparent, and easy to clean, with average index of refraction and relative chromatic dispersion sufficiently close to those of the fused silica). The photon detector PMTs are located

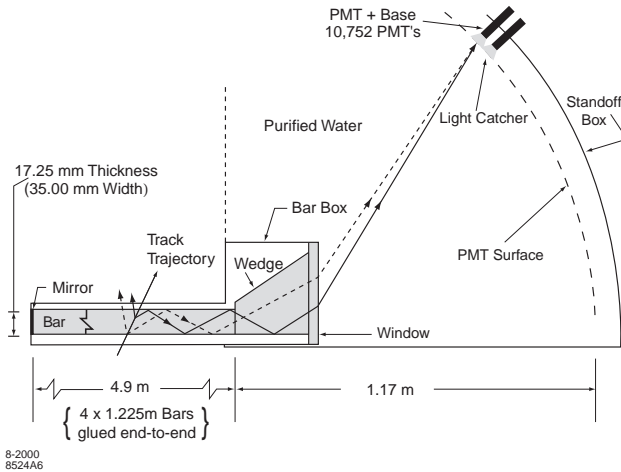


Figure 16: Schematic of the *BABAR* DIRC.

at the rear of the SOB, about 1.2 m away from the quartz bar exit window.

The reconstruction of the Cherenkov angle uses information from the tracking system together with the positions of the PMT hits in the DIRC. In addition, information on the time of arrival of hits is used in rejecting background hits, and resolving ambiguities.

The *BABAR* DIRC performed reliably and efficiently over the whole *BABAR* data taking period (1999–2007). Its physics performance remained consistent throughout the run period, although some upgrades, such as the addition of shielding and replacement of electronics, were necessary to cope with machine conditions. Its main performance parameters are the following:

- measured time resolution of about 1.7 ns, close to the PMT transit time spread of 1.5 ns;
- single photon Cherenkov angle resolution of 9.6 mrad for dimuon events;
- Cherenkov angle resolution per track of 2.5 mrad in dimuon events;
- $K - \pi$ separation above 2.5 ' σ ' from the pion Cherenkov threshold up to 4.2 GeV/ c .

5.2 Barrel PID at SuperB

5.2.1 Performance Optimization

As discussed above, the PID system in SuperB must cope with much higher luminosity-

related background rates than in *BABAR* – current estimates are on the order of 100 times higher. The basic strategy is to make the camera much smaller and faster. A new photon camera imaging concept, based on focusing optics, is therefore envisioned. The focusing blocks (FBLOCK), responsible for imaging the Cherenkov photons onto the PMT cathode surfaces, would be machined from radiation-hard pieces of fused silica. The major design constraints for the new camera are the following: (a) it must be consistent with the existing *BABAR* bar box design, as these elements will be reused in SuperB; (b) it must coexist with the *BABAR* mechanical support and magnetic field constraints; (c) it requires very fine photon detector pixelation and fast photon detectors.

Imaging is provided by a mirror structure focusing onto an image plane containing highly pixelated photomultiplier tubes. The reduced volume of the new camera and the use of fused silica for coupling to the bar boxes (in place of water as it was in *BABAR* SOB), is expected to reduce the sensitivity to background by about one order of magnitude compared to *BABAR* DIRC. The very fast timing of the new PMTs is expected to provide many additional advantages: (a) an improvement of the Cherenkov resolution; (b) a measure of the chromatic dispersion term in the radiator [6, 7, 8]; (c) separation of ambiguous solutions in the folded optical system; and (d), another order of magnitude improvement in background rejection.

Figure 17 shows the new FDIRC camera design (see Ref. [9] for more detail). It consists of two parts: (a) a focusing block (FBLOCK) with cylindrical and flat mirror surfaces, and (b) a new wedge. The wedge at the end of the bar rotates rays with large transverse angles (in the focusing plane) before they emerge into the focusing structure. The old wedge is too short so that an additional wedge element must be added to insure that all rays strike the cylindrical mirror. The cylindrical mirror is rotated appropriately to make sure that all rays reflect onto

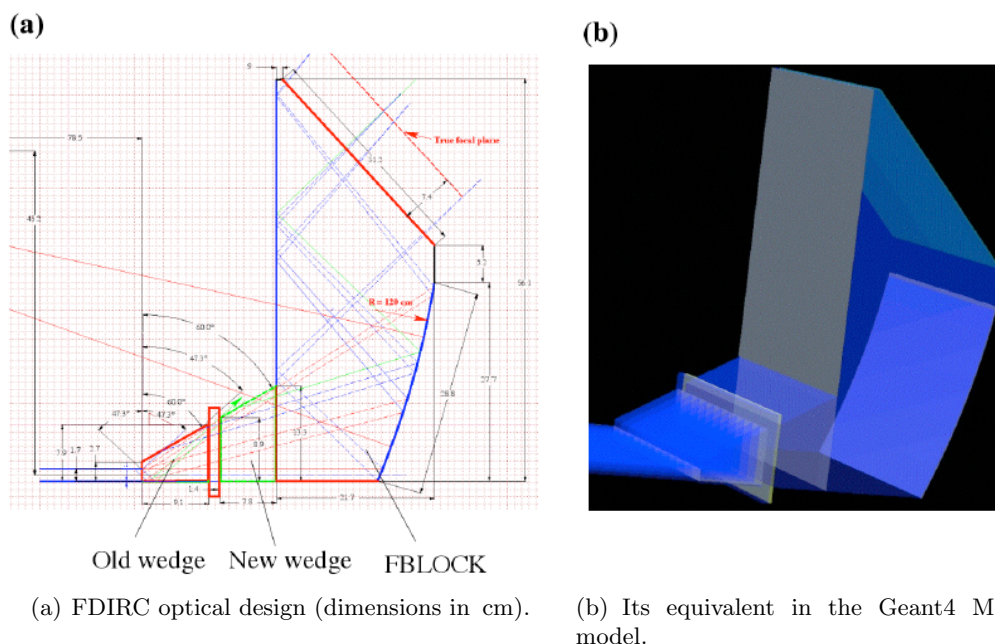


Figure 17: Barrel FDIRC Design.

the FBLOCK flat mirror, preventing reflections back into the bar box itself; the flat mirror then reflects rays onto the detector focal plane with an incidence angle of almost 90° , thus avoiding reflections. The focal plane is located in a slightly under-focused position to reduce the FBLOCK size and therefore its weight. Precise focusing is unnecessary, as the finite pixel size would not take advantage of it. The total weight of the solid fused silica FBLOCK is about 80kg. This significant weight requires good mechanical support.

There are several important advantages gained in moving from the *BABAR* pinhole focused design with water coupling to a focused optical design made of solid fused silica: (a) the design is modular; (b) sensitivity to background, especially to neutrons, is significantly reduced; (c) the pinhole-size component of the angular resolution in the focusing plane can be removed, and timing can be used to measure the chromatic dispersion, thus improving performance; (d) the total number of photomultipliers is reduced by about one half compared to a non-focusing design with equivalent perfor-

mance; (e) there is no risk of water leaks into the SuperB detector, and no time-consuming maintenance of a water system, as was required to operate *BABAR* safely.

Each new camera will be attached to its *BABAR* bar box with an optical RTV glue, which will be injected in a liquid form between the bar box window and the new camera and cure in place. As Fig. 17 shows, the cylindrical mirror focuses in the radial (y) direction, while pinhole focusing is used in the direction out of the plane of the schematic (the x -direction). Photons that enter the FBLOCK at large x -angles reflect from the parallel sides, leading to an additional ambiguity. However, the folded design makes the optical piece small, and places the photon detectors in an accessible location, improving both the mechanics and the background sensitivity. Since the optical mapping is 1 to 1 in the y -direction, this “folding” reflection does not create an additional ambiguity. Since a given photon bounces inside the FBLOCK only 2–4 times, the requirements on surface quality and polishing for the optical pieces are much less stringent than that required for the DIRC bar

FDIRC Design	Option	θ_C resolution [mrad]
1	3 mm \times 12 mm pixels with a micro-wedge	8.1
2	3 mm \times 12 mm pixels and no micro-wedge	8.8
3	6 mm \times 12 mm pixels with a micro-wedge	9.0
4	6 mm \times 12 mm pixels and no micro-wedge	9.6

Table 1: FDIRC performance simulation by Geant4 MC.

box radiator bars. This significantly reduces the cost of optical fabrication.

Each DIRC wedge inside an existing bar box has a 6 mrad angle at the bottom. This was done intentionally in *BABAR* to provide simple step-wise “focusing” of rays leaving the bar towards negative y to reduce the effect of bar thickness. However, in the new optical system, having this angle on the inner wedge somewhat worsens the design FDIRC optics resolution. There are two choices: (a) either leave it as it is, or (b) glue a micro-wedge at the bottom of the old wedge, inside the bar box, to correct for this angle. Though (b) is possible in principle, it is far from trivial, as the bar box must be opened.

The performance of the new FDIRC is simulated with a Geant4 based program [10]. Preliminary results for the expected Cherenkov angle resolution are shown in Table 1 for different layouts [10]. Design #1, which has emerged as the preferred one (a 3 mm \times 12 mm pixel size with the micro-wedge glued in) gives a resolution of ~ 8.1 mrad per photon for 4 GeV/c pions at 90° dip angle. This can be com-

pared with *BABAR* DIRC’s measured resolution of ~ 9.6 mrad per photon for di-muon events. If we decide not to glue in the micro-wedge (design #2), the resolution will increase to 8.8 mrad per photon *i.e.*, we lose about 0.7 mrad per photon. Going to a coarser pixelization of 6 mm \times 12 mm will worsen the Cherenkov angle resolution by ~ 1 mrad per photon (see designs #3 & #4). On the other hand, correcting for chromatic dispersion using timing information on each photon [6, 9, 11] may improve the FDIRC resolution by an additional 0.5–1 mrad per photon.

5.2.2 Design and R&D Status

Multianode Photomultiplier Tubes (MaPMT) made by Hamamatsu are the leading choice as photon detectors. They are highly pixelated and about 10 times faster than the *BABAR* DIRC PMTs. Their performance has been tested and proven in high rate environments such as the HERA-B experiment. Two PMT pixelation options are under consideration. A pixel size of 3 mm \times 12 mm can be achieved by shorting pads of the Hamamatsu 256-pixel H-9500 MaPMT, resulting in 64 readout channels per MaPMT. Figure 18(a) [11] shows the single photoelectron response of this tube with such pixelization, normalized to the Photonis Quantacon PMT. Each camera will have ~ 48 H-9500 MaPMT detectors, which corresponds to a total of ~ 576 for the entire SuperB FDIRC, or $\sim 36\,864$ pixels in the entire system. Another option – see Fig. 18(b) – is a pixel size of 6 mm \times 12 mm, which is achieved by shorting pads of the Hamamatsu 64-pixel H-8500 MaPMT, resulting in $64/2 = 32$ readout channels per MaPMT, *i.e.* half the total pixel count compared to the H-9500 choice.

Measurements with a prototype – a single bar FDIRC set up at SLAC [6, 7, 8] – confirm that the best Cherenkov angle resolution is achieved with a pixel size of 3 mm in the vertical direction and 12 mm in the horizontal direction, in agreement with the Monte Carlo. This configuration, combined with a good single photon timing resolution, is expected to provide superior Cherenkov angle resolution using the full three-

dimensional imaging available with the DIRC technique. Although the smaller pixels of the H-9500 MaPMT would lead to better performance, a potential advantage of the H-8500 MaPMT solution could be a higher quantum efficiency (QE). Moreover, given its wider use in the medical community, the manufacturer (Hamamatsu) is likely to focus efforts on this tube, leading to more reliable tubes at lower costs. For example, Hamamatsu can deliver H-8500 tubes reliably with $QE \sim 24\%$, which cannot be promised for the H-9500 tube at this point. Furthermore, the fabrication of H-9500 tubes is likely to extend over several years – up to 3.5 years, according to Hamamatsu itself. The final choice between the two MaPMTs will be made after further R&D.

Several options are being considered for the FDIRC electronics. One option is to couple a leading edge discriminator with a 100 ps/count TDC, together with an ADC to provide the pulse height corrections that are needed to improve timing resolution – aiming at a level of 150–200 ps per single photon. An alternative choice is to use waveform digitizing electronics, based either on the Waveform catcher concept [12] or the BLAB chip design [13]. The choice between these options will be made during the R&D period.

Figure 19 shows a possible design for the mechanical support. Each bar box is a separate module with its own FBLOCK support, light seal, and individual access for maintenance. Each FBLOCK, weighing almost 100kg, is supported on rods with ball bearings to provide precise control as it is mated to the bar box. The optical coupling between the FBLOCK and the bar box is done with an RTV coupling. Similarly, detectors are coupled to FBLOCK with an RTV cookie. There is a common magnetic shield mounted on hinges to allow easy access to the detector.

Tests of a number of these electronic scenarios continue in the SLAC cosmic ray telescope (CRT) [14] with the FDIRC single bar prototype. We plan to set up a full size DIRC bar box equipped with the new focusing optics to

run in the cosmic ray telescope in 2010-11. In parallel, we intend to revive a scanning setup to test photodetectors with the new electronics. Test bench setups are also planned at LAL-Orsay and the University of Maryland.

Finally, a summary budget projecting the costs of the barrel FDIRC can be found in Section 11.

5.3 Forward PID at SuperB

5.3.1 Motivation for a Forward PID Detector

Though the barrel FDIRC detector combined with dE/dx from the DCH provides good $\pi - K$ separation up to about 4 GeV/c, hadron identification in the forward and backward regions in SuperB is limited unless dedicated PID devices are added there. Any such device needs to cover the “cross-over” π/K ambiguity region for dE/dx near 1 GeV/c, and should also provide high momentum π/K separation at higher momenta where the dE/dx separation is rather poor (less than 2σ). Cluster counting in the DCH, if incorporated in SuperB, could provide adequate PID at the high momentum, but, of course, the cross-over ambiguity would remain.

Improved PID performance over the entire detector solid angle increases the event reconstruction efficiency in various exclusive B -channels and helps to reduce specific backgrounds. In addition, the reconstruction of hadronic and semi-leptonic B channels – a key ingredient of recoil physics analyses – would be improved. For some of these channels, the reconstruction efficiencies and the purities improve significantly – the higher the number of charged particles in the reconstructed final states, the faster the gain. Dedicated Monte-Carlo studies aiming at quantifying these improvements are ongoing within the SuperB (DGWG).

The momenta of backward-going tracks in SuperB is quite low on average. The EMC group is proposing a backward veto calorimeter which may be fast enough to provide significant $\pi - K$ separation using TOF which might provide an inexpensive approach to PID in this region; R&D continues.

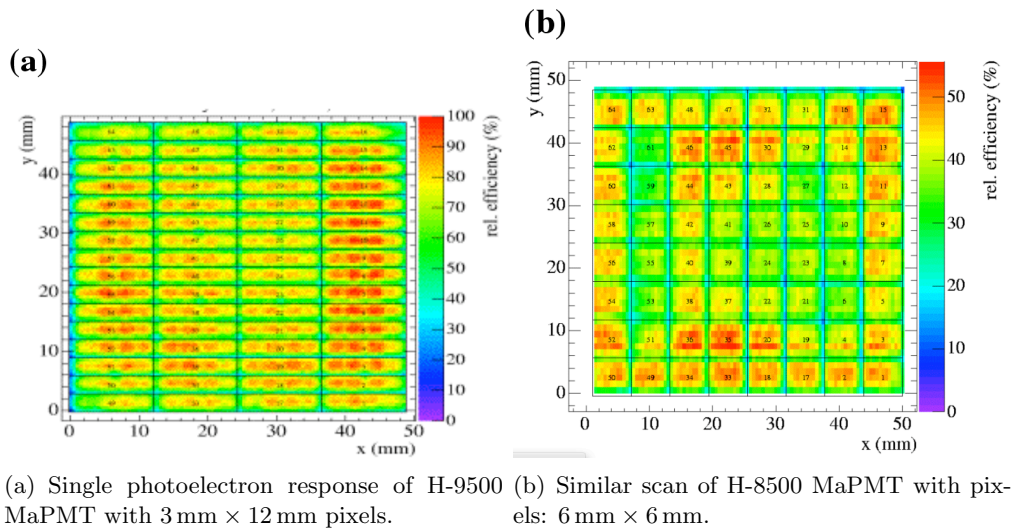
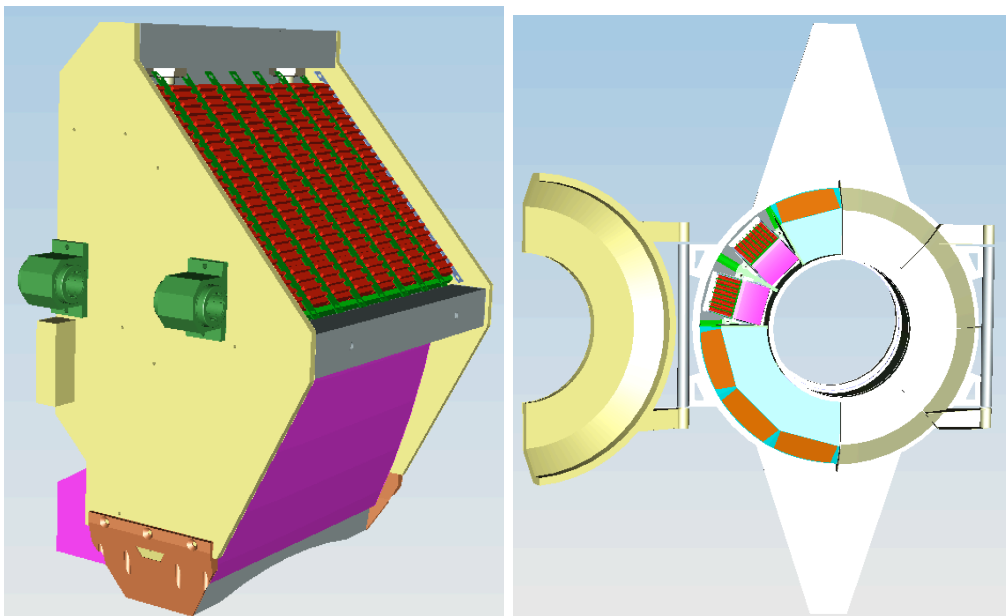


Figure 18: Single photoelectron response of MaPMTs.



(a) Mechanical enclosure and support of the FBLOCK with the new wedge. (b) Overall mechanical support design with the new magnetic shield door.

Figure 19: Possible mechanical design for the FDIRC.

The forward region covers a larger fraction of the SuperB geometrical acceptance than the backward because of the boost, although it is still less than 10% of the total. Another consequence of the beam energy asymmetry is that the particles crossing this region have higher average momenta. With the help of the DGWG the SuperB PID group is investigating the option of adding forward PID coverage in detail. The status of this ongoing R&D effort is reported in the following Section 5.3.3.

5.3.2 Forward PID Requirements

The physics performance goals for a forward PID detector are to cover the π/K ambiguity near 1 GeV/c, and, if possible, to extend the region with good π/K separation up to 3 GeV/c or even above. Space is quite limited in the forward area so any such SuperB detector should be compact. A reasonable goal is a thickness of ~ 10 cm. A thicker device requires either a shorter DCH, a forward shift of the EMC, or both, which, in turn, lead to (typically modest) performance degradation for these devices. Moreover, the radiation length (X_0) of this new device should be kept as low as possible, in order to avoid degrading the reconstruction of electromagnetic showers in the EMC endcap, and the mass should be located as close as possible to the EMC. Finally, the cost of such a detector must be small with respect to the cost of the barrel PID, somehow in proportionality to their relative solid angle coverage.

5.3.3 Status of the Forward PID R&D Effort

Three designs for forward PID detectors are currently being investigated: a “DIRC-like” time-of-flight device, a “pixelated” time-of-flight detector and a Focusing Aerogel RICH, the “FARICH”.

“DIRC-like” time-of-flight detector concept

In this scheme [3], charged tracks cross a thin layer of quartz in which Cherenkov photons are emitted along the particle trajectories, at the

Cherenkov polar angle. These photons are then transported through internal reflections to one side of the quartz volume where they are detected by PMTs located outside of the SuperB acceptance. Unlike the DIRC, no attempt is made to measure the Cherenkov angle directly. Instead, PID separation is provided by TOF: at a given momentum, kaons fly more slowly than pions, as they are heavier. This method is challenging for several reasons, including the limited number of photons detected, and possible pattern recognition issues in the expected high background environment. Moreover, the whole detector chain (the hardware and the reconstruction software) must be very precisely calibrated: for instance, 3 GeV/c kaon and pion are only separated by about 90 ps after 2 m – roughly the expected particle flight distance in the current SuperB layout. On the other hand, such a detector is potentially attractive as it should fit without problems into the available space between the DCH and EMC. But the X_0 of this detector is the smallest and most uniform of the proposed layouts, and it requires a modest number of readout channels.

Figure 20 shows the current layout of the “DIRC-like” time-of-flight (TOF) detector, as implemented in Geant4-based simulations. Twelve tiles (1–2 cm thick) of fused silica provide good azimuthal coverage of the forward side of the SuperB detector. The photons are transported inside the fused silica volume until the inner part of the tile where they are detected by MCP-PMTs. Simulations are in progress to understand and optimize the detector response to signal Cherenkov photons.

In addition, R&D programs are currently ongoing at the University of Hawaii and LAL-Orsay in order to design waveform-digitizing electronics which would be able to fulfill the timing accuracy requirements of this detector (a few tens of ps at most) while being affordable and robust. Finally, as this apparatus would have to fit into a very limited space, detailed mechanical integration studies have started at LAL, in connection with the inner (DCH) and outer (EMC) subsystems.

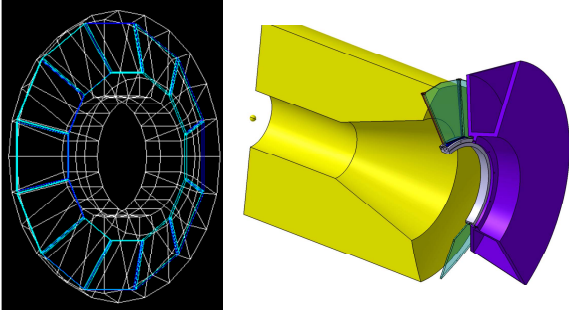


Figure 20: Left: the “DIRC-like” TOF design, as currently implemented in Geant4 simulations. Right: a possible design for the mechanical integration of this detector (in green) in SuperB. The yellow (magenta) volumes represent the envelope of the DCH (forward EMC).

“Pixelated” time-of-flight detector concept

In this design, Cherenkov light is also produced in a quartz radiator [4]. However, in this case the radiator is made of quartz cubes, which couple directly onto matching pixelated photodetectors that cover the entire detector surface. No photon tracking is required. This layout makes the reconstruction much easier (a given track would only produce light in a particular pixel whose location would be predicted by the tracking algorithms); it is insensitive to chromatic time broadening; and it is less sensitive to background as it runs at low gain and is insensitive to single photoelectron background. On the other hand, the radiation length X_0 is larger, as the photodetectors and the electronics are located in front of the EMC calorimeter. In addition, PMTs with excellent timing resolution (such as MCP-PMTs) that are able to operate in a 16kG magnetic field are very expensive. The PID performance depends on the timing resolution obtained. It should be possible, but challenging, to reach resolutions of 30 ps or better, leading to $\sim 3\sigma$ separation for

3 GeV/c pions and kaons. As a much lower cost alternative, we are looking into pixelated TOF devices that would use photon detectors based on G-APD arrays or mesh PMTs, coupled to radiators such as LYSO, quartz or a fast plastic scintillator, with a more modest resolution goal of ~ 100 ps. This would be sufficient to provide π/K separation near 1 GeV/c (where dE/dx is useless) and help below 700 MeV/c. However, higher momentum PID would be only that provided by dE/dx .

FARICH concept The FARICH detector [5] uses a 3-layer aerogel radiator with focusing effect for high momentum separation and a water radiator to cover the low momentum region. The Cherenkov light is detected by a wall of pixelated MCP-PMTs. MC simulations predict π/K separation at the 3 ‘ σ ’ level or better up to 5 GeV/c, with μ/π separation up to 1 GeV/c. The amount of material is similar to the “pixelated” time-of-flight design while the number of channels is 4 times larger. The FARICH has the best high momentum PID performance of all detectors proposed for the forward direction – it is even “too good” at high momenta. Its main drawbacks are thickness, mass, cost, and absence of beam test results.

References

- [1] B. Ratcliff, SLAC-PUB-5946, 1992; and *Simple considerations for the SOB re-design for SuperB*, <http://agenda.infn.it/conferenceDisplay.py?confId=458>, SuperB PID meeting, March 18, 2008.
- [2] I. Adam *et al.*, Nucl. Instrum. Methods Phys. Res., Sect. A **583**, 281 (2007).
- [3] J. Va’vra, <http://agenda.infn.it/conferenceDisplay.py?confId=1161>, Perugia, June 2009, and <http://agenda.infn.it/conferenceDisplay.py?confId=1742>, October 2009, SLAC.
- [4] J. Va’vra *et al.*, Nucl. Instrum. Methods Phys. Res., Sect. A **606**, 404 (2009).

- [5] S.Korpar *et al.*, Nucl. Instrum. Methods Phys. Res., Sect. A **553**, 64 (2005); A. Yu. Barnyakov *et al.*, Nucl. Instrum. Methods Phys. Res., Sect. A **553**, 70 (2005); and E. Kravchenko, <http://agenda.infn.it/conferenceDisplay.py?confId=1161>, June 2009, Perugia.
- [6] J. Benitez *et al.*, SLAC-PUB-12236, October 2006.
- [7] J. Va'vra *et al.*, SLAC-PUB-12803, March 2007.
- [8] J. Benitez *et al.*, Nucl. Instrum. Methods Phys. Res., Sect. A **595**, 104 (2008).
- [9] J. Va'vra, *Simulation of the FDIRC optics with Mathematica*, SLAC-PUB-13464, 2008; and *Focusing DIRC design for SuperB*, SLAC-PUB-13763, 2009.
- [10] D. Roberts, *Geant4 model of FDIRC*, <http://agenda.infn.it/conferenceDisplay.py?confId=1742>, October 2009, SLAC.
- [11] C. Field *et al.*, *Development of Photon Detectors for a Fast Focusing DIRC*, SLAC-PUB-11107, 2004.
- [12] D. Breton, E. Delagnes and J. Maalmi, *Picosecond time measurement using ultra fast analog memories*, talk and proceedings at TWEPP-09, Paris, September 2009.
- [13] G. Varner, Nucl. Instrum. Methods Phys. Res., Sect. A **538**, 447 (2005).
- [14] J. Va'vra, *SLAC cosmic ray telescope facility*, SLAC-PUB-13873, Jan. 2010.

6 Electromagnetic Calorimeter

The Super*B* electromagnetic calorimeter (EMC) provides energy and direction measurement of photons and electrons, and is an important component in the identification of electrons versus other charged particles. The system contains three components, shown in Fig. 1: the barrel calorimeter, reused from *BABAR*; the forward endcap calorimeter, replacing the *BABAR* forward endcap; and the backward endcap calorimeter, a new device improving the backward solid angle coverage. Table 2 details the solid angle coverage of each calorimeter. The total solid angle covered for a massless particle in the center-of-mass (CM) is 94.1% of 4π .

In addition to the *BABAR* simulation for the barrel calorimeter, simulation packages for the new forward and backward endcaps have been developed, both in the form of a full simulation using the Geant4 toolkit and in the form of a fast simulation package for parametric studies. These packages are used in the optimization of the calorimeter and to study the physics impact of different options.

6.1 Barrel Calorimeter

The barrel calorimeter for Super*B* is the existing *BABAR* CsI(Tl) crystal calorimeter.[1] Estimated rates and radiation levels indicate that this system will continue to survive and function in the Super*B* environment. It covers 2π in azimuth and polar angles from 26.8° to 141.8° in the lab. There are 48 rings of crystals in polar angle, with 120 crystals in each azimuthal ring, for a total of 5,760 crystals. The crystal length ranges from $16X_0$ to $17.5X_0$. They are read out by two redundant PIN diodes connected to a multi-range amplifier. A source calibration system allows calibrating the calorimeter with 6.13 MeV photons from the ^{16}N decay chain. The *BABAR* barrel calorimeter will be largely unchanged for Super*B*; we indicate planned changes below.

Adding one more ring of crystals at the backward end of the barrel is under consideration. These crystals would be obtained from the current *BABAR* forward calorimeter, that will not be reused in Super*B*. Space is already available for the additional crystals in the existing mechanical structure, although some modification would be required to accommodate the additional readout.

The existing barrel PIN diode readout is kept at Super*B*. In order to accommodate the higher event rate, the shaping time is decreased. The existing ‘‘CARE’’ chip [2] covers the required dynamic range by providing four different gains to be digitized in a ten-bit ADC. However, this system is old, and the failure rate of the analog-to-digital boards (ADBs) is unacceptably high. Thus, a new ADB has been designed, along with a new analog board, the Very Front End (VFE) board, shown in Fig. 21. The new design incorporates a dual-gain amplifier, followed by a twelve-bit ADC. In order to provide good least-count resolution on the 6 MeV calibration source, an additional calibration range is provided on the ADB. The existing PIN diodes, with their redundancy, are expected to continue to perform satisfactorily. They are epoxied to the crystals and changing them would be a difficult operation.

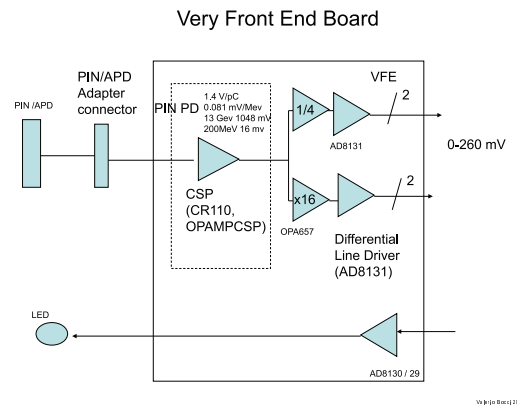


Figure 21: Block diagram for the Very Front End board, for the barrel and forward endcap signal readout.

Table 2: Solid angle coverage of the electromagnetic calorimeters. Values are obtained assuming the barrel calorimeter is in the same location with respect to the collision point as for *BABAR*. The CM numbers are for massless particles and nominal 4 on 7 GeV beam energies. The barrel Super*B* row includes one additional ring of crystals over *BABAR*.

Calorimeter	$\cos\theta$ (lab)		$\cos\theta$ (CM)		Ω (CM)(%)
	minimum	maximum	minimum	maximum	
Backward	-0.974	-0.869	-0.985	-0.922	3.1
Barrel (<i>BABAR</i>)	-0.786	0.893	-0.870	0.824	84.7
Barrel (Super <i>B</i>)	-0.805	0.893	-0.882	0.824	85.2
Forward	0.896	0.965	0.829	0.941	5.6

Table 3: Layout of the forward endcap calorimeter.

Group	Modules	Crystals
1	36	900
2	42	1050
3	48	1200
4	54	1050
Total		4500

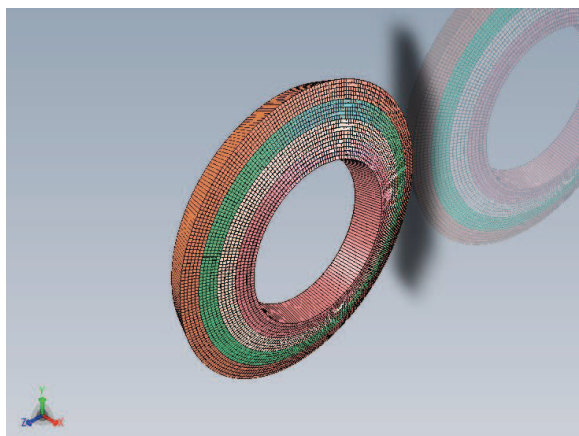


Figure 22: Arrangement of the LYSO crystals in groups of rings.

6.2 Forward Endcap Calorimeter

The forward electromagnetic calorimeter for Super*B* is a new device replacing the *BABAR* CsI(Tl) forward calorimeter, with coverage starting at the end of the barrel and extending

down to 270 mrad ($\cos\theta = 0.965$) in the laboratory. Because of the increased background levels, a faster and more radiation hard material, such as LYSO or pure CsI, is required in the forward calorimeter. The baseline design is based on LYSO (Lutetium Yttrium Orthosilicate, with Cerium doping) crystals. The advantages of LYSO include a much shorter scintillation time constant (LYSO: 40 ns, CsI(Tl): 680 ns and $3.34\mu\text{s}$), a smaller Molière radius (LYSO: 2.1 cm, CsI: 3.6 cm), and greater resistance to radiation damage. One radiation length is 1.14 cm in LYSO and 1.86 cm in CsI. An alternative choice is pure CsI [3]. However, the light output is much smaller, making LYSO preferable.

There are 20 rings of crystals, arranged in four groups of 5 layers each. The crystals maintain the almost projective geometry of the barrel. Each group of five layers is arranged in modules five crystals wide. The preferred endcap structure is a continuous ring. However, the numbers of modules in each group of layers are multiples of 6, allowing the detector to be split in two halves, should that be necessary from installation considerations. The grouping of crystals is summarized in Table 3 and illustrated in Fig. 22.

Each crystal is up to $2.5 \times 2.5\text{ cm}^2$ at the back end, with a projective taper to the front. The maximum transverse dimensions are dictated by the Molière radius and by the desire to obtain two crystals from a boule. The length of each crystal is approximately 20 cm, or $17.5X_0$.

6.2.1 Mechanical Structure

The support for the crystals is an alveolar structure (*i.e.*, a sort of egg-crate structure, with a cell for each crystal) constructed of either carbon fiber or glass fiber and bounded by two conical structures at the radial extremes. To minimize the dead material between the endcap and the barrel, the outer cone is made of carbon fiber with a thickness between 6 and 10 mm. The inner cone is instead made of 20 to 30 mm-thick aluminum.

With the inclusion of the source calibration system, described below, and the front cooling system, the total front wall thickness may reach 20–30 mm. A good solution that minimizes material in front of the calorimeter is to embed the pipes into the foam core of a sandwich panel completed by two skins of 2–3 mm carbon fiber. A lighter alternative under investigation is to use depressions in pressed aluminum sheets forming the two skins of the front wall to form the calibration and cooling circuits. The support at the back, providing the load-bearing support for the forward calorimeter, is constructed in stainless steel as either an open frame or closed plate.

6.2.2 Readout System

Two possible readouts are under study: PIN diodes as used in the barrel and APDs (Avalanche Photodiodes). As for the barrel, redundancy is achieved with 2 APDs or PIN diodes per crystal. APDs, with a low-noise gain of order 50, offer the possibility of measuring signals from sub-MeV radioactive sources. This would obviate the need for a step with photomultipliers during the uniformity measurement process during calorimeter construction. A concern in the SuperB environment is the nuclear counter effect from background neutrons. APDs also have an advantage over PIN diodes here. Nevertheless, it may be desirable to use the redundant photodetectors with a comparator arrangement to eliminate spurious large signals due to this background. This is under investigation. The disadvantage of APDs is the gain

dependence on temperature, which can be of order 2%/°C (e.g. [4]). This requires tight control of the readout temperature. The same electronics as for the barrel is used, with an adjustment to the VFE board gain with the APD choice.

6.2.3 Calibration and Beam Test

The source calibration system is a new version of the 6.13 MeV calibration system already used in *BABAR*. This system uses a neutron generator to produce activated ^{16}N from fluorine in Fluorinert [5] coolant. The activated coolant is circulated near the front of the crystals in the detector, where the ^{16}N decays with a 7 s half-life. The 6.13 MeV photons are produced in the decay chain $^{16}\text{N} \rightarrow ^{16}\text{O}^* + \beta$, $^{16}\text{O}^* \rightarrow ^{16}\text{O} + \gamma$.

Two beam tests are planned to study the LYSO performance and the readout options. The first beam test is at Frascati's Beam Test Facility, covering the 50–500 MeV energy range. The second beam test is at CERN, to cover the GeV energy range. In addition, a prototype alveolar support structure is being constructed for the beam test.

6.2.4 Performance Studies

Simulation studies are underway to optimize the detector configuration. It is important to use a realistic clustering algorithm in these studies, since in actual events multiple particles can overlap, requiring clever pattern recognition. Fig. 23 shows how the measured energy distribution changes for different reconstruction algorithms.

Particular attention has been devoted to the study of the effect of material in front of the forward calorimeter, for instance due to a proposed forward PID device. Material in front of the calorimeter enhances the low-energy tail of the measurement, although peak width measures, such as the FWHM, are almost unaffected, as shown in Fig. 24. for the cases of 25 and 60 mm of quartz in front of the calorimeter.

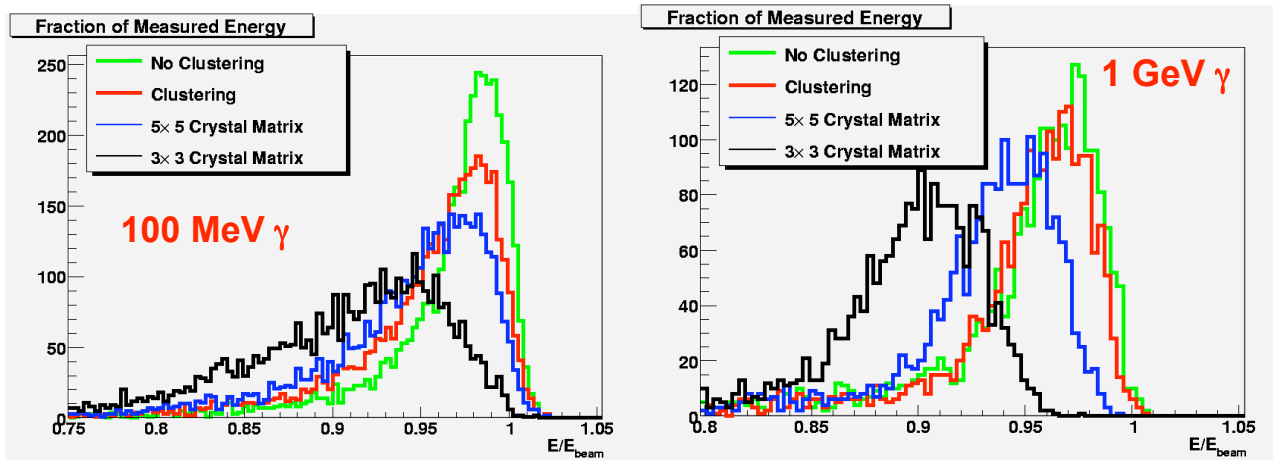


Figure 23: Effect on the measured energy distribution for various reconstruction algorithms. The “No clustering” distribution results from simply adding all crystal energies greater than 1 MeV. The “Clustering” distribution results from the algorithm used in *BABAR*. The curves labeled 5×5 crystal matrix and 3×3 crystal matrix are simple sums of energy deposits in 25 or 9 crystals, respectively, centered on the crystal with the most energy. Left: 100 MeV photons; Right: 1 GeV photons.

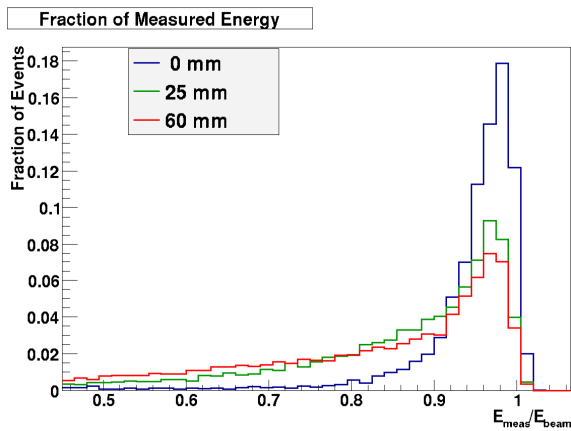


Figure 24: Ratio of the measured/beam energy in the forward calorimeter for 100 MeV photons and two different thickness of quartz, as well as no quartz, in front of the calorimeter.

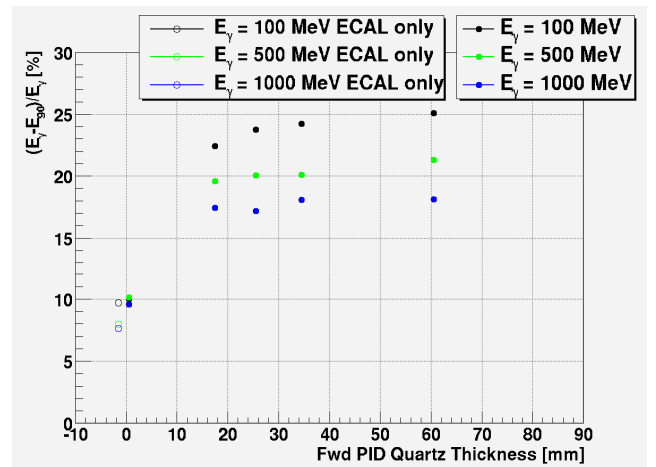


Figure 25: The effect of quartz material in front of the forward calorimeter, as a function of thickness and photon energy. The ordinate is f_{90} , explained in the text, expressed as per cent.

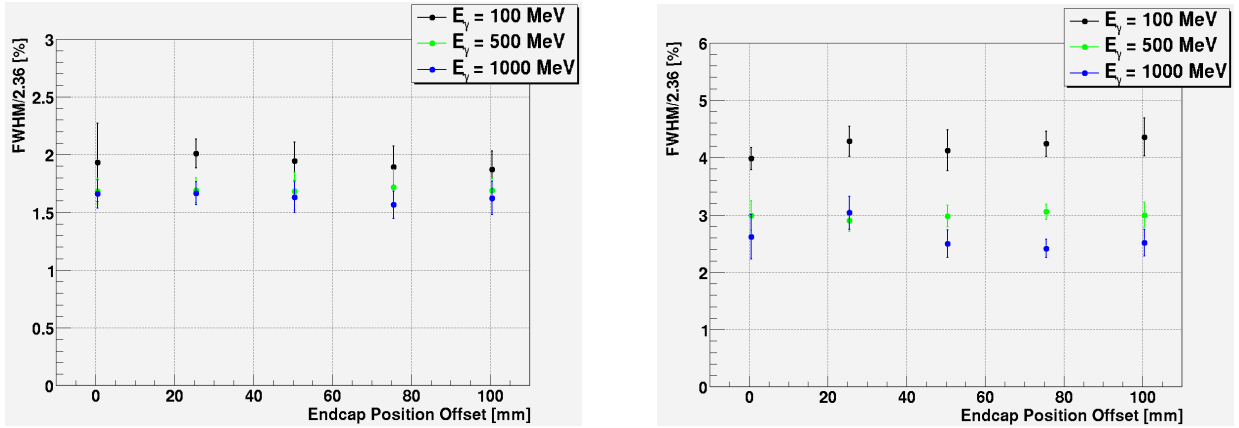


Figure 26: Effect on resolution of z-position of forward calorimeter. Left: Resolution as a function of position for showers away from the edges of the forward calorimeter. Right: Resolution as a function of position for showers in the transition region between the barrel and forward calorimeters. Note the different scales.

A more meaningful measure that we may use is:

$$f_{90} \equiv \frac{E_{\text{true}} - E_{90}}{E_{\text{true}}},$$

where E_{true} is the energy of the generated photon and E_{90} gives the 90% quantile of the measured energy distribution, *i.e.*, 90% of measurements of the photon energy are above this value. Fig. 25 shows the effect on the f_{90} measure of resolution as a function of the quartz thickness.

Ideally, the transition between the barrel and forward calorimeters should be smooth, in order to contain the electromagnetic showers and to keep pattern recognition simple. Some possibilities for particle identification however require the forward calorimeter to be moved back from the IP relative to the smooth transition point. The effect of this on photon energy resolution has been studied, see Fig. 26. The resolution degrades in the barrel-endcap transition region as expected, but there is substantially no dependence on the z-position.

6.3 Backward Endcap Calorimeter

The backward electromagnetic calorimeter for SuperB is a new device with the principal intent of improving hermeticity at modest cost. Excellent energy resolution is not a requirement,

since there is significant material from the drift chamber in front of it. Thus a high quality crystal calorimeter is not planned for the backward region. The proposed device is based on a multi-layer lead-scintillator stack with longitudinal segmentation providing capability for π/e separation.

The backward calorimeter is located starting at $z = -1320$ mm, allowing room for the drift chamber front end electronics. The inner radius is 310 mm, and the outer radius 750 mm. The total thickness is $12X_0$. It is constructed from a sandwich of 2.8 mm Pb alternating with 3 mm plastic scintillator (*e.g.*, BC-404 or BC-408). The scintillator light is collected for readout in wavelength-shifting fibers (*e.g.*, 1 mm Y11).

To provide for transverse spatial shower measurement, each layer of scintillator is segmented into strips. The segmentation alternates among three different patterns for different layers:

- Right-handed logarithmic spiral;
- Left-handed logarithmic spiral; and
- Radial wedge.

This set of patterns is repeated eight times to make a total of 24 layers. With this arrangement, the fibers all emerge at the outer radius

of the detector. There are 48 strips per layer, for a total of 1152 strips. The strip geometry is illustrated in Fig. 27.

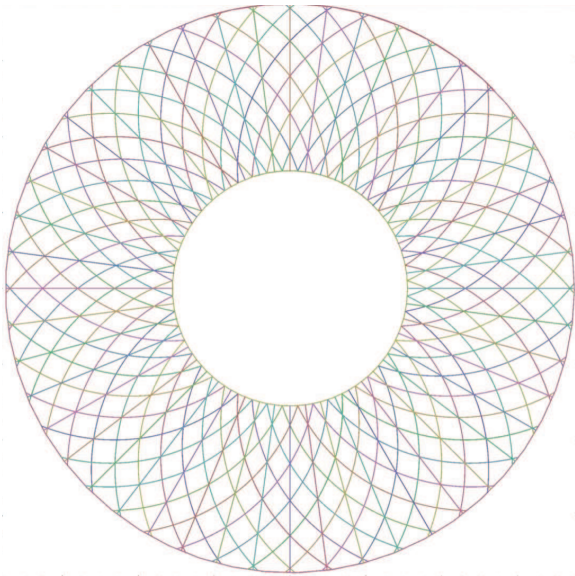


Figure 27: The backward EMC, showing the scintillator strip geometry for pattern recognition.

It is desirable to maintain mechanical integrity by constructing the scintillator layers with several strips from a single piece of scintillator, and not completely severing them. Isolation is achieved by cutting grooves at the strip boundaries. The optimization of this with respect to cross-talk and mechanical properties is under investigation.

The readout fibers are embedded in grooves cut into the scintillator. Each fiber is read out at the outer radius with a $1 \times 1 \text{ mm}^2$ multi-pixel photon counter (MPPC, or SiPM, for “silicon photomultiplier”) [6]. A mirror is glued to each fiber at the inner radius to maximize light collection. The SPIROC (SiPM Integrated Read-Out Chip) integrated circuit [7] developed for the ILC is used to digitize the MPPC signals, providing both TDC (100 ps) and ADC (12 bit) capability. Each chip contains 36 channels.

A concern with the MPPCs is radiation hardness. Degradation in performance is observed

in studies performed for the SuperB IFR, beginning at integrated doses of order 10^8 1-MeV-equivalent neutrons/ cm^2 [8]. This needs to be studied further, and possibly mitigated with shielding.

Simulation studies are being performed to investigate the performance gain achieved by the addition of the backward calorimeter. The $B \rightarrow \tau\nu_\tau$ decay presents an important physics channel where hermeticity is a significant consideration. The measurement of the branching fraction has been studied in simulations to evaluate the effect of the backward calorimeter. Events in which one B decays to $D^0\pi$, with $D^0 \rightarrow K^-\pi^+$, are used to tag the events, and several of the highest branching fraction one-prong τ decays are used.

Besides the selection of the tagging B decay, and one additional track for the τ , the key selection criterion is on E_{extra} , the energy sum of all remaining clusters in the EMC. This quantity is used to discriminate against backgrounds by requiring events to have low values; a reasonable criterion is to accept events with $E_{\text{extra}} < 400 \text{ MeV}$.

In this study we find that the signal-to-background ratio is improved by approximately 20% if the backward calorimeter is present (Fig. 28). The corresponding improvement in precision ($S/\sqrt{S+B}$) for 75 ab^{-1} is approximately 8% (Fig. 3). We note that only one tag mode has so far been investigated, and this study is ongoing with work on additional modes to obtain results for a more complete sample analysis. Also, the effect of background events superimposed on the physics event has not been fully studied.

The possibility of using the backward endcap for particle identification as a time-of-flight measuring device is also under investigation. Figure 29 shows, for example, for 100 ps timing resolution, a separation of more than three standard deviations (σ) can be achieved for momenta up to $1 \text{ GeV}/c$ and approximately 1.5σ up to $1.5 \text{ GeV}/c$.

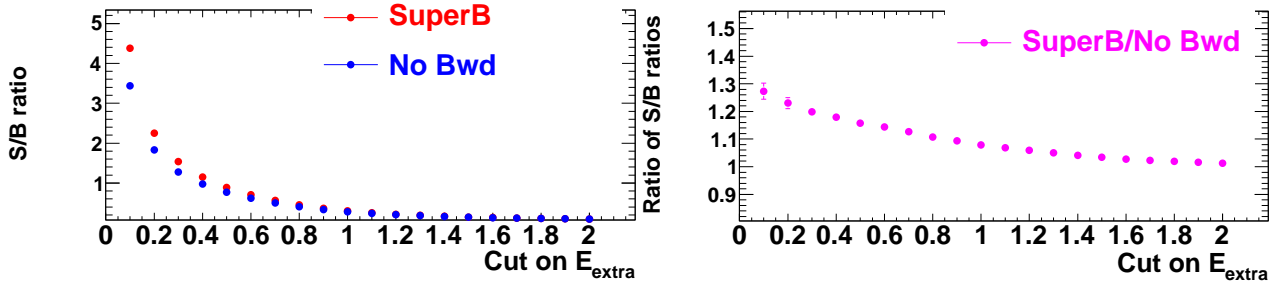


Figure 28: Left: Signal-to-background ratio with and without a backward calorimeter, as a function of the E_{extra} selection. Right: Ratio of the S/B ratio with a backward calorimeter to the S/B ratio without a backward calorimeter, as a function of the E_{extra} selection.

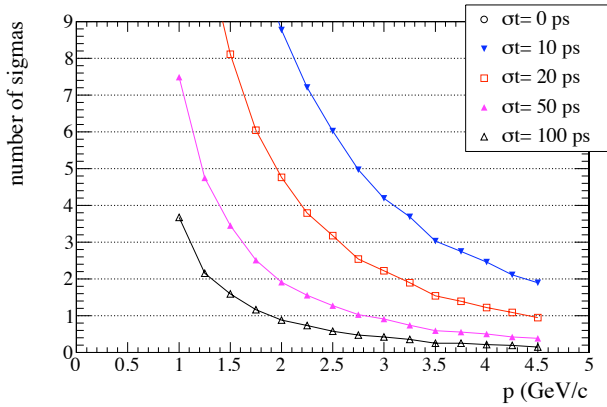


Figure 29: Kaon-pion separation versus measured momentum for different timing resolutions in the backward EMC region. The finite separation for perfect timing resolution is because measured momentum is used.

6.4 R&D

6.4.1 Barrel Calorimeter

The main R&D question for the barrel concerns the shaping time. Simulation work is underway to investigate pile-up effects from backgrounds. In addition, electronics and software issues connected with the possibility of adding one more ring of CsI crystals at the back end are still to be addressed.

6.4.2 Forward Calorimeter

Since the forward calorimeter is a new device, two beam tests are planned to test the performance of an LYSO crystal array as well as the solutions for the electronics and mechanical designs. The beam tests will also investigate the use of PIN diodes and APDs as readout options as well as the effect of material in front of the crystals in the beam test. Simulation work is ongoing to predict performance and backgrounds. Possible modifications to the electronics design to deal with neutron nuclear-counter signals in the photodetector will be investigated. There is an ongoing R&D effort with vendors to produce crystals with good light output and uniformity at an acceptable cost. The crystal support and integration of the calibration and cooling circuits with the mechanical structure is under investigation in consultation with vendors.

6.4.3 Backward Calorimeter

A beam test of the backward calorimeter is also planned, probably concurrent with the forward calorimeter beam test at CERN. The mechanical support and segmentation of the plastic scintillator is being investigated for a solution that achieves simplicity and acceptable cross-talk. The use of multi-pixel photon counters is being studied, including the radiation damage issue. The timing resolution for a possible time-of-flight measurement is an interesting question. Further simulation studies are being

made to characterize the performance impact of the backward calorimeter.

References

- [1] B. Aubert *et al.* (BABAR Collaboration), *The BABAR Detector*, Nucl. Instrum. Methods Phys. Res., Sect. A **479**, 1 (2002) [arXiv:hep-ex/0105044].
- [2] G. Haller and D. Freytag, IEEE Trans. Nucl. Sci. **43**, 1610 (1996).
- [3] I. Nakamura, *Belle Electromagnetic Calorimeter and its sBelle Upgrade*, J. Phys. Conf. Ser. **169**, 012003 (2009).
- [4] CMS ECAL Technical Design Report, CERN/LHCC 97-33 (1997), http://cms-ecal.web.cern.ch/cms-ecal/ECAL_TDR/ref/C4_P107-116.pdf.
- [5] Fluorinert is the trademark name for polychlorotrifluoro-ethylene), manufactured by 3M Corporation, St. Paul, MN, USA.
- [6] Hamamatsu S10362-11 series MPPC, http://jp.hamamatsu.com/resources/products/ssd/pdf/s10362-11series_kapd1022e05.pdf.
- [7] M. Bouchel, *et al.*, *SPIROC (SiPM Integrated Read-Out Chip): Dedicated very front-end electronics for an ILC prototype hadronic calorimeter with SiPM read-out*, NSS '07 IEEE **3**, 1857 (2007).
- [8] M. Angelone *et al.*, *Silicon Photo-Multiplier radiation hardness tests with a beam controlled neutron source*, arXiv:1002.3480 [physics.ins-det].

7 Instrumented Flux Return

The Instrumented Flux Return (IFR) is designed primarily to identify muons, and, in conjunction with the electromagnetic calorimeter, to identify neutral hadrons, such as K_L^0 . This section describes the performance requirements and a baseline design for the IFR. The iron yoke of the detector magnet provides the large amount of material needed to absorb hadrons. The yoke, as in the *BABAR* detector, is segmented in depth, with large area particle detectors inserted in the gaps between segments, allowing the depth of penetration to be measured.

In the *SuperB* environment, the critical regions for backgrounds are the small polar angle sections of the endcaps and the edges of the barrel internal layers, where we estimate that in the hottest regions the rate is a few hundred Hz/cm². These rates are too high for gaseous detectors. While the *BABAR* experience with both RPCs and LSTs has been, in the end, positive, detectors with high rate capability are required in the high background regions of *SuperB*. A scintillator-based system provides much higher rate capability than gaseous detectors, and therefore the baseline technology choice for the *SuperB* detector is extruded plastic scintillator using wavelength shifting (WLS) fibers read out with avalanche photodiode pixels operated in Geiger mode. The following subsections describe in detail all the components.

The IFR system must have high efficiency for selecting penetrating particles such as muons, while at the same time rejecting charged hadrons (mostly pions and kaons). Such a system is critical in separating signal events in $b \rightarrow s\ell^+\ell^-$ and $b \rightarrow d\ell^+\ell^-$ processes from background events originating from random combinations of the much more copious hadrons. Positive identification of muons with high efficiency is also important in rare B decays such as $B \rightarrow \tau\nu_\tau(\gamma)$, $B \rightarrow \mu\nu_\mu(\gamma)$ and $B_d(B_s) \rightarrow \mu^+\mu^-$ and in the search for lepton flavour-violating processes such as $\tau \rightarrow \mu\gamma$. Background suppression

in reconstruction of final states with missing energy carried by neutrinos (as in $B \rightarrow \mu\nu_\mu(\gamma)$) can benefit from vetoing the presence of energy carried by neutral hadrons. In the *BABAR* detector, about 45% of relatively high momentum K_L^0 s interacted only in the IFR system. A K_L^0 identification capability is therefore required.

7.1 Performance Optimization

7.1.1 Identification Technique

Muons are identified by measuring their penetration depth in the iron of the return yoke of the solenoid magnet. Hadrons shower in the iron, which has a hadronic interaction length $\lambda_I = 16.5$ cm [1] so that the survival probability to a depth d varies as e^{-d/λ_I} . Fluctuations in shower development and decay in flight of hadrons to final states with muons are the main sources of hadron misidentification as muons. The penetration technique has a reduced efficiency for muons with momentum below 1 GeV/ c , due to ranging out of the charged track in the absorber. Moreover, only muons with a sufficiently high transverse momentum can penetrate the IFR to sufficient depth to be efficiently identified.

Neutral hadrons interact in the electromagnetic calorimeter as well as in the flux return. A K_L^0 tends to interact in the inner section of the absorber, therefore K_L^0 identification capability is mainly dependent on energy deposited in the inner part of the absorber, thus a fine segmentation at the beginning of the iron stack is needed. Best performance can be obtained by combining the initial part of a shower in the electromagnetic calorimeter with the rear part in the inner portion of the IFR. An active layer between the two subsystems, external to the solenoid, is therefore desirable.

7.1.2 Baseline Design Requirements

The total amount of material in the *BABAR* detector flux return (about 5 interaction lengths at normal incidence in the barrel region including the inner detectors) is not optimal for muon identification [2]. Adding iron with respect to

the *BABAR* flux return for the upgrade to the Super*B* detector can produce an increase in the pion rejection rate at a given muon identification efficiency, and one of the goals of the simulation studies is to understand whether the *BABAR* iron structure can be upgraded to match the Super*B* muon detector requirements. A possible longitudinal segmentation of the iron is shown in Fig. 30. The three inner detectors are most useful for K_L^0 identification; the coarser segmentation in the following layers preserves the efficiency for low momentum muons.

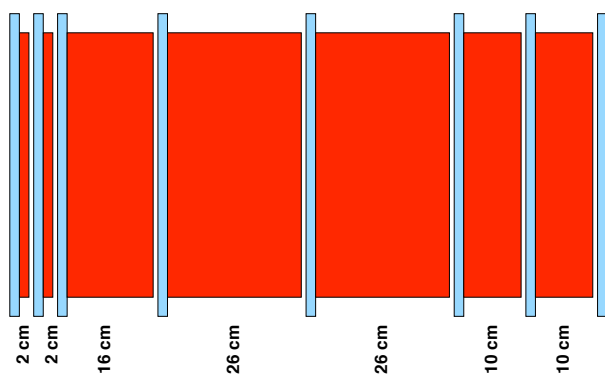


Figure 30: Sketch of the longitudinal segmentation of the iron absorber (red) in the baseline configuration. Active detector positions are shown in light blue from the innermost (left) to the outermost (right) layers.

The layout presented in Fig. 30 has a total of 92 cm of iron and allows the reuse of the *BABAR* flux return with some mechanical modifications. It is our baseline configuration, although several different possible designs are under study. The final steel segmentation will be chosen on the basis of Monte Carlo studies of muon penetration, and charged and neutral hadron interactions. Preliminary results of these studies are shown in the next section.

7.1.3 Design Optimization and Performance Studies

We are performing the detector optimization by means of a Geant4 based simulation in or-

der to have a reliable description of hadronic showers. The simulation also includes realistic features derived from detector R&D studies such as spatial resolution, detection efficiency, and electronic noise. Single muons and pions with momentum ranging between 0.5 GeV/ c and 4 GeV/ c enter the detector and their tracks are reconstructed and analyzed to extract relevant quantities for a cut based muon selector. Preliminary results obtained using the baseline detector configuration give an average muon efficiency of $\sim 87\%$ with a pion contamination of $\sim 2.1\%$ over the entire momentum range. The efficiency and misidentification probability for muons and charged pions as function of the particle momentum are shown in Fig. 31.

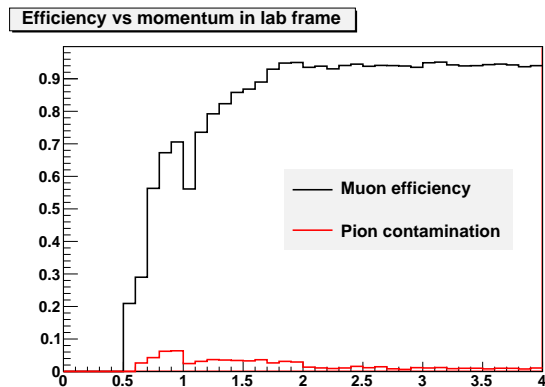


Figure 31: Efficiency and misidentification probability for muons and charged pions as function of the particle momentum. Study performed with baseline detector configuration.

In spite of the good results obtained with the baseline configuration, more extensive studies are needed before making a final decision on the detector design: a careful comparison with other iron configurations will be done using a neural network algorithm for the particle identification. Further simulation studies will also include the effects of machine background on detector performance, and a detailed investigation of neutral hadrons.

7.2 R&D Work

Scintillators. Main requirements for the scintillator are a good light yield and a fast response. Both these requirements depend on the scintillator material characteristics and on the geometry adopted for the bar layout. Since more than 20 metric tons of scintillator will be used in the final detector, minimizing cost is a major concern. We found the extruded scintillator produced by the FNAL-NICADD facility (also used in the MINOS experiment [3]) suitable for our detector.

Since the gaps between two iron absorbers are roughly 25 mm, the bar thickness should not exceed 20 mm. The bar width is 4 cm and the fibers are placed in three holes extruded with the scintillator. We have two possible layouts for the bar:

- 1 cm thick, filling the gap with two separate thin detection layers;
- 2 cm thick, filling the gap with only one thick active layer.

These two scintillator layouts have been used to study different readout options: a Time readout and; a Binary readout. In the Time readout, one coordinate is determined by the scintillator position and the other by the arrival time of the signal digitized by a TDC. In this case both coordinates are measured by the same 2 cm-thick scintillator bar, and there is therefore no ambiguity in case of multiple tracks, but the resolution of one coordinate is limited by the time resolution of the system (about 1 ns). In the Binary readout option, the track is detected by two orthogonal 1 cm-thick scintillator bars. The spatial resolution is driven by the width of the bars (that is 4 cm as for the Time readout), but in case of multiple tracks a combinatorial association of the hits in the two views must be made.

WLS Fibers. The fibers are required to have a good light yield, to ensure a high detection efficiency and a time response consistent with a $\simeq 1$ ns time resolution. WLS fibers from Saint-Gobain (BCF92) and from Kuraray (Y11-300)

have been tested [4]. Both companies produce multicladd fibers with a good attenuation length ($\lambda \simeq 3.5$ m) and trapping efficiency ($\varepsilon \simeq 5\%$), but Kuraray fibers have a higher light yield, while Saint-Gobain fibers have a faster response (with a decay time $\tau = 2.7$ ns, to be compared with Kuraray's $\tau \simeq 9.0$ ns).

Photodetectors. Recently developed devices, called Geiger Mode APDs, suit rather well the needs of converting the light signal in a tight space and high magnetic field environment. These devices have high gain ($\simeq 10^5$), good Detection Efficiency ($\simeq 30\%$), fast response (rise-time ≈ 200 ps), and are very small (few mm) and insensitive to magnetic field. On the other hand they have a rather high dark count rate (≈ 1 MHz/mm² at 1.5 p.e.) and are sensitive to radiation. Both 1×1 mm² SiPM, produced by IRST-FBK, and MPPC, produced by Hamamatsu, have been tested [5]. The comparison between SiPMs and MPPCs showed the former to have a lower detection efficiency, but also a faster response and less critical dependence on temperature and bias voltage. In order to couple the photodetector with up to four 1.0-mm-thick fibers, 2×2 mm² FBK and 3×3 mm² Hamamatsu devices have been tested; the latter was significantly noisier, and the SiPM is therefore currently considered to be the baseline detector.

7.2.1 R&D Tests and Results

R&D Studies were performed using mainly cosmic rays, with the setup placed inside a custom built 4 m long “dark box” to keep scintillators, fibers and photodetectors in a light-tight volume.

Given the sensitivity to radiation, the possibility of placing the SiPMs in a low radiation area outside the detector, bringing the light signal to the photodetectors through about 10 m of clear fibers has been studied. The light loss, expected to be about a factor 3 (confirmed by measurements) due to the attenuation length of

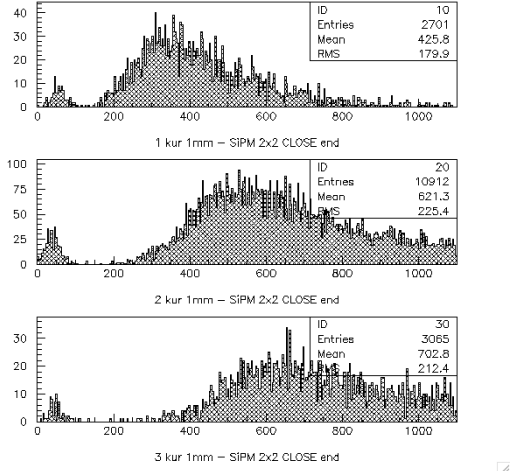


Figure 32: Light collected by 1, 2 and 3 fibers coupled to a SiPM $2 \times 2 \text{ mm}^2$.

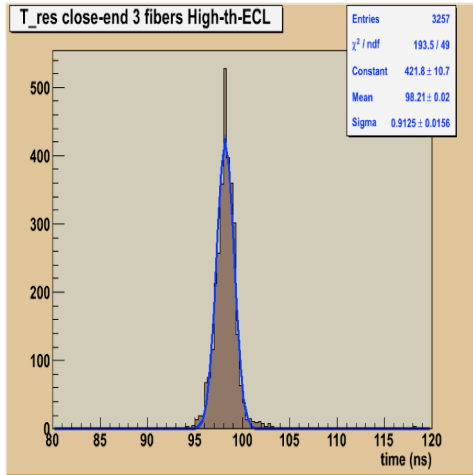


Figure 33: Fit to the time distribution of the SiPM signal.

the clear fiber ($\lambda \approx 10 \text{ m}$), can be partially recovered by using more than one fiber per scintillator bar. Figure 32 shows the comparison of the collected charge in a $2 \times 2 \text{ mm}^2$ SiPM through 1, 2, or 3 WLS fibers. With three fibers in the scintillator we would recover a factor 1.65, while putting a fourth fiber would add only another 10% of light, insufficient to fully regain the light lost in the clear fibers, which is needed to meet the efficiency and the time resolution values dis-

cussed below. Since the light loss is too high to bring the photodetector out of the iron, the SiPMs must be coupled to the WLS fibers inside the detector, at the end of the scintillator bars. Appropriate neutron shields are essential to guarantee a reasonable SiPM lifetime.

A systematic study has been performed with the photodetectors directly coupled to the WLS fibers. The detection efficiency (ε) and the time resolution (σ_T) have been measured in the most critical points. Figure 33 shows a typical time distribution while all the results are reported in Table 4. The goal is to have a detection efficiency $\varepsilon > 95\%$ and, for the Time readout only, a time resolution $\sigma_T \simeq 1 \text{ ns}$ (that would translate to a longitudinal coordinate resolution $\sigma_z \simeq 20 \text{ cm}$). From Table 4 we see that, in order to have some safety margin, the minimum of fibers to be placed inside the scintillator is three.

A radiation test has also been carried out at the Frascati Neutron Generator facility (ENEA laboratory). First results ([7]) show that radiation effects start from an integrated dose of $\simeq 10^8 \text{ n/cm}^2$ and remain rather stable up to a dose of $\simeq 7 \times 10^{10} \text{ n/cm}^2$; in this range, the irradiated SiPMs continue to work, although with lower efficiency and higher dark rate.

7.2.2 Prototype

R&D achievements will be tested on a full scale prototype that is currently in preparation and that will be used to validate the simulation results. The prototype is composed of a full stack of iron with a segmentation which allows the study of different detector configurations. The active area is $60 \times 60 \text{ cm}^2$ for each gap. Scintillator slabs, full length WLS fibers and photodetectors will be located in light-tight boxes (one for each active layer) placed within the gaps. The prototype will be equipped with eight active layers: four having Binary readout and four with Time readout. A beam test will be done at Fermilab using a muon/pion beam with momentum ranging from $1 \text{ GeV}/c$ to $5 \text{ GeV}/c$. Beside the muon identification capability with different iron configurations, which is the main purpose

TIME READOUT						
	Time Resolution (ns)			Detection Efficiency (%)		
2 fibers	1.5 p.e.	2.5 p.e.	3.5 p.e.	1.5p.e.	2.5p.e.	3.5 p.e.
0.3 m	0.91	0.95	–	95.4	98.6	–
2.2 m	1.38	1.44	–	95.9	96.5	–
3 fibers	1.5 p.e.	2.5 p.e.	3.5 p.e.	1.5p.e.	2.5p.e.	3.5 p.e.
0.3 m	0.89	0.91	0.97	94.2	98.9	99.4
2.2 m	1.16	1.17	1.26	95.9	99.1	99.1

BINARY READOUT						
	Time Resolution (ns)			Detection Efficiency (%)		
2 fibers	1.5 p.e.	2.5 p.e.	3.5 p.e.	1.5p.e.	2.5p.e.	3.5 p.e.
2.4 m	1.87	2.16	2.14	98.8	97.4	91.6
3 fibers	1.5 p.e.	2.5 p.e.	3.5 p.e.	1.5p.e.	2.5p.e.	3.5 p.e.
2.4 m	1.60	1.65	1.76	98.7	99.2	98.5

Table 4: Summary of measurements for the Time and Binary readout. The few % lowering of the detection efficiency at 1.5 p.e. threshold is a dead time effect due to the high rate

of the beam test, detection efficiency and spatial resolution of the detector will also be measured.

7.3 Baseline Detector Design

Although the final detector design will be decided after the prototype test, a preliminary baseline layout can be defined from the R&D studies, the simulation results and the experience with the *BABAR* muon detector. Binary and Time readout have pros and cons from the performance point of view, but they both match the requirements for *SuperB*. Mechanically, the installation of the Binary readout, with orthogonal layers of scintillator, would be rather complicated in the barrel due to the limited access to the gaps. On the other hand, the region of the endcaps at low radii is subjected to high radiation and is not a suitable location for the photodetectors. Therefore we currently plan to instrument the barrel region with Time readout, with the photodetectors on both ends of the bars, and to instrument the endcaps with Binary readout, reading the bars only on one end. The number of fibers is three per scintillator bar for each readout mode and the photodetectors are placed inside the gaps just at the end

of the bars. The signal is brought to the electronics card, placed outside the iron, by means of about 10 m of coaxial cable. A detailed description of the frontend electronics will be given in the Electronics section.

7.3.1 Flux Return

The baseline configuration foresees reuse of the *BABAR* flux return with some mechanical modifications. The design thickness of the absorbing material in *BABAR* was 650 mm in the barrel and 600 mm in the endcaps; in order to improve the muon identification the thickness was then increased up to 780 mm in the barrel and up to 840 mm in the forward endcap by replacing some active layers with brass plates and adding a steel plate in the forward part of the endcap. In the *SuperB* baseline design, the total thickness of the absorbing material is 920 mm, corresponding to 5.5 interaction lengths. This can be achieved either by filling more gaps with metal plates (brass or low permeability stainless steel), or by reusing a 100 mm steel thickness in the barrel which was not used in *BABAR*. The last point requires considerable modification of the support structures surrounding the barrel flux return and, due to the increased weight, a

general reinforcement of the support elements is needed.

References

- [1] C. Amsler *et al.* (Particle Data Group), Phys. Lett. B **667**, 1 (2008).
- [2] B. Aubert *et al.* (BABAR Collaboration), *The BABAR Detector*, Nucl. Instrum. Methods Phys. Res., Sect. A **479**, 1 (2002) [arXiv:hep-ex/0105044].
- [3] MINOS Collaboration, *The MINOS Technical Design Report*, NuMI Note, NuMI-L-337.
- [4] Bicron specs @ <http://www.detectors.saint-gobain.com/fibers.aspx>;
- [5] Kuraray specs @ <http://www.df.unife.it/u/baldini/superB/Kuraray.pdf>.
- [6] C. Piemonte *et al.*, *Development of Silicon PhotoMultipliers at FBK-irst*, Nuovo Cimento **C30**, 473 (2007); MPPC specs @ <http://sales.hamamatsu.com/en/products/solid-state-division/si-photodiode-series/mppc.php>.
- [7] M. Andreotti *et al.*, *A Muon Detector based on Extruded Scintillators and GM-APD Readout for a Super B Factory*, Nuclear Science Symposium Conference Record, 2009. NSS '09. IEEE(2009).
- [8] M. Angelone *et al.*, *Silicon Photo-Multiplier radiation hardness tests with a beam controlled neutron source*, arXiv:1002.3480 [physics.ins-det].

8 Electronics, Trigger, DAQ and Online

8.1 Overview of the Architecture

The architecture proposed for the Super B [1] Electronics, Trigger, Data acquisition and Online systems (ETD) has evolved from the $BABAR$ architecture, informed by the experience gained from running $BABAR$ [2] and building the LHC experiments [3], [4], [5]. The detector side of the system is synchronous and all sub-detector readouts are now triggered, leading to improved reliability and uniformity. In Super B , standard links like Ethernet are the default; custom hardware links are only used where necessary. The potential for high radiation levels makes it mandatory to design radiation-safe on-detector electronics.

The first-level hardware trigger uses dedicated data streams of reduced primitives from the sub-detectors and provides decisions to the fast control and timing system (FCTS) which is the centralized bandmaster of the system. The FCTS distributes the clock and the fast commands to all elements of the architecture and controls the readout of the events.

A high level trigger (HLT) processes complete events and reduces the data stream to an acceptable rate for logging.

8.1.1 Trigger Strategy

The $BABAR$ and Belle [6] experiments both chose to use “open triggers” that preserved nearly 100% of $B\bar{B}$ events of all topologies, and a very large fraction of $\tau^+\tau^-$ and $c\bar{c}$ events. This choice enabled very broad physics programs at both experiments, albeit at the cost of a large number of events that needed to be logged and reconstructed, since it was so difficult to reliably separate the desired signals from the $q\bar{q}$ ($q = u, d, s$) continuum and from higher-mass two-photon physics at trigger level. The physics program envisioned for Super B requires very

high efficiencies for a wide variety of $B\bar{B}$, $\tau^+\tau^-$, and $c\bar{c}$ events, and depends on continuing the same strategy, since few classes of the relevant decays provide the kinds of clear signatures that allow the construction of specific triggers.

All levels of the trigger system should be designed to permit the acquisition of prescaled samples of events that can be used to measure the trigger performance.

The trigger system consists of the following components ¹:

Level 1 (L1) Trigger: A synchronous, fully pipelined L1 trigger receives continuous data streams from the detector independently of the event readout and delivers readout decisions with a fixed latency. While we have yet to conduct detailed trigger studies, we expect the L1 trigger to be similar to the $BABAR$ L1 trigger, operating on reduced-data streams from the drift chamber and the calorimeter. We will study the possibilities of improving the L1 trigger performance by including SVT information, taking advantage of larger FPGAs, faster drift chamber sampling, the faster forward calorimeter, and improvements to the trigger readout granularity of the EMC.

High Level Triggers (HLT)—Level 3 (L3) and Level 4 (L4): The L3 trigger is a software filter that runs on a commodity computer farm and bases its decisions on specialized fast reconstruction of complete events. An additional “Level 4” filter may be implemented to reduce the volume of permanently recorded data if needed. Decisions by L4 would be based on a more complete event reconstruction and analysis. Depending on the worst-case performance guarantees of the reconstruction algorithms, it might become necessary to decouple this filter from the near-realtime requirements of L3—hence, its designation as a separate stage.

¹ While at this time we do not foresee a “Level 2” trigger that acts on partial event information in the data path, the data acquisition system architecture would allow the addition of such a trigger stage at a later time, hence the nomenclature.

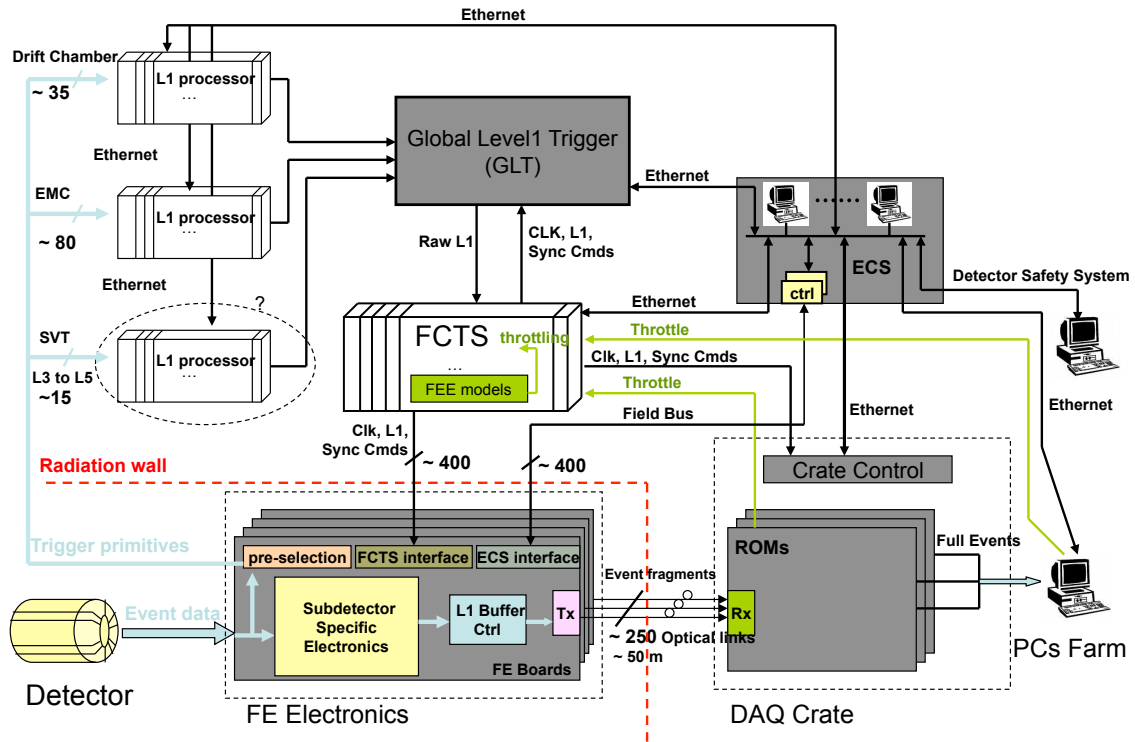


Figure 34: Overview of the ETD and Online global architecture

8.1.2 Trigger Rates and Event Size Estimation

The present L1-accept rate design standard is 150 kHz. It has been increased from the SuperB CDR [1] design of 100 kHz to allow more flexibility and add headroom both to accommodate the possibility of higher backgrounds than design (e.g. during machine commissioning), and the possibility that the machine might exceed its initial design luminosity of $10^{36} \text{ cm}^{-2}\text{sec}^{-1}$.

The event size estimates still have large uncertainties. Raw event sizes (between front-end electronics and ROMs) are understood well enough to determine the number of fibres required. However, neither the algorithms that will be employed in the ROMs for data size reduction (such as zero suppression or feature extraction) nor their specific performance for event size reduction are yet known. Thus, while the 75 kbytes event size extrapolated from BABAR for the CDR remains our best estimate,

the event size could be significantly larger due to new detector components such as Layer 0 of the SVT and/or the forward calorimeter. **In this document we will use 150 kHz L1-accept rate and 75 kbytes per event as the baseline.**

With the prospect of future luminosity upgrades up to 4 times the initial design luminosity, and the associated increases in event size and rate, we also must define the system upgrade path, including which elements need to be designed upfront to facilitate such an upgrade, which can be deferred until a later time, and, ultimately, what the associated costs would be.

8.1.3 Dead Time and Buffer Queue Depth Considerations

The readout system is designed to handle an average rate of 150 kHz and to absorb the expected instantaneous rates, both without incur-

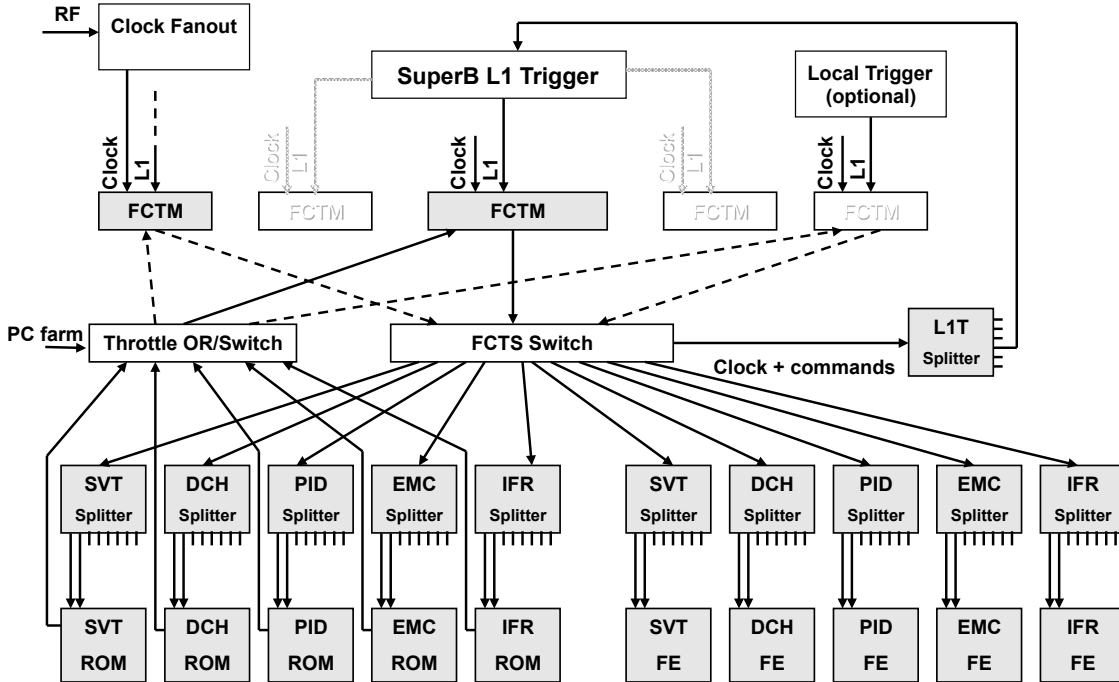


Figure 35: Fast Control and Timing System

ring dead time² of more than 1% under normal operating conditions at design luminosity. The average rate requirement determines the overall system bandwidth: the instantaneous trigger rate requirement affects the FCTS (Fast Control and Timing System), the data extraction capabilities of the front-end-electronics, and the depth of the de-randomization buffers. The minimum time interval between bunch crossings at design luminosity is about 2.1 ns—so short in comparison to detector data collection times that we assume “continuous beams” for the purposes of trigger and FCTS design. Therefore, the burst handling capabilities (minimum time between triggers and maximum burst length) to achieve the dead time goal are dominated by the capability of the L1 trigger to separate events in time and by the ability of the trigger and read-

²Dead time is generated and managed centrally by the FCTS which will drop valid L1 trigger requests that would not fit into the readout system’s envelope for handling of average or instantaneous L1 trigger rates. out systems to handle events that are partially

overlapping in space or time (pile-up, accidentals, etc.). Detailed detector and trigger studies are needed to determine these requirements.

8.2 Electronics, Trigger and DAQ

The Electronics, Trigger and DAQ (ETD) system includes all the hardware elements in the architecture, including FCTS, sub-detector-specific and common parts (CFEE) of the front-end electronics (FEE) for data readout and control, the Level 1 hardware trigger, the Readout Module boards (ROMs), the Experiment Control System (ECS), and the various links that interconnect these components.

The general design approach is to standardize components across the system as much as possible, to use mezzanine boards to isolate sub-system-specific functions differing from the standard design, and to use commercially available common off-the-shelf (COTS) components where viable.

We will now describe the main components of the ETD in more detail.

8.2.1 Fast Control and Timing System

The Fast Control and Timing System (FCTS, Fig. 35) manages all elements linked to clock, trigger, and event readout, and is responsible for partitioning the detector into independent sub-systems for testing and commissioning.

The FCTS will be implemented in a crate where the backplane can be used to distribute all the necessary signals in point-to-point mode. This permits the delivery of very clean synchronous signals to all boards—avoiding the use of external cables. The Fast Control and Timing Module (FCTM, shown in Fig. 36) provides the main functions of the FCTS:

Clock and Synchronization: The FCTS synchronizes the experiment with the machine and its bunch pattern, distributes the clock throughout the experiment, buffers the clock, and generates synchronous reset commands.

Trigger Handling: The FCTS receives the raw L1 trigger decisions, throttles them as necessary, and broadcasts them to the sub-detectors.

Calibration and Commissioning: The FCTS can trigger the generation of calibration pulses

and flexibly programmable local triggers for calibration and commissioning.

Event Handling: The FCTS generates event identifiers, manages the event routing, and distributes event routing information to the ROMs. It also keeps a trace of all of its activity, including an accounting of triggers lost due to dead time or other sources of throttling and event-linked data that needs to be included with the readout data.

The FCTS crate includes as many FCTM boards as required to cover all partitions. One FCTM will be dedicated to the unused sub-systems in order to provide them with the clock and the minimum necessary commands.

Two dedicated switches are required in order to be able to partition the system into independent sub-systems or groups of sub-systems. One switch distributes the clock and commands to the front-end boards, the other collects throttling requests from the readout electronics or the ECS. These switches can be implemented on dedicated boards, connected with the FCTMs, and need to receive the clock. To reduce the number of connections between ROM crates and the global throttle switch board, throttle commands could be combined at the ROM crate level before sending them to the global switch.

Instantaneous throttling of the data acquisition by directly inhibiting the raw L1 trigger from the front-end electronics is not possible because the induced latency is too long. Instead, models of the front-ends and the L1 event buffer queues will be emulated in the FCTM to instantaneously reduce the trigger rate if data volume exceeds the front-end capacity.

The FCTM also manages the distribution of events to the HLT farm for event building, deciding the destination farm node for every event. There are many possible implementations of the event building network protocol and the routing of events based on availability of HLT farm machines, so at this point we can provide only a high-level description. We strongly prefer to use

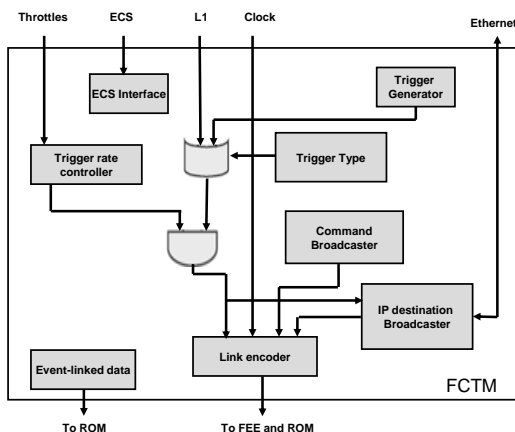


Figure 36: Fast Control and Timing Module

the FCTS to distribute event routing information to the ROMs because it is simple and provides natural synchronization. Management of event destinations and functions such as bandwidth management for the event building network or protocols to manage the event distribution based on the availability of farm servers can then be implemented in FCTM firmware and/or software.

“Continuation events” to deal with pile-up could either be merged in the ROMs or in the high-level trigger farm, but we strongly prefer to merge them in the ROMs. Merging them in the trigger farm would complicate the event builder and require the FCTS to maintain event state and adjust the event routing to send all parts of a continuation event to the same HLT farm node.

8.2.2 Clock, Control and Data Links

Designing and validating the different serial links required for SuperB (for data transmission, timing, and control commands distribution and read-out) will require substantial effort during the TDR phase. Because of fixed latency and low jitter constraints, simple solutions relying on off-the-shelf electronics components must be thoroughly tested to validate them for use in clock and control links. Moreover, because radiation levels on the detector side are expected to be high, R&D will be necessary to qualify the selected chip-sets for radiation robustness. Since requirements for the various link types differ, technical solutions for different link types may also differ.

The links are used to distribute the frequency-divided machine clock (running at 56 MHz) and fast control signals such as trigger pulses, bunch crossing, and event IDs or other qualifiers to all components of the ETD system. Copper wires are used for short haul data transmission (< 1m), while optical fibres are used for medium and long haul. To preserve timing information, suitable commercial components will be chosen so that the latency of transmitted data and

the phase of the clock recovered from the serial stream do not change with power cycles, resets, and loss-of-locks. Encoding and/or scrambling techniques will be used to minimize the jitter on the recovered clock. The same link architecture is also suitable for transmitting regular data instead of fast controls, or a combination of both.

Link types can be divided into two classes:

A-Type: The A-type links are homogeneous links with both ends off-detector. Given the absence of radiation, they might be implemented with Serializer-De-serializers (SerDes) embedded in FPGAs (Field Programmable Gate Arrays). Logic in the FPGA fabric will be used to implement fixed latency links and to encode/decode fast control signals. A-Type links are used to connect the FCTS system to the DAQ crate control and to the Global Level 1 Trigger. A-Type links run at approximately 2.2 Gbits/s.

B-Type: The B-type hybrid links have one end on-detector and the other end off-detector. The on-detector side might be implemented with off-the-shelf radiation-tolerant components—the off-detector end might still be implemented with FPGA-embedded SerDes. B-Type links connect the FCTS crate to the FEE and the FEE to ROMs. The B-Type link speed might be limited by the off-the-shelf SerDes performance, but is expected to be at least 1 Gbit/s for the FCTS to FEE link and about 2 Gbits/s for the FEE to ROM link.

All links can be implemented as plug-in boards or mezzanines, (1) decoupling the development of the user logic from the high-speed link design, (2) simplifying the user board layout, and (3) allowing an easy link upgrade without affecting the host boards. Mezzanine specifications and form-factors will likely be different for A-Type and B-Type links, but they will be designed to share a common interface to the host board to the maximum possible extent.

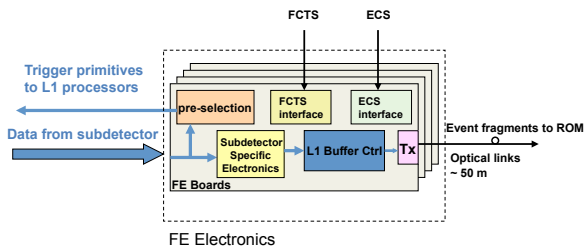


Figure 37: Common Front-End Electronics

8.2.3 Common Front-End Electronics

Common Front-End Electronics (CFEE) designs and components allow us to exploit the commonalities between the sub-detector electronics and avoid separate design and implementation of common functions for each sub-detector.

In our opinion, the separate functions required to drive the FEE should be implemented in dedicated independent elements. These elements will be mezzanines or circuits directly mounted on the front-end modules (which act as carrier boards) and will be standardized across the sub-systems as much as possible. For instance, as shown in Fig. 37, one mezzanine can be used for FCTS signal and command decoding, and one for ECS management. To reduce the number of links, it may be possible to decode the FCTS and ECS signals on one mezzanine and then distribute them to the neighbouring boards.

A common dedicated control circuitry inside a radiation-tolerant FPGA may also drive the L1 buffers. It would handle the L1 accept commands and provide the signals necessary to manage the data transfers between latency buffers, derandomizer buffers and the fast multiplexers feeding the optical link serializers. If required by the system design, it would also provide logic for special treatment of pile-up events and/or extending the readout window back in time after a Bhabha event has been rejected.

The latency buffers can be implemented either in the same FPGA or directly on the carrier boards. One such circuit can drive numerous data links in parallel, thus reducing the amount of electronics on the front-end.

One intriguing, possible advantage of this approach is that *analog* L1 buffers might be implemented in an ASIC, though the analog output of the ASIC then must be able to drive an internal or external ADC that samples the signal.

Serializers and optical link drivers will also reside on carrier boards, mainly for mechanical and thermal reasons. Fig. 37 shows a possible implementation of the L1 buffers, their control electronics (in a dedicated FPGA), and their outputs to the optical readout links.

All (rad-tolerant) FPGAs in the FEE have to be reprogrammable without dismounting a board. This could be done through dedicated front panel connectors, which might be linked to numerous FPGAs, but it would be preferable if the reprogramming could be done through the ECS without any manual intervention on the detector side.

Sampling of the analog signals in the FEEs is done with the global clock or a clock signal derived from the global clock (typically by dividing it down). To maintain the timing required by the fixed latency design, the latency buffers in the FEEs must be read with the same sampling frequency as they are written. In addition, when initializing the FEE boards, care must be taken that all dividers are reset synchronously with those of the first level trigger (by a global signal) in order to maintain a constant phase between them.

8.2.4 Readout Module

The Readout Modules (ROM, Fig. 38) receive event fragments from the sub-detectors' front-end electronics, tag them with front-end identifiers and absolute time-stamps, buffer them in de-randomizing memories, perform processing (still to be defined) on the fragment data, and eventually inject the formatted fragment buffers into the event builder and HLT farm. Connected to the front-end electronics via optical fibres, they will be located in an easily accessible, low radiation area.

A modular approach will maximize standardization across the system to simplify develop-

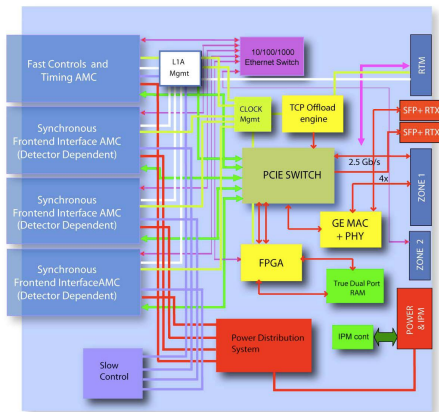


Figure 38: Readout Module

ment and keep costs low—different sub-detector requirements can then be accommodated by using sub-detector-specific “personality modules”.

On the ROM boards, signals from optical receivers mounted on mezzanine cards will be routed to the de-serializers (in commercial FPGAs) where data processing can take place. Special requirements from the sub-detector systems will be accommodated by custom-built mezzanines mounted on common carriers. One of the mezzanine sites on the carrier will host an interface to the FCTS to receive global timing and trigger information. The carrier itself will host memory buffers and 1 Gbit/s or 10 Gbits/s links to the event building network.

A baseline of 8 optical fibres per card currently seems like a good compromise between keeping the number of ROM boards low and adding to their complexity. This density is sufficient so that there needs to be only one ROM crate per sub-detector, and corresponds nicely to the envisaged FCTS partitioning.

8.2.5 Experiment Control System

The complete SuperB experiment (power supplies, front-end, DAQ, etc.) must be controlled by an Experiment Control System (ECS). As shown in Fig. 34, the ECS is responsible both for controlling the experiment and for monitoring its functioning.

Configuring the Front-ends: Many front-end parameters must be initialized before the system can work correctly. The number of parameters per channel can range from a only a few to large per-channel lookup tables. The ECS may also need to read back parameters from registers in the front-end hardware to check the status or verify that the contents have not changed. For a fast detector configuration and recovery turnaround in factory mode, it is critical to not have bottlenecks either in the ECS itself, or in the ECS’ access to the front-end hardware. If technically feasible and affordable, front-end electronics on or near the detector should be shielded or engineered to avoid frequent parameter reloads due to radiation-induced single event upsets—reconfiguring through the ECS should only be considered as a last resort.

Calibration: Calibration runs require extended functionality of the ECS. In a typical calibration run, after loading calibration parameters, event data collected with these parameters must be sent through the DAQ system and analyzed. Then the ECS must load the parameters for the next calibration cycle into the front-ends and repeat.

Testing the FEE: The ECS may also be used to remotely test all FEE electronics modules using dedicated software. This obviates the need for independent self-test capability for all modules.

Monitoring the Experiment: The ECS continuously monitors the entire experiment to insure that it functions properly. Some examples include (1) independent spying on event data to verify data quality, (2) monitoring the power supplies (voltage, current limits, etc.), and (3) monitoring the temperature of power supplies, crates, and modules. Support for monitoring the FEE modules themselves must be built into the FEE hardware so that the ECS can be informed about FEE failures. The ECS also acts

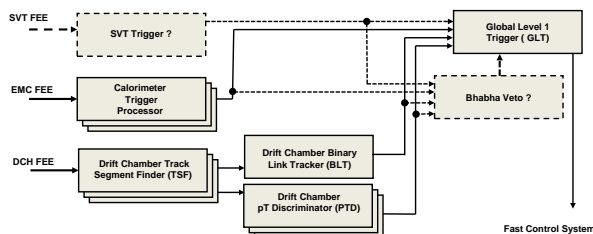


Figure 39: Level 1 Trigger Overview

as a first line of defense in protecting the experiment from a variety of hazards. In addition, an independent, hardware-based detector safety system (part of the Detector Control System, see 8.3.6) must protect the experiment against equipment damage in case the software-based ECS is not operating correctly.

The specific requirements that each of the sub-systems makes on ECS bandwidth and functionality must be determined (or at least estimated) as early as possible so that the ECS can be designed to incorporate them. Development of calibration, test, and monitoring routines must be considered an integral part of sub-system development, as it requires detailed knowledge about sub-system internals.

Possible ECS Implementation: The field bus used for the ECS has to be radiation tolerant on the detector side and provide very high reliability. Such a bus has been designed for the LHCb experiment: it is called SPECS (Serial Protocol for Experiment Control System) [7]. It is a bidirectional 10 Mbits/s bus that runs over standard Ethernet Cat5+ cable and provides all possible facilities for ECS (like JTAG (Joint Test Action Group) and I2C (Inter IC)) on a small mezzanine. It could be easily adapted to the SuperB requirements. Though SPECS was initially based on PCI boards, it is currently being translated to an Ethernet-based system, as part of an LHCb upgrade, also integrating all the functionalities for the out-of-detector elements.

For the electronics located far from the detector, Ethernet will be used for ECS communication.

8.2.6 Level 1 Hardware Trigger

The current baseline for the L1 trigger is to reimplement the *BABAR* L1 trigger with state-of-the-art technology. It would be a synchronous machine running at 56 MHz (or multiples of 56 MHz) that processes primitives produced by dedicated electronics located on the front-end boards or other dedicated boards of the respective sub-detector. The raw L1 decisions are sent to the FCTM boards which applies a throttle if necessary and then broadcasts them to the whole experiment. The standard chosen for the crates would most likely be either ATCA (Advanced Telecommunications Computing Architecture) for the crates and the backplanes, or a fully custom architecture.

The main elements of the L1 trigger are shown in Fig. 39 (see [8] for detailed descriptions of the *BABAR* trigger components):

Drift chamber trigger (DCT): The DCT consists of a track segment finder (TSF), a binary link tracker (BLT) and a p_t discriminator (PTD).

Electromagnetic Calorimeter Trigger (EMT): The EMT processes the trigger output from the calorimeter to find clusters.

Global Trigger (GLT): The GLT processor combines the information from DCT and EMT (and possibly other inputs such as an SVT trigger or a Bhabha veto) and forms a final trigger decision that is sent to the FCTS.

We will study the applicability of this baseline design at SuperB luminosities and backgrounds, and will investigate improvements, such as adding a Bhabha veto or using SVT information in the L1 trigger. We will also study faster sampling of the DCH and the new fast forward calorimeter. In particular for the barrel EMC we will need to study how the L1 trigger time resolution can be improved and the trigger jitter can be reduced compared to BaBar. In

general, improving the trigger event time precision should allow a reduction in readout window and raw event size. The L1 trigger may also be improved using larger FPGAs (e.g. by implementing tracking or clustering algorithm improvements, or by exploiting better readout granularity in the EMC).

L1 Trigger Latency: The *BABAR* L1 trigger had $12\ \mu\text{s}$ latency. However, since the size, and cost, of the L1 data buffers in the sub-detectors scale directly with trigger latency, it should be substantially reduced, if possible. L1 trigger latencies of the much larger, more complex, ATLAS, CMS and LHCb experiments range between 2 and $4\ \mu\text{s}$, however these experiments only use fast detectors for triggering. Taking into consideration that the DCH adds an intrinsic dead time of about $1\ \mu\text{s}$ and adding some latency reserve for future upgrades, we are currently estimating a total trigger latency of $6\ \mu\text{s}$ (or less). More detailed engineering studies will be required to validate this estimate.

Monitoring the Trigger: To debug and monitor the trigger, and to provide cluster and track seed information to the higher trigger levels, trigger information supporting the trigger decisions is read out on a per-event basis through the regular readout system. In this respect, the low-level trigger acts like just another sub-detector.

8.3 Online System

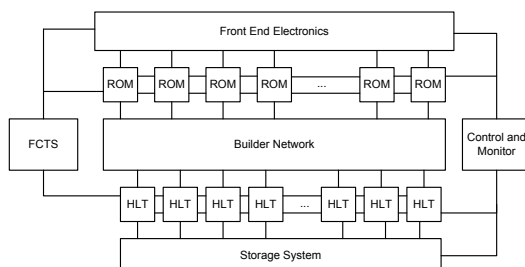


Figure 40: High-level logical view of the Online System

The Online system is responsible for reading out the ROMs, building complete events, filtering events according to their content (High Level Triggers), and archiving the accepted events for further physics analysis (Data Logging). It is also responsible for continuous monitoring of the acquired data to understand detector performance and detect detector problems (Data Quality Monitoring). The Detector Control System (DCS) monitors and controls the detector and its environment.

Assuming a L1 trigger rate of 150 kHz and an event size of 75 kbytes, the input bandwidth of the Online system must be about 12 Gbytes/s, corresponding to about 120 Gbits/s with overhead. It seems prudent to retain an additional safety factor of ~ 2 , given the event size uncertainty and the immaturity of the overall system design. Thus, we will take 250 Gbits/s as the baseline for the Online system input bandwidth.

Assuming that the HLT accepts a cross-section of about 25 nb leads to an expected event rate of 25 kHz at a luminosity of $10^{36}\ \text{cm}^{-2}\text{sec}^{-1}$, or a logging data rate of $\sim 1.9\ \text{Gbytes/s}$.

The main elements of the Online system (Fig. 40) are described in the following sections.

8.3.1 ROM Readout and Event Building

The ROMs read out event fragments in parallel from sub-detector front-end electronics—buffering the fragments in deep de-randomizing memories. The event-related information is then transferred into the ROM memories, and sent over a network to an event buffer in one of the machines of the HLT farm. This collection task, called event building, can be performed in parallel for multiple events, thanks to the depth of the ROM memories and bandwidth of the event building network switch (preferably non-blocking). Because of this inherent parallelism, the building rate can be scaled up as needed (up to the bandwidth limit of the event building network). We expect to use Ethernet as the basic technology of the event builder network, using 1 Gbits/s and 10 Gbits/s links.

8.3.2 High Level Trigger Farm

The HLT farm needs to provide sufficient aggregate network bandwidth and CPU resources to handle the full Level 1 trigger rate on its input side. The Level 3 trigger algorithms should operate and log data entirely free of event time ordering constraints and be able to take full advantage of modern multi-core CPUs. Extrapolating from *BABAR*, we expect 10 ms core time per event to be more than adequate to implement a software L3 filter, using specialized fast reconstruction algorithms. With such a filter, an output cross-section of 25 nb should be achievable.

To further reduce the amount of permanently stored data, an additional filter stage (L4) could be added that acts only on events accepted by the L3 filter. This L4 stage could be an equivalent (or extension) of the *BABAR* offline physics filter—rejecting events based either on partial or full event reconstruction. If the worst-case behavior of the L4 reconstruction code can be well controlled, it could be run in near real-time as part of, or directly after, the L3 stage. Otherwise, it may be necessary to use deep buffering to decouple the L4 filter from the near real-time performance requirements imposed at the L3 stage. The discussion in the *SuperB* CDR [1] about risks and benefits of a L4 filter still applies.

8.3.3 Data Logging

The output of the HLT is logged to disk storage. We assume at least a few Tbytes of usable space per farm node, implemented either as directly attached low-cost disks in a redundant (RAID) configuration, or as a storage system connected through a network or SAN. We do not expect to aggregate data from multiple farm nodes into larger files. Instead, the individual files from the farm nodes will be maintained in the downstream system and the book-keeping system and data handling procedures will have to deal with missing run contribution files. A switched Gigabit Ethernet network sep-

arate from the event builder network is used to transfer data asynchronously to archival storage and/or near-online farms for further processing. It is not yet decided where such facilities will be located, but network connectivity with adequate bandwidth and reliability will need to be provided. Enough local storage must be available to the HLT farm to allow data buffering for the expected periods of link down-time.

While the format for the raw data has yet to be determined, many of the basic requirements are clear, such as efficient sequential writing, compact representation of the data, portability, long-term accessibility, and the freedom to tune file sizes to optimize storage system performance.

8.3.4 Event Data Quality Monitoring and Display

Event data quality monitoring is based on quantities calculated by the L3 (and possibly L4) trigger, as well as quantities calculated by a more detailed analysis on a subset of the data. A distributed histogramming system collects the monitoring output histograms from all sources and makes them available to automatic monitoring processes and operator GUIs.

8.3.5 Run Control System

The control and monitor of the experiment is performed by the Run Control System (RCS), providing a single point of entry to operate and monitor the entire experiment. It is a collection of software and hardware modules that handle the two main functions of this component: controlling, configuring, and monitoring the whole Online system, and providing its user interface. The RCS interacts both with the Experiment Control System (ECS) and with the Detector Control System (DCS). We expect the RCS to utilize modern web technologies.

8.3.6 Detector Control System

The Detector Control System (DCS) is responsible for ensuring detector safety, controlling the

detector and detector support system, and monitoring and recording detector and environmental conditions.

Efficient detector operations in factory mode require high levels of automation and automatic recovery from problems. The DCS plays a key role in maintaining high operational efficiency, and tight integration with the Run Control System is highly desirable.

Low-level components and interlocks responsible for detector safety (Detector Safety System, DSS) will typically be implemented as simple circuits or with programmable logic controllers (PLCs).

The software component will be built on top of a toolkit that provides the interface to whatever industrial buses, sensors, and actuators may be used. It must provide a graphical user interface for the operator, have facilities to generate alerts automatically, and have an archiving system to record the relevant detector information. It must also provide software interfaces for programmatic control of the detector.

We expect to be able to use existing commercial products and controls frameworks developed by the CERN LHC experiments.

8.3.7 Other Components

Electronic Logbook: A web-based logbook, integrated with all major Online components, allows operators to keep an ongoing log of the experiment's status, activities and changes.

Databases: Online databases such as configuration, conditions, and ambient databases are needed to track, respectively, the intended detector configuration, calibrations, and actual state and time-series information from the DCS.

Configuration Management: The configuration management system defines all hardware and software configuration parameters, and records them in a configuration database.

Performance Monitoring: The performance monitoring system monitors all components of the Online.

Software Release Management: Strict software release management is required, as is a tracking system that records the software version (including any patches) that was running at a given time in any part of the ETD/Online system. Release management must cover FPGAs and other firmware as well as software.

Computing Infrastructure Reliability: The Online computing infrastructure (including the specialized and general-purpose networks, file, database and application servers, operator consoles, and other workstations) must be designed to provide high availability, while being self-contained (sufficiently isolated and provided with firewalls) to minimize external dependencies and downtime.

8.3.8 Software Infrastructure

The Online system is basically a distributed system built with commodity hardware components. Substantial manpower will be needed to design the software components—taking a homogeneous approach in both the design and implementation phases. An Online software infrastructure framework will help organize this major undertaking. It should provide basic memory management, communication services, and the executive processes to execute the Online applications. Specific Online applications will make use of these general services to simplify the performance of their functions. Middleware designed specifically for data acquisition exists, and may provide a simple, consistent, and integrated distributed programming environment.

8.4 Front-End Electronics

8.4.1 SVT Electronics

The SVT electronics shown in Fig. 41 is designed to take advantage, where possible, of the data-push characteristics of the front-end chips. The time resolution of the detector is dominated by the minimal time resolution of the FSSR2 chip, which is 132 ns. Events are

built from packets of three minimal time slices (396 ns event time window). The readout chain in layer 0 starts from a half-module holding two sets of pixel chips (2 readout sections, ROS). Data are transferred on copper wires to boards located a few meters away from the interaction region where local buffers will store the read hits. As discussed in the SVT chapter, for layer 0, the data rate is dominated by the background. The bandwidth needed is about 16 Gbits/s/ROS. This large bandwidth is the main reason to store hits close to the detector and transfer only hits from triggered events.

For events accepted by the L1 trigger, the bandwidth requirement is only 0.85 Gbits/s and data from each ROS can be transferred on optical links (1 Gbit/s) to the front-end boards (FEB) and then to ROMs through the standard 2 Gbits/s optical readout links. Layers 1-5 are read out continuously with the hits being sent to the front-end boards on 1 Gbit/s optical links. On the FEBs, hits are sorted in time and formatted to reduce event size (timestamp stripping). Hits of triggered events are then selected and forwarded to the ROMs on 2 Gbits/s standard links.

Occupancies and rates on layers 3-5 should be low enough to make them suitable for fast track searching so that SVT information could be used in the L1 trigger. The SVT could provide the number of tracks found, the number of tracks not originating from the interaction re-

in the ϕ coordinate. A possible option for SVT participation to the L1 trigger would require two L1 trigger processing boards each one linked to the FEBs of layers 3-5 with synchronous optical links.

In total, the SVT electronics requires 58 FEBs and 58 ROMs, 58 optical links at 2 Gbits/s, 308 links at 1 Gbit/s (radiation hard) and, optionally, two L1 trigger processing boards and about 40 links at 1.25 Gbits/s for L1 trigger processing.

8.4.2 DCH Electronics:

The design is still in a very early stage, so we only provide a baseline description of the drift chamber front-end electronics. It does not include additional front-end features currently under study (such as a cluster counting capability).

The DCH provides charged particle tracking, dE/dx , and trigger information. The front-end electronics measures the drift time of the first electron and the total charge collected on the sense wires, and generates the information to be sent to the L1 trigger.

The DCH front-end chain can be divided into three different blocks:

Very Front End Boards (VFEB): The VFEBs contain HV distribution and blocking capacitors, protection networks and preamplifiers. They could also host discriminators. The VFEBs are located on the (backward) chamber end-plate to maximize the S/N ratio.

Data Conversion and Trigger Pattern Extrac-

tion: Data conversion incorporates both TDCs (1 ns resolution, 10 bits dynamic range) and continuous sampling ADCs (6 bits dynamic range). Trigger data contain the status of the discriminated channels, sampled at about 7 MHz (compared to 3.7 MHz in *BABAR*). This section of the chain can be located either on the end-plate (where power dissipation, radiation environment, and material budget are issues) or in external crates (where either micro-

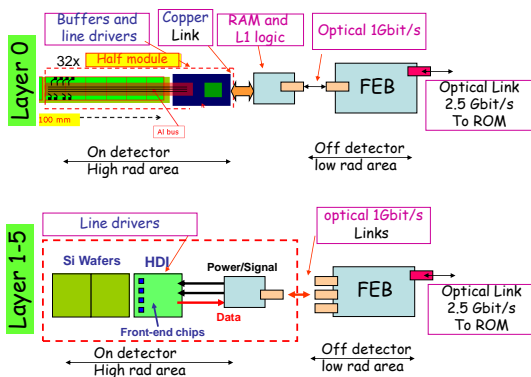


Figure 41: SVT Electronics
gion, and the presence of back-to-back events

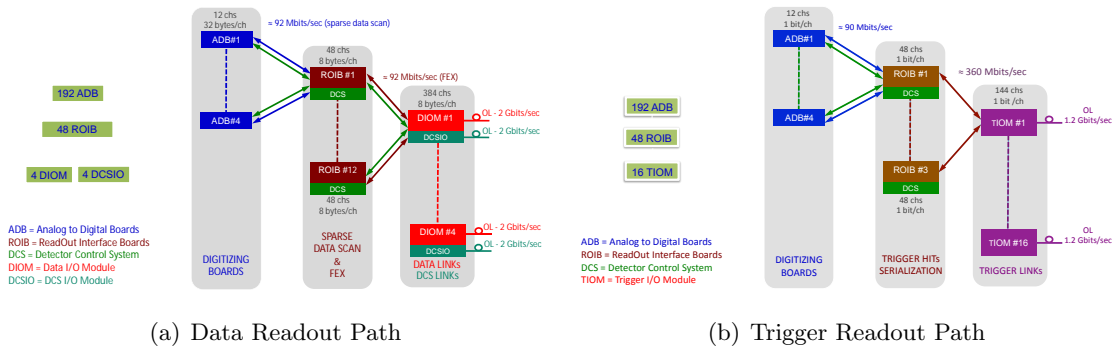


Figure 42: DCH Electronics

coax or twisted cables must be used to carry out the preamplifier signals).

Readout Modules: The ROMs collect the data from the DCH FEE and send zero-suppressed data to DAQ and trigger.

The number of links required for data transfer to the DAQ system can be estimated based on the following assumptions: 150 kHz L1 trigger rate, 10k channels, 15% chamber occupancy in a $1 \mu\text{s}$ time window, and 32 bytes per channel. At a data transfer speed of 2 Gbits/s per link, about 40 links are needed. 56 synchronous 1.25 Gbits/s links are required to transmit the trigger data sampled at 7 MHz. The topology of the electronics suggests that the number of ECS and FCTS links should be the same as the number of readout links.

8.4.3 PID Electronics:

Forward PID Option: There are currently two detector options be considered for the forward PID.

The first option is to measure the time of flight (TOF) of particles from the interaction point to the PID detector. Two implementations are under consideration—a pixel detector which would lead to a large number of read-out channels (7200), or a DIRC-like detector with fused silica bars (plates) which would require a much smaller (192) channel count. Both im-

plementations make use of fast Micro Channel Plate PMTs (MCP-PMT) and have to provide a measurement of the hit time with a precision of ~ 10 ps. The readout would probably use fast analog memories which, as of today, are the most plausible solution for a picosecond time measurement in this environment. To achieve this time resolution, the clock distribution will have to be very carefully designed and will likely require direct use of the machine clock at the beam crossing frequency.

A second option is a Focusing Aerogel Cherenkov detector. Though the timing requirements are less severe, its $\sim 115,000$ channels would also have to come from MCP-PMTs, since standard multi-anode PMTs cannot be used in the high magnetic field where it resides. Since

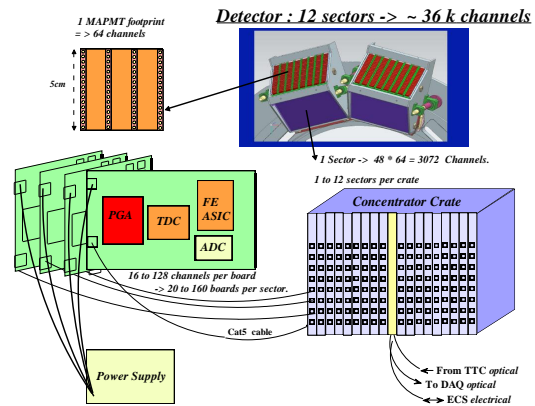


Figure 43: PID Electronics

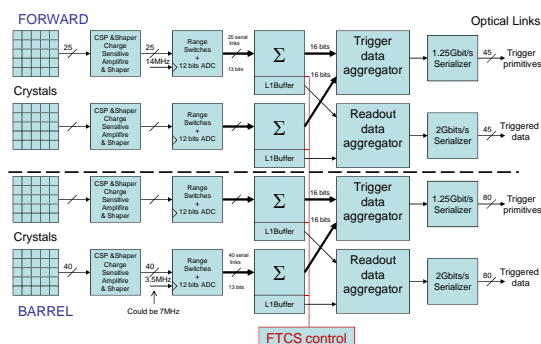


Figure 44: EMC Electronics

the time precision needed is similar to that of the barrel, the same type of electronics could be used. At least 50 links would be the minimum necessary for the data readout, while the ECS and FCTS would require a maximum of about 50 additional links.

Barrel PID: The barrel PID electronics must provide the measurement of the arrival time of the photons produced in the fused silica bars with a precision of about 100 ps rms. The SuperB detector baseline is a focusing DIRC, using multi-anodes photo multipliers. This optical design (smaller camera volume, and materials) reduces the background sensitivity by at least one order of magnitude compared to *BABAR* thus reducing the rate requirements for the front-end electronics.

The baseline design is implemented with 16-channel TDC ASICs—offering the required precision of 100 ps rms. A 12-bit ADC can provide an amplitude measurement, at least for calibration, monitoring and survey, which is transmitted with the hit time. A 16-channel front-end analog ASIC must be designed to sample and discriminate the analog signal. Both ASICs would be connected to a radiation-tolerant FPGA which would handle the hit readout sequence and push data into the L1 trigger latency buffers.

This front-end electronics must all sit on the MAPMT base, where space is very limited and cooling is difficult. However, crates concentrating front-end data and driving the fast opti-

cal links can be located outside the detector in a more convenient place where space is available. They would be connected to the front-end through standard commercial cables (like Cat 5 Ethernet cables). The readout mezzanines would be implemented there, as well as the FCTS and ECS mezzanines from where signals would be forwarded to the front-end electronics through the same cables.

The system would be naturally divided into 12 sectors. Using the baseline camera with 36,864 channels, 150 kHz trigger rate, 100kHz/channel hit rate, 32 data bits/hit, and 2 Gbits/s link rate, the readout link occupancy should be only $\sim 15\%$, thus offering a pleasant safety margin. A camera using another model of PMTs with one-half the number of channels is also being studied.

An alternative readout option would be to use analog memories instead of TDCs to perform both time and amplitude measurements. This option retains more information on the hit signals but would likely be more expensive. Its advantages and disadvantages are still under study.

8.4.4 EMC Electronics:

Two options have been considered for the EMC system design—a *BABAR*-like push architecture where all calorimeter data are sent over synchronous optical 1 Gbit/s links to L1 latency buffers residing in the trigger system, or a “triggered” pull architecture where the trigger system receives only sums of crystals (via synchronous 1 Gbit/s links), and only events accepted by the trigger are sent to the ROMs through standard 2 Gbits/s optical links.

The triggered option, shown in Fig. 44, requires a much smaller number of links and has been chosen as the baseline implementation. The reasons for this choice and the implications are discussed in more detail below.

To support the activated liquid-source calibration, where no central trigger can be provided, both the barrel and the end-cap readout systems need to support a free running “self-triggered” mode where only samples with an ac-

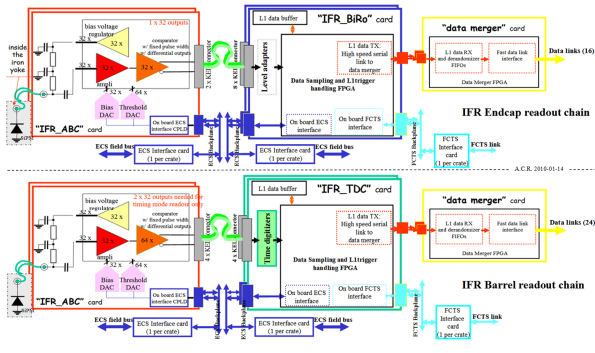


Figure 45: IFR Electronics

tual pulse are sent to the ROM. Pulse detection may require digital signal processing to suppress noisy channels.

Forward Calorimeter The 4500 crystals are read out with PIN or APD photodiodes. A charge preamplifier translates the charge into voltage and the shaper uses a 100 ns shaping time to provide a pulse with a FWHM of 240 ns.

The shaped signal is amplified with two gains ($\times 1$ and $\times 64$). At the end of the analog chain, an auto-range circuit decides which gain will be digitized by a 12 bit pipeline ADC running at 14 MHz. The 12 bits of the ADC plus one bit for the range thus cover the full scale from 10 MeV to 10 GeV with a resolution better than 1%. A gain is set during calibration using a programmable gain amplifier in order to optimize the scale used during calibration with a neutron-activated liquid-source system providing gamma photons around 6 MeV.

Following the *BABAR* detector design, a push architecture with a full granularity readout scheme was first explored. In this approach, the information from 4 channels is grouped, using copper serial links, reaching an aggregate rate of 0.832 Gbits/s per link to use up most of the synchronous optical link's 1 Gbit/s bandwidth. A total of 1125 links are required. The main advantage of this architecture is the flexibility of the trigger algorithm that can be implemented off-detector using state of the art FPGAs with-

out constraining their radiation resistance. The main drawback is the large cost due to the huge number of links.

The number of links can be reduced by summing channels together on the detector side, and only sending the sums to the trigger. The natural granularity of the forward detector is a module which is composed of 25 crystals. In this case, data coming from 25 crystals is summed together, forming a word of 16 bits. Then the sums coming from 4 modules are aggregated together to produce a payload of 0.896 Gbits/s. In this case, the number of synchronous links toward the trigger is only 45. The same number of links would be sufficient to send the full detector data with a 500 ns trigger window. This architecture limits the trigger granularity, and implies more complex electronics on the detector side, but reduces the number of links by a large factor (from 1125 down to 90). However, it cannot be excluded that a faster chipset will appear on the market which could significantly reduce this implied benefit.

Barrel Calorimeter The EMC barrel reuses the 5760 crystals and PIN diodes from *BABAR*, with, however, the shaping time reduced from 1 μ s to 500 ns and the sampling rate doubled from 3.5 MHz to 7 MHz. The same considerations about serial links discussed above for the forward EMC apply to the barrel EMC. If full granularity data were pushed synchronously to the trigger, about 520 optical links would be necessary.

The number of synchronous trigger links can be drastically reduced by performing sums of 4×3 cells on the detector side, so that 6 such energy sums could be continuously transmitted through a single optical serial link. This permits a reduction in the number of trigger links so as to match the topology of the calorimeter electronics boxes, which are split into 40ϕ sectors on both sides of the detector. Therefore, the total number of links would be 80 both for the trigger and the data readout toward the ROMs, including a substantial safety margin (> 1.5).

8.4.5 IFR Electronics:

The IFR is equipped with plastic scintillators coupled to wavelength shifting fibres. Although different options have been explored, it is currently assumed that single photon counting devices (SiPM) will be located “inside” the iron, as close as possible to the scintillating assemblies. Each SiPM will be biased and read out through a single coaxial cable.

A schematic diagram of the IFR readout electronics is shown in Fig. 45. The first stage of the readout chain is based on the IFR_ABC boards which provide (for 32 channels each):

- Amplification, presently based upon off-the-shelf components (COTS).
- Individually programmable bias voltages for the SiPMs.
- Comparators with individually programmable thresholds, presently based on COTS.

To minimize the length of the coaxial cables from the SiPMs to the IFR_ABC boards, these boards need to be placed as close to the iron yoke as possible. The digital outputs of the IFR_ABC boards will then be processed in different ways for the IFR barrel and end-caps.

IFR Barrel The barrel scintillation elements are mounted parallel to the beam axis. The time of arrival of pulses from both ends of the scintillating elements must be recorded so that the z-position of particle hits can be determined during reconstruction. The signals are read out with IFR_TDC 64-channel timing digitizer boards.

The total TDC channel count estimate for the barrel is 14,400, which comes from the 3600 scintillating assemblies in the barrel that are read out at both ends with 2 comparators (with different thresholds) per end to improve timing (and position) resolution.

IFR End-caps: The signals from the scintillators in the IFR end-caps (which are positioned vertically and horizontally) are read out

with IFR_BiRO 128 channel “Binary Readout” boards, which sample the status of the input lines and update a circular memory buffer from which data are extracted upon trigger request.

The total channel count estimate for the end-caps is 9,600 BiRO channels coming from the two end caps, each with 2,400 scintillating assemblies in X, and 2,400 scintillating assemblies in Y read out into a single comparator per channel.

The IFR_TDC and IFR_BiRO digitizers should be located as closely as possible to the IFR_ABC boards to minimize the cost of the interconnecting cables, preferably in an area of low radiation flux. In this case, commercial TDC ASICs could be used in the design. Alternatively, radiation-tolerant TDCs could be used closer to the detector. The FPGAs used in the digitizers should be protected against radiation effects by architecture and by firmware design.

The output streams from the IFR_TDC and IFR_BiRO boards go through custom “data concentrators” to merge the data coming from a number of digitizers, and send the resulting output data to the ROMs via the standard optical readout links.

In total, 225 IFR_TDC boards (12 crates) and 75 IFR_BiRO boards (4 crates) are needed. The total number of links to the ROMs is presently estimated to be 24 for the barrel (2 links per digitizer crate), and 16 for the end-caps (4 links per digitizer crate).

To optimize the electronics topology, the number of ECS and FCTS links should match the number of readout links.

8.5 R&D

For the overall EDT/Online system, substantial R&D is needed to better understand the global system requirements, develop solutions, and probe the possible upgrade paths to handle luminosities of up to $4 \times 10^{36} \text{ cm}^{-2}\text{sec}^{-1}$ during the lifetime of the experiment.

Data Links: The data links for Super*B* require R&D in the following areas: (1) studying jitter related issues and filtering by means of jitter cleaners; (2) coding patterns for effective error detection and correction; (3) radiation qualification of link components; and (4) performance studies of the serializers/de-serializers embedded in the new generation of FPGAs (Virtex6, Xilinx, etc.)

Readout Module: Readout Module R&D includes investigation of 10 Gbits/s Ethernet technology, and detailed studies of the I/O subsystem on the ROM boards. The possibility of implementing the ROM functions in COTS computers by developing suitable PCIe boards (such as optical link boards for FCTS and FEE links, or personality cards to implement sub-detector-specific functions) should also be investigated.

Trigger: For the L1 trigger, the achievable minimum latency and physics performance will need to be studied. The studies will need to address many factors including (1) improved time resolution and trigger-level granularity of the EMC and a faster DCH than *BABAR*; (2) potential inclusion of SVT information at L1; (3) the possibility of a L1 Bhabha veto; (4) possibilities for handling pile-up and overlapping (spatially and temporally) events at L1; and (5) opportunities created by modern FPGAs to improve the trigger algorithms.

For the HLT, studies of achievable physics performance and rejection rates need to be conducted, including the risks and benefits of a possible L4 option.

ETD Performance and Dead Time: The design parameters for the ETD system are driven by trigger rates and dead time constraints, and will need to be studied in detail to determine the requirements for (1) trigger distribution through the FCTS, (2) the FEE/CFEE buffer sizes, and (3) for handling pile-up and overlapping events. Input from the L1 trigger R&D and from background simulation studies will be required.

Event Builder and HLT Farm: The main R&D topics for the Event Builder and HLT Farm are (1) the applicability of existing tools and frameworks for constructing the event builder; (2) the HLT farm framework; and (3), event building protocols and how they map onto network hardware.

Software Infrastructure: To provide the most efficient use of resources, it is important to investigate how much of the software infrastructure, frameworks and code implementation can be shared with Offline computing. This requires us to determine the level of reliability-engineering required in such a shared approach. We also must develop frameworks to take advantage of multi-core CPUs.

8.6 Conclusions

The architecture of the ETD system for Super*B* is optimized for simplicity and reliability at the lowest possible cost. It builds on substantial in-depth experience with the *BABAR* experiment, as well as more recent developments derived from building and commissioning the LHC experiments. The proposed system is simple and safe. Trigger and data readout are fully synchronous—allowing them to be easily understood and commissioned. Safety margins are specifically included in all designs to deal with uncertainties in backgrounds and radiation levels. Event readout and event building are centrally supervised by a FCTS system which continuously collects all the information necessary to optimize the trigger rate. The hardware trigger design philosophy is similar to that of *BABAR* but with better efficiency and smaller latency. The event size remains modest.

The Online design philosophy is similar—leveraging existing experience, technology, and toolkits developed by *BABAR*, the LHC experiments, and commercial off-the-shelf computing and networking components—leading to a simple and operationally efficient system to serve the needs of Super*B* factory-mode data taking.

References

- [1] M. Bona *et al.*, *SuperB: A High-Luminosity Heavy Flavour Factory. Conceptual Design Report*, arXiv:0709.0451v2 [hep-ex], INFN/AE-07/2, SLAC-R-856, LAL 07-15, also available at <http://www.pi.infn.it/SuperB/CDR>.
- [2] B. Aubert *et al.* (BABAR Collaboration), *The BABAR Detector*, Nucl. Instrum. Methods Phys. Res., Sect. A **479**, 1 (2002) [arXiv:hep-ex/0105044].
- [3] The ATLAS Collaboration, *ATLAS Detector and Physics Performance Technical Design Report*, <http://atlas.web.cern.ch/Atlas/GROUPS/PHYSICS/TDR/access.html>.
- [4] The CMS Collaboration, *CMS Detector Technical Design Report*, <http://cmsdoc.cern.ch/cms/cpt/tdr/>.
- [5] The LHCb Collaboration, *LHCb Technical Design Reports*, <http://cmsdoc.cern.ch/cms/cpt/tdr/>.
- [6] The Belle Collaboration, *The Belle Detector*, Nucl. Instrum. Methods Phys. Res., Sect. A **479**, 117 (2002).
- [7] The SPECS Web Page, <https://lhcb.lal.in2p3.fr/Specs/>.
- [8] The BABAR Trigger Web Pages, <http://www.slac.stanford.edu/BFROOT/www/Detector/Trigger/index.html>.

9 Software and Computing

The computing models of the *BABAR* and Belle experiments have proven to be quite successful for a flavor factory in the $\mathcal{L} = 10^{34} \text{ cm}^{-2}\text{s}^{-1}$ luminosity regime. A similar computing model can also work for a super flavor factory at a luminosity of $\mathcal{L} = 10^{36} \text{ cm}^{-2}\text{s}^{-1}$. Data volumes will be much larger, comparable in fact to those expected for the first running periods of the ATLAS and CMS experiments at the LHC, but predictable progress in the computing industry will provide much of the performance increase needed to cope with them. In addition, effective exploitation of computing resources on the Grid, that has become well established in the LHC era, will enable Super*B* to access a much larger set of resources than were available to *BABAR*.

To illustrate the scale of the computing problem and how the Super*B* computing group envisage to attack it, the first part of this section contains an overview of the current *BABAR*-inspired computing baseline model with an estimate of the extrapolated Super*B* computing requirements, followed by a description of the current development and implementation timeline. In the current view, the design phase of the Super*B* computing model is planned to start with a dedicated R&D program in the first year of the project and to finish with the completion of the Computing TDR by the end of the second year.

So far, the main effort of the computing group has been devoted to the development and the support of the simulation software tools and the computing production infrastructure needed for carrying out the detector design and performance evaluation studies for the Detector TDR. Quite sophisticated and extended detector and physics studies can now be performed thanks to:

- the development of a detailed Geant4-based Monte Carlo simulation (Bruno) and of a much faster parametric fast simulation (FastSim) which can directly leverage the existing *BABAR* analysis code base;

- the implementation of a production system for managing very large productions that can parasitically exploit the computing resources available on the European and US Grids.

A description of the tools made available and their capabilities is reported in the second part of the section.

9.1 The Super*B* baseline model

The data processing strategy for Super*B* is envisaged to be similar to the one employed in *BABAR* and can be summarized as follows.

The “raw data” coming from the detector are permanently stored, and reconstructed in a two step process:

- a “prompt calibration” pass performed on a subset of the events to determine various calibration constants.
- a full “event reconstruction” pass on all the events that uses the constants derived in the previous step.

Reconstructed data are also permanently stored and data quality is monitored at each step of the process.

A comparable amount of Monte Carlo simulated data is also produced in parallel and processed in the same way.

In addition to the physics triggers, the data acquisition also records random triggers that are used to create “background frames”. Monte Carlo simulated data, incorporating the calibration constants and the background frames on a run-by-run basis, are prepared.

Reconstructed data, both from the detector and from the simulation, are stored in two different formats:

- the Mini, that contains reconstructed tracks and energy clusters in the calorimeters as well as detector information. It is a relatively compact format, through noise suppression and efficient packing of data.

- the Micro, that contains only information essential for physics analysis.

Detector and simulated data are made available for physics analysis in a convenient form through the process of “skimming”. This involves the production of selected subsets of the data, the “skims”, designed for different areas of analysis. Skims are very convenient for physics analysis, but they increase the storage requirement because the same events can be present in more than one skim.

From time to time, as improvements in constants, reconstruction code, or simulation are implemented, the data may be “reprocessed” or new simulated data generated. If a set of new skims become available, an additional skim cycle can be run on all the reconstructed events.

9.1.1 The requirements

The SuperB computing requirements can be estimated using as a basis the present experience with *BABAR* and applying a scaling of about two orders of magnitude. Fortunately, much of this scaling exercise is quite straightforward.

As a baseline, all rates are simply scaled linearly with luminosity. Only a few parameters have been modified to keep into account improved efficiency of utilization of the computing resources that are likely to be obtained with SuperB, *i.e.*:

- the skimmed data storage requirements have been reduced (by $\sim 40\%$), assuming a more aggressive use of event indexing techniques;
- the CPU requirements for physics analysis are reduced by a factor of two as a result of more stringent optimization goals that can be achieved in SuperB;
- the duration of the reprocessing and simulation re-generation cycle, expected to take place once significant improvements of the reconstruction code physics performance have been obtained, has been set to two years instead of one, as it was in *BABAR*, in view of the larger expected cost-to-benefit ratio;

The resulting CPU and storage requirements are shown in Table 5 for a typical year of data taking at nominal luminosity, assuming an integrated luminosity of 50 ab^{-1} reached at the end of the same year.

Table 5: Summary of computing resources needed in a typical year of SuperB data taking at nominal luminosity, assuming an integrated luminosity of 50 ab^{-1} has been collected.

Parameter	typical Year
Luminosity (ab^{-1})	15
Storage (PB)	
Tape	113
Disk	52
CPU (KHep-Spec06)	
Event data reconstruction	210
Skimming	250
Monte Carlo	670
Physics analysis	570
Total	1700

The total computing resources needed for one year of data taking at nominal luminosity are of the same order as the corresponding figures estimated, in the spring of 2010, by the Atlas and CMS experiments for the 2011 running period, which amounted to 580 KHep-Spec06 for total CPU, 60 PB for disk space, and 47 PB for tape space. However SuperB will profit from the technological advances that will take place over a period of approximately 10 years, and make extensive use of distributed computing resources accessible via the Grid infrastructures. This will give an important degree of flexibility in providing the required level of computing resources.

9.1.2 SuperB offline computing development

The bulk of the SuperB software development effort is foreseen to take place after the Computing TDR is released. All major design choices

should at that time be made, based to a large extent on the results of the R&D activities previously carried out.

In an estimated two years a preliminary version of a fully-functional offline system can be built and validated via dedicated data challenges, so that the collaboration can start using it for detector and physics simulation studies in the fourth project year.

Through further extensive test and development cycles the system will be brought to its full scale size in the following couple of years, before the Super B collider is turned on. Acquisition and deployment of dedicated computing resources will also be carried out during that period as well as consolidation and validation of the distributed computing infrastructure that Super B will have to count on.

This timeline is comparable with the time needed to develop and deploy the *BABAR* offline system.

9.2 Computing tools and services for the Detector and Physics TDR studies

9.2.1 Fast simulation

Because the Super B detector and its machine environment will differ substantially from those at *BABAR*, simple extrapolations of *BABAR* measurements are not adequate to estimate the physics reach of the experiment. Additionally, to make optimal choices in the Super B detector design, an understanding of the effect of design options on the final result of critical physics analyses is needed. However, a detailed simulation of the full Super B detector, with its various options, carried out to the level of statistical precision needed for a relevant physics result, is beyond the capability of the current Super B computing infrastructure.

To address these needs, a fast simulation (FastSim) program has been developed. FastSim relies on simplified models of the detector geometry, materials, response, and reconstruction to achieve an event generation rate several orders of magnitude faster than is possible with a Geant4-based detailed simulation, but with

sufficient detail to allow realistic physics analyses. In order to produce more reliable results, FastSim incorporates the effects of expected machine and detector backgrounds. FastSim is easily configurable, allowing different detector options to be selected at runtime, and is compatible with the *BABAR* analysis framework, allowing sophisticated analyses to be performed with minimal software development.

Event generation Since FastSim is compatible with the *BABAR* analysis framework, we can exploit the same event generation tools used by *BABAR*. On-peak events ($e^+e^- \rightarrow \Upsilon(4S) \rightarrow B\bar{B}$), with the subsequent decays of the B and \bar{B} mesons, are generated through the EvtGen package [1]. EvtGen also has an interface to JETSET for the generation of continuum $e^+e^- \rightarrow q\bar{q}$ events ($q = u, d, s, c$), and for the generic hadronic decays that are not explicitly defined in EvtGen. The Super B machine design includes the ability to operate with a 60–70% longitudinally polarized electron beam, which is especially relevant for tau physics studies. We generate $e^+e^- \rightarrow \tau^+\tau^-$ events with polarized beams using the KK generator and Tauola [2]. Other important physics processes can be generated, such as Bhabha and radiative Bhabha scattering, and $e^+e^- \rightarrow e^+e^-e^+e^-$ or $e^+e^- \rightarrow \gamma\gamma$. More details can be found at the end of this section where the simulation of machine backgrounds is described.

Detector description FastSim models Super B as a collection of *detector elements* that represent medium-scale pieces of the detector. The overall detector geometry is assumed to be cylindrical about the solenoid \vec{B} axis, which simplifies the particle navigation. Individual detector elements are described as sections of two-dimensional surfaces such as cylinders, cones, and planes, where the effect of physical thickness is modeled parametrically. Thus a barrel layer of Si sensors is modeled as a single cylindrical element. Intrinsically thick elements (such as the calorimeter crystals) are modeled by layering several elements and summing their

effects. Gaps and overlaps between the real detector pieces within an element (such as staves of a barrel Si detector) are modeled statistically.

The density, radiation length, interaction length, and other physical properties of common materials are described in a simple database. Composite materials are modeled as admixtures of simpler materials. A detector element may be assigned to be composed of any material, or none.

Sensitive components are modeled by optionally adding a *measurement type* to an element. Measurement types describing Si strip and pixel sensors, drift wire planes, absorption and sampling calorimeters, Cherenkov light radiators, scintillators, and TOF are available. Specific instances of measurement types with different properties (resolutions) can co-exist. Any measurement type instance can be assigned to any detector element, or set of elements. Measurement types also define the time-sensitive window, which is used in the background modeling described below.

The geometry and properties of the detector elements and their associated measurement types are defined through a set of XML files using the EDML (Experimental Data Markup Language) schema, invented for SuperB.

Interaction of particles with matter The SuperB FastSim models particle interactions using parametric functions. Coulomb scattering and ionization energy loss are modeled using the standard parametrization in terms of radiation length and particle momentum and velocity. Molière and Landau tails are modeled. Bremsstrahlung and pair production are modeled using simplified cross-sections. Discrete hadronic interactions are modeled using simplified cross-sections extracted from a study of Geant4 output. Electromagnetic showering is modeled using an exponentially-damped power law longitudinal profile and a Gaussian transverse profile, which includes the logarithmic energy dependence and electron-photon differences of shower-max. Hadronic showering is modeled with a simple exponentially-damped longitudinal profile tuned using Geant4 output.

Unstable particles are allowed to decay during their traversal of the detector. Decay rates and modes are simulated using the BABAR EvtGen code and parameters.

Detector response All measurement types for the detector technologies relevant to SuperB are implemented. Tracking measurements are described in terms of the single-hit and two-hit resolution, and the efficiency. Si strip and pixel detectors are modeled as two independent orthogonal projections, with the efficiency being uncorrelated (correlated) for strips (pixels) respectively. Wire chamber planes are defined as a single projection with the measurement direction oriented at an angle, allowing stereo and axial layers. Ionization measurements (dE/dx) used in particle identification are modeled using a Bethe-Bloch parametrization.

The Calorimeter response is modeled in terms of the intrinsic energy resolution of clusters as a function of the incident particle energy. Energy deposits are distributed across a grid representing the crystal or pad segmentation.

Cherenkov rings are simulated using a lookup table to define the number of photons generated based on the properties of the charged particle when it hits the radiator. Timing detectors are modeled based on their intrinsic resolution.

Reconstruction A full reconstruction based on pattern-recognition is beyond the scope of FastSim. However, a simple smearing of particle properties is insensitive to important effects like backgrounds. As a compromise, FastSim reconstructs high-level detector objects (tracks and clusters) from simulated low-level detector objects (hits and energy deposits), using the simulation truth to associate detector objects. Pattern recognition errors are introduced by perturbing the truth-based association, using models based on observed BABAR pattern recognition algorithm performance.

In tracking, hits from different particles within the two-hit resolution of a device are merged, the resolution degraded, and the resultant merged hit is assigned randomly to one

particle. Hits overlapping within a region of ‘potential pattern recognition confusion’, defined by the particle momentum, are statistically mis-assigned, based on their proximity. The final set of hits associated to a given charged particle are then passed to the *BABAR* Kalman filter track fitting algorithm to obtain reconstructed track parameters at the origin and the outer detector. Outlier hits are pruned during the fitting, based on their contribution to the fit χ^2 , as in *BABAR*.

Ionization measurements from the charged particle hits associated to a track are combined using a truncated-mean algorithm, separately for the SVT and DCH hits. The truncated mean and its estimated error are later used in particle identification (PID) algorithms. The measured Cherenkov angle from the DIRC is smeared according to the Kalman filter track fit covariance at the radiator.

In the calorimeter, overlapping signals from different particles are summed across the grid. A simple cluster-finding based on a local maxima search is run on the grid of calorimeter response. The energies deposited in the cluster cells are used to define the reconstructed cluster parameters (cluster energy and position). A simple track-cluster matching based on proximity of the cluster position to a reconstructed track is used to distinguish charged and neutral clusters.

Machine backgrounds Machine backgrounds at Super*B* are assumed to be dominated by luminosity-based sources, as the Super*B* beam currents will not be much higher than at *BABAR*, which was mostly affected by luminosity-based background. The two dominant processes are radiative Bhabhas and QED two-photon processes ($e^+e^- \rightarrow e^+e^-e^+e^-$). Since the bunch spacing (a few ns) is short relative to the time-sensitive window of most of the Super*B* detectors, interactions from a wide range of bunch crossings must be considered as potential background sources.

Understanding the effect of backgrounds on physics analyses is crucial when making detector design choices, such as the tradeoffs between spatial versus timing resolution, and for under-

standing the physics algorithms required to operate at $\mathcal{L} = 10^{36} \text{ cm}^{-2}\text{s}^{-1}$. Background effects on electronics (hit pileup) and sensors (saturation or radiation damage) are also crucial for Super*B*, but are best studied using the full simulation and other tools.

Background events are generated in dedicated FastSim or Bruno runs. Bruno is needed to model the effect of backgrounds coming from small-angle radiative Bhabha showers in the machine elements, as a detailed description of these elements and the processes involved are beyond the scope of FastSim. Large-angle radiative Bhabhas, and two-photon events, where the primary particles directly generate the background signals, are generated using FastSim. The same *BABAR* generators are used in FastSim and Bruno.

Background events are stored as lists of the generated particles, which are then filtered to save only those which enter the sensitive detector volume. For both the low-angle radiative Bhabha events and the two-photon events, the generated events are combined to correspond to the luminosity of a single bunch crossing at nominal machine parameters, with the actual number of combined events obtained by sampling the appropriate Poisson distribution.

Background events from all sources are overlaid on top of each generated physics event during FastSim simulation. The time origin of each background event is assigned randomly across a global window of $0.5 \mu\text{s}$ (the physics event time origin is defined to be zero). Background events are sampled according to a Poisson distribution whose mean is the effective cross-section of the background process times the global time window.

Particles from background events are simulated exactly as those from the physics event, except that the response they generate in a sensitive element is modulated by their different time origin. In general, background particle interactions outside the time-sensitive window of a measurement type do not generate any signal, while those inside the time-sensitive window generate nominal signals. Background par-

ticle calorimeter response is modeled based on waveform analysis, resulting in exponentially-decaying signals before the time-sensitive window, and nominal signals inside. The hit-merging, pattern recognition confusion and cluster merging described earlier are also applied to background particle signals, so that fake rates and resolution degradation can be estimated from the FastSim output. A mapping between reconstructed objects and particles is kept, allowing analysts to distinguish background effects from other effects.

Analysis tools Because FastSim is compatible with the *BABAR* analysis framework, existing *BABAR* analyses can be run in FastSim with minimal modification. For instance, the vertexing tools and combinatorics engines used in *BABAR* work also in FastSim.

The primary difference is that only a subset of the lists of identified particles (PID lists) available in *BABAR* are available in FastSim. The majority of the available PID lists are based on tables of purities and fake rates extracted from *BABAR*, extended to the additional coverage of Super*B*. A few PID lists based on the actual behavior of the simulated Super*B* detector systems (like dE/dx) are available, but these are of limited utility given the lack of precise calibration or the use of sophisticated statistical techniques like neural nets used in *BABAR* PID lists.

The lack of PID lists also means that the ‘tagging’ (B vs. \bar{B} meson identification) used in *BABAR* does not function in FastSim at present. New tagging algorithms based on the Super*B* detector capabilities, such as the improved transverse impact parameter resolution, have not yet been developed.

The standard tool used in *BABAR* to store analysis information into a ROOT tuple has been adapted to work in FastSim, allowing large analyses to be run in FastSim approximately as in *BABAR*, and to allow the use of *BABAR* analysis macros.

A full mapping of analysis objects back to the particles which generated them (including

background particles) is provided in FastSim, along with the full particle genealogy.

9.2.2 Bruno: the Super*B* full simulation tool

The availability of reliable tools for full simulation is crucial in the present phase of the design of both the accelerator and the detector. For example, the background rate at the sub-detectors needs to be carefully assessed for each modification in the accelerator design and, for a given background scenario, the sub-detectors’ design must be optimized. The full simulation tool can be used to improve the results of the FastSim in some particular cases, as discussed in the following. The choice was made to rewrite from scratch the core simulation software, aiming at having more freedom to better profit from both the *BABAR* legacy and the experience gained in the development of the full simulation for the LHC experiments. Geant4 and the C++ programming language were therefore the natural choices as underlying technology. While the implementation is still at a very early stage, the software is already usable. Basic functionality is in place, and more is being added following user requests. There follows a short overview of the main characteristics, emphasizing areas where future development is planned.

Geometry description The need to re-use as much as possible the existing geometrical description of the *BABAR* full simulation called for some application-independent interchange format to store the information concerning the geometry and materials of the sub-detectors. Among the formats currently used in High Energy Physics applications, the Geometry Description Markup Language (GDML) was chosen because of the availability of native interfaces in Geant4 and ROOT, and the easiness of human inspection and editing provided by the XML-based structure.

Simulation input: Event generators The event generator code can be run either inside the Bruno executable or as a separate process.

In the latter case the results are saved in an intermediate file, which is then read by the full simulation job. Bruno currently supports two interchange formats: a plain text file and one in ROOT format.

Simulation output Hits from the different sub-detectors, which represent the simulated event as seen from the detector, are saved in the output (ROOT) file for further processing. Also the Monte Carlo Truth (MCTruth), intended as a summary of the event as seen by the simulation engine itself, is saved and can be exploited in Bruno in several useful ways, for instance to estimate particle fluxes at sub-detector boundaries by means of full snapshots taken at different scoring volumes.

In staged simulations, snapshots of particles taken at a specific sub-detector boundaries can be saved, read back, and used to start a new simulation process without the need of retracking particles through sub-detectors that sit at inner positions. This allows sub-detectors to assess the effects of layout and geometry changes without the need to run large, computationally-heavy production jobs involving the entire detector.

Interplay with FastSim The event snapshot at a specific sub-detector boundary can also be read by FastSim, allowing a very powerful hybrid simulation approach. For instance the design of the interaction region, which strongly influences the background rates in the detector, cannot be described with the required level of detail in FastSim, while full simulation is not fast enough to generate the high statistics needed for physics studies. By using Bruno to simulate background events up to and including the interaction region, and saving a snapshot of the event without running the entire simulation, one obtains a set of *background frames*, which can be read back in FastSim, that then propagates particles through the simplified detector geometry and adds the resulting hits to the ones coming from signal events.

Another aspect where the interplay between fast and full simulation is needed is the evaluation of the neutron background. The concept is to have Bruno, in addition to handling all particle interactions within the interaction region, as explained above, also track neutrons in the whole detector until they interact or decay, saving the products as part of the background frame used by FastSim. All these functionalities are currently implemented, and have been used in recent production runs.

9.2.3 The distributed production environment

To design the detector and to extract statistically significant results from the data analysis, a huge number of Monte Carlo simulated events is needed. Such a production is way beyond the capacity of a single computing farm so it was decided to design, even to support the detector TDR studies, a distributed model capable of fully exploiting the existing HEP world wide Grid computing infrastructure [3, 4, 5, 6, 7].

The LHC Computing Grid (LCG) architecture [8] was adopted to provide the minimum set of services and applications upon which the SuperB distributed model could be built, and the INFN Tier1 site located at CNAF (Bologna) was chosen as the central site where job submission management, the Bookkeeping Data Base, and the data repository would reside.

Jobs submitted to remote sites transfer their output back to a central repository and update the Bookkeeping Data Base containing all metadata related to the production input and output files. The system uses standard Grid services such as WMS, VOMS, LFC, StoRM, GANGA [9, 10, 11, 12, 13, 14].

The distributed computing infrastructure, as of January 2010, includes several sites in Europe and North America as reported in Table 6. Each site implements a Grid flavor depending on its own affiliation and geographical position. The EGEE Workload Manager System (WMS) allows a job's progress through the different Grid middleware flavors to be managed transparently.

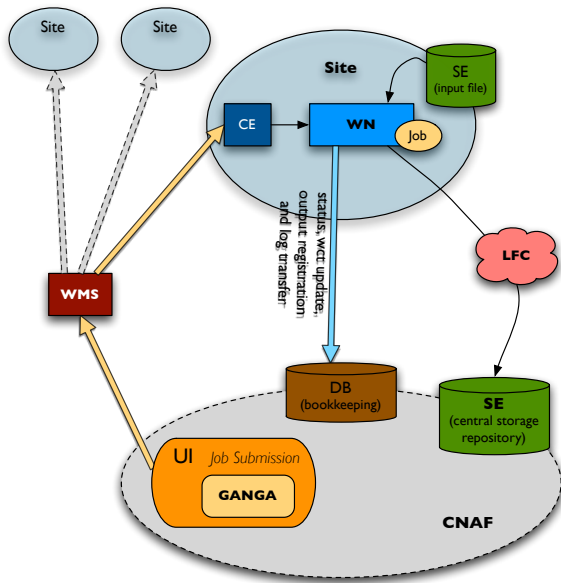


Figure 46: Simulation production work-flow

Table 6: List of sites and Grid technologies involved in SuperB distributed computing model as of January 2010

Site name	Grid flavor
CNAF Tier1, Bologna, Italy	EGEE/gLite
Caltech, California, USA	OSG/Condor
SLAC, California, USA	OSG/Condor
Queen Mary, London, UK	EGEE/gLite
RALPP, Manchester, UK	EGEE/gLite
GRIF, Paris/Orsay, France	EGEE/gLite
IN2P3, Lyon, France	EGEE/gLite
INFN-LNL, Legnaro, Italy	EGEE/gLite
INFN-Pisa, Pisa, Italy	EGEE/gLite
INFN-Bari, Bari, Italy	EGEE/gLite
INFN-Napoli, Napoli, Italy	EGEE/gLite

Simulation production work-flow The production of simulated events is performed in three main phases:

1. Distribution of input data files to remote site Storage Elements (SE). Jobs running on each site are able to access input files from local SE avoiding a file transfer on the Wide Area Network.
2. Job submission, via the SuperB GANGA interface at CNAF, to all available enabled remote sites.

3. Job stage out of files to the CNAF repository.

The job work-flow, shown in Fig. 46, includes also procedures for correctness check, monitoring, data handling and bookkeeping metadata communication. Reliability and fail-over conditions have been implemented in order to maximize the efficiency for copying the output files to the CNAF repository. A replication mechanism permits to store the job output to the local site SE. The job input data management includes an pre-production step: the test release and background files are transferred to all involved sites for access by the jobs at run time. The job submission procedure includes a per site customization to adapt the job actions to site peculiarities: *e.g.*, file transfer to and from three different data handling systems: StoRM [13], dCache [15] and DPM [16].

Production Tools Both the job submission system and the individual physicist require a way to identify interesting data files and to locate the storage holding them. To make this possible, the experiment needs a data bookkeeping system to maintain the semantic information associated to data files and keep track of the relation between executed jobs and their parameters and outputs.

Moreover, a semi-automatic submission procedure is needed in order to keep data consistent, to speed up production completion and to provide an easy-to-use interface for non-expert users. To accomplish this task, a web-based user interface has been developed which takes care of the database interactions and the job preparation; it also provides basic monitoring functionalities.

The bookkeeping database was modeled according to the requirements specified by the collaboration, and implemented adhering to the relational model with MySQL rDBMS. It was extensively tested against the most common use cases and provides a central repository of the production metadata.

A Web-based User Interface (WebUI) has been developed that is bound to the bookkeeping database which provides inputs for the job preparation and monitoring.

It presents two different sections for Full Simulation and Fast Simulation, each of which is divided into submission and monitor subsections. A basic authentication and authorization layer, based on the collaborative tools permits the differentiation of users and grants access to the corresponding sections of the site.

A typical production workflow consists of an initialization phase, during which the data of a bunch (or several bunches) of jobs is inserted into the database, and of the subsequent phase of submission either to a batch system or to a distributed environment. The simulation jobs interact extensively with the database during their lifetime to update data and insert outputs and logs.

A production software layer and a database manager layer have thus been developed to interface the database with the jobs. The prototype service uses a RESTful [17] interface in order to allow the communications between centralized or distributed jobs and a centralized database.

The WebUI provides basic monitoring features by querying the bookkeeping database. The user can retrieve the list of jobs as a function of run number range, generator, geometry, physics list, site, status, etc. The monitor provides, for each job, the list of output files – if any – and direct access to the log files. Reports on output file size, execution time, site loading, job spread over channels, and the list of the most recently completed jobs (successfully or with failures) are also provided.

Remote Grid sites Sites involved in the SuperB distributed computing infrastructure need to enable the superbvo.org Virtual Organization (VO) and install the SuperB FastSim software as specified in the VO Identity Card. Currently no permanent storage is required at the sites, and memory requirements are modest (2 Gbyte RAM per core and 2 Gbyte virtual memory).

First 2010 production runs The production system has been used during the first large scale Bruno and FastSim production in January, February and March 2010. During this production phase, over 1.7 billion simulation events, equivalent to $\sim 0.2 \text{ ab}^{-1}$, were produced using the distributed computing environment.

The Bruno production was divided in two categories: simulation of machine background frames for FastSim (bgframes) and full simulation for machine background studies (bgstudies). The entire Bruno production ran at CNAF in about 12 days. Table 7 shows the production summary.

Table 7: Full Simulation Production Summary

2010_01_bgframes			
Geometry	Status	Jobs	Events
SuperB	done	4000	10^6
SuperB	failed	1	250
SuperB	sys-failed	1	250
2010_02_bgstudies			
Geometry	Status	Jobs	Events
shielded	done	4840	604000
shielded	sys-failed	1	100
unshielded	done	785	196250
unshielded	failed	2	500
unshielded	sys-failed	13	3250

The FastSim production was divided into two categories: simulation of generic events ($B^0\bar{B}^0$, B^+B^- , $c\bar{c}$ and uds); and simulation of specific decay channels (signal mode).

For generics, four generators and three geometry configurations were used. Events with and without background mixing were produced. In the signal mode production, four physics channels events were simulated with background mixing. Results are summarized in Table 8.

FastSim production involved nine remote sites; about 82% of submitted jobs used the Grid infrastructure, exploiting remote resources, as illustrated in Fig. 47 for the generics production.

9.2 Computing tools and services for the Detector and Physics TDR studies 75

Table 8: Fast Simulation Production Summary

2010_February_Generics		
Bkg	Jobs	Events
Y	4508	104.340×10^6
N	14672	1472.100×10^6
Total	19180	$\approx 1.58 \times 10^9$
2010_February_Signal		
Signal	Jobs	Events
BtoTauNu	30	3×10^6
BtoKNUu	60	6×10^6
BtoKstarNuNu	60	6×10^6
BtoKplusNuNu	688	68.8×10^6
Total	838	83.8×10^6

Over a period of 2 weeks, approximately 20000 jobs were completed with an average $\sim 8\%$ failure rate, mainly due to site misconfigurations (2.6%), proxy expiration (2.0%), and temporary overloading of the machine used to receive the data transfers from the remote sites at CNAF (3%). The peak rate reached 3200 simultaneous jobs with an average of 500.

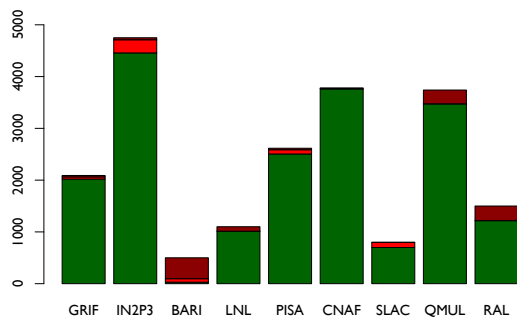


Figure 47: Jobs submitted to remote sites for the Generics Production.

9.2.4 The software development and collaborative tools

As a collaboration facing the task of preparing design documents and developing software

code, the SuperB group needs to be supported by a set of suitable computing tools in carrying out its day-by-day coordinated activities. A description of currently available tools is presented here.

Directory Service To support the access to the collaborative tools through a unique authentication and authorization interface, a directory service based on LDAP application protocol was made available and it has been now actively used for more than one year. A web interface to provide an easy way to manage the directory tree has also been set up by modifying open source software and is ready to enter the testing phase. In choosing all the other tools we put a great emphasis on the ability to integrate with the directory service.

Web site To make the inclusion of information content easier for the collaborators it was decided to create a web site managed by a content management system (CMS). After some testing phase and initial experience with Drupal, the Joomla open source CMS [18] was selected due to its user-friendly interface and widespread use in INFN. Two web sites were created, the first addressing the needs of the SuperB group and the second dedicated to the general public.

Wiki In addition to the web sites, the collaboration has realized from the beginning the need for a Wiki site that permits the easy creation of web pages to be used as internal documentation, to create meaningful topic associations between different pages, and simple editing of existing pages, keeping track of recent changes. The Wiki server [19] is currently up and running, integrated with the directory service and is used by several sub-detector groups in the collaboration.

Software repository A source code management system is needed to manage the production of software code. The Subversion [20] open source tool was selected as the most suitable for SuperB at this stage of the project. Due to the

multi-developer way of producing code within a collaboration like SuperB the repository was the first tool deployed and integrated with the directory service.

9.2.5 Code packaging and distribution

As almost all the computing power available in the collaborating institutes is made of Linux boxes with Red Hat or Scientific Linux distributions, it was decided to build releases only for these operating systems, in particular the builds are available for *RH/SL* 4.6 and for *RH/SL* 5.1 for 32 bit architectures. Work is ongoing to extend the support also for 64 bit architectures. Support for MacOSX is also under study, although it might require some time and dedicated effort, given that this system is quite different from Linux.

Tools To ease distribution and installation, SuperB software is packaged with *RPM* [21] and distributed with *yum* [22], along with external software used by it, such as *ROOT* [23], *Geant4* [24], *CLHEP* [25], *CERNLIB* [26] and *Xerces-c* [27]. The reason to have a specific experiment version/packaging for these tools is to avoid conflicts with other experiments using a different release of the same software, or the same release build with different options. To improve security packages are signed in order to guarantee their origin. To distribute the software yum repositories have been set up, one per architecture.

References

- [1] <http://robbep.home.cern.ch/robbep/EvtGen/GuideEvtGen.pdf>.
- [2] S. Jadach, B. F. L. Ward, and Z. Was, *Comput. Phys. Commun.* **130**, 260 (2000), arXiv:hep-ph/9912214.
- [3] <http://www.eu-egee.org>.
- [4] <http://www.opensciencegrid.org>.
- [5] <http://www.nordugrid.org>.
- [6] <http://www.westgrid.ca>.
- [7] The LCG TDR Editorial Board, *LHC Computing Grid, Technical Design Report* LCG-TDR-001, CERN-LHCC-2005-024 (2005).
- [8] <http://lcg.web.cern.ch/LCG>.
- [9] <http://glite.web.cern.ch/glite>.
- [10] <http://hep-project-grid-scg.web.cern.ch/hep-project-grid-scg/voms.html>.
- [11] <https://twiki.cern.ch/twiki/bin/view/LCG/LfcAdminGuide>.
- [12] <http://sdm.lbl.gov/srm-wg/doc/SRM.v2.2.html>.
- [13] A Corso *et al.*, *StoRM, an SRM Implementation for LHC Analysis Farms*, in *Computing in High Energy Physics (CHEP 2006)*, Mumbai, India, Feb. 13–17.
- [14] <http://ganga.web.cern.ch/ganga>.
- [15] P. Fuhrmann and V. Glzow, *dCache, Storage System for the Future*. New York: Lecture Notes in Computer Science (Springer, 2006), Vol. 4128, pp. 1106–1113.
- [16] https://twiki.cern.ch/twiki/pub/LCG/DataManagementUsefulPresentations/chep07_poster_DPM.ppt.
- [17] Fielding R.T., *Architectural Styles and the Design of Network-based Software Architectures*, PhD. Thesis, University of California Irvine, 2000.
- [18] <http://www.joomla.org/>.
- [19] <http://www.mediawiki.org/wiki/MediaWiki>.
- [20] <http://subversion.apache.org/>.
- [21] <http://www.rpm.org/>.
- [22] <http://yum.baseurl.org/>.
- [23] <http://root.cern.ch/>.
- [24] <http://geant4.web.cern.ch/geant4/>.
- [25] <http://proj-clhep.web.cern.ch/proj-clhep/>.
- [26] <http://cernlib.web.cern.ch/cernlib/>.
- [27] <http://xerces.apache.org/xerces-c/>.

10 Mechanical Integration

10.1 Introduction

The *BABAR* detector was built to a design optimized for operations at a high luminosity asymmetric B meson factory. The detector performed well during the almost nine years of colliding beams operation, at luminosities three times the PEP-II accelerator design. There are substantial cost and schedule benefits that result from reuse of detector components from the *BABAR* detector in the Super B detector in instances where the component performance has not been significantly compromised during the last decade of use. These benefits arise from two sources: one from having a completed detector component which, though it may require limited performance enhancements, will function well at the Super B Factory; and the other from requiring reduced interface engineering, installation planning and tooling manufacture (most of the assembly/disassembly tooling can be reused). The latter reduces risk to the overall success of the mechanical integration of the project. Though reuse is very attractive, risks are also introduced. Can the detector be disassembled, transported, and reassembled without compromise? Will components arrive in time to meet the project needs?

The reuse of elements of the PID, EMC and IFR system, and associated support structures have been described in previous chapters. In this section, issues related to the magnet coil and cryostat, and the IFR steel and support structure are discussed as well as the integration and assembly of the Super B detector, which begins with the disassembly of *BABAR*, and includes shipping components to Italy for reassembly there.

10.1.1 Magnet and Instrumented Flux Return

The *BABAR* superconducting coil, its cryostat and cryo-interface box, and the helium compres-

sor and liquefier plant will be reused in whole or in part. The magnet coil, cryostat and cryo-interface box will be used in all scenarios. Use of on-detector pumps and similar components may not be cost effective due to electrical incompatibility. An initial review of local refrigeration facilities at the proposed Frascati Super B site suggests that there may not be sufficient capacity in that system to cool both the detector magnet and the final focus superconducting magnets. The existing *BABAR* helium liquefier plant, which is halfway through its forty year service life, has sufficient capacity. The final decision about reuse of these external service components will take into account electrical compatibility, schedule and cost.

The initial *BABAR* design contained too little steel for quality μ identification at high momentum. Additional brass absorber was added during the lifetime of the experiment to compensate. The flux return steel is organized into five structures: the barrel portion, and two sets of two end doors. Each of these is, in turn, composed of multiple structures. The substructures were sized to match the 50 ton load limit of the crane in the *BABAR* hall.

Each of the end doors is composed of eighteen steel plates organized into two modules joined together on a thick steel platform. This platform rests on four columns with jacks and Hilman rollers. A counterweight is also located on the platform. There are nine steel layers of 20 mm thickness, four of 30 mm thickness, four of 50 mm thickness, and one of 100 mm thickness. During 2002, five layers of brass absorber were installed in the forward end door slots in order to increase the number of interaction lengths seen by μ candidate tracks. In the baseline, these doors will be retained, including the five 25 mm layers of brass installed in 2002, as well as the outer steel modules which can house two additional layers of detectors. Additional layers of brass or steel will be added, following the specification of the baseline design in the instrumented flux return section. A cost-benefit analysis will be performed to choose between brass and steel. The aperture of the forward

plug must be opened to accommodate the accelerator beam pipe. Compensating modifications to the backward plug are likely to be necessary. These modifications to the steel may affect the central field uniformity and the centering forces on the solenoid coil, and so must be carefully re-engineered.

The barrel structure consists of six cradles. These are each composed of eighteen layers of steel. The inner sixteen layers have the same thicknesses as the corresponding end door plates. The two outermost layers are each 100 mm thick. The eighteen layers are organized into two parts; the inner sixteen layers are welded into a single unit along with the two side plates, and the outer two layers are welded together and then bolted into the cradle. The six cradles are in turn suspended from the double I-beam belt that supports the detector. During the 2004/2006 barrel LST upgrade, layers of 22 mm brass were installed, replacing six layers of detectors in the cradles. In the Super*B* baseline, these brass layers will be retained, as well as all the additional flux return steel attached to the barrel in the gap between the end doors and barrel. As in the end doors, additional layers of absorber will be placed in gaps occupied in *BABAR* by LSTs. In order to provide more uniform coverage at the largest radius for the μ identification system, modifications to the sextant steel support mechanism are likely to be needed. Finite element analyses are in progress to confirm that deflections of the steel structure due to this alternative support mechanism do not reduce inter-plate gaps needed for the tracking detectors.

10.2 Component Extraction

Extraction of components for reuse requires the disassembly of the *BABAR* detector. This process began after the completion of *BABAR* operations in April 2008. The first stage of the project was to establish a minimal maintenance state, including stand alone environmental monitoring, that preserves the assets that have reuse value. The transition was complete in August. In order to disassemble the detector into its component

systems, it must be moved off the accelerator beam line where it is pinned between the massive supports of accelerator beamline elements into the more open space in the IR2 Hall. This required removal of the concrete radiation shield wall, severing of the cable and services connections to the electronics house which contained the off detector electronics, and roll-back of the electronics house 14 m. Electronics, cables and infrastructure that were located at the periphery of the detector were removed. Beamline elements close to the detector were removed to allow access to the central core of the detector by July 2009, allowing removal of the support tube, which contained the PEP-II accelerator final beamline elements as well as the silicon vertex detector, the following month.

The core disassembly sequence was optimized after the Conceptual Design Report. Completion of disassembly of the detector now requires fewer steps, less time, and poses fewer risks, with the end doors being disassembled while the detector is on beamline. As of mid-May 2010, three of the four end doors have been broken down into component parts, and the EMC forward endcap and the drift chamber have been removed, with the final end door breakdown to be completed within a month.

This work has been accomplished as a low priority project with a small crew of engineers and technicians. Though the disassembly project is behind schedule, due to laboratory priorities, the earned value compared to actual costs indicates that the level of effort estimated to perform the disassembly is very accurate. The same methodology used to determine the level of effort needed for the *BABAR* disassembly has been applied in estimating the needs for Super*B* assembly.

The components from *BABAR* that are expected to be reused in Super*B* are expected to be available for transport to Italy in mid-2011. This should present no challenge to the Super*B* project schedule. The remaining steps in the *BABAR* disassembly, which represents more than half of the effort, are outlined below. Tooling that was used in the initial installation of the

detector at IR2 is in the process of being refurbished and additional tooling is being fabricated for the disassembly effort. All of this tooling is available for use on SuperB.

After rolling off the beamline, the next phase of detector disassembly consists of extraction of the DIRC and its support system from the core of the detector. The SOB camera is first removed and will not be reused. In order to minimize the possibility of damage to the DIRC bar boxes and their fused silica bar content, disassembly proceeds with removal of the bar boxes one by one from the bar box support structure inside the DIRC. The twelve bar boxes will be stored in an environmentally controlled container to await shipment to Italy. The DIRC structure is then removed from the barrel.

The barrel EMC is then removed from the barrel steel. The solenoid is removed from the barrel steel. A temporary structure is assembled inside the barrel hexagon to support the upper cradles during disassembly. The upper half of the support belt is removed. Because of the load limitations of the IR2 crane, the six cradles must be disassembled in situ. The outer sections of the top cradles are removed, followed by the inner part of each of the three cradles. The temporary support structure is removed. The inner part of the lower cradles is removed, followed by the outer portions. The balance of the structural belt is disassembled.

10.3 Component Transport

The magnet steel components will be crated for transport to limit damage to mating surfaces and edges. Most, if not all, of these components can be shipped by sea.

The *BABAR* solenoid was shipped via special air transport from Italy to SLAC. It is expected that this component can be returned to Italy in the same fashion. The original transport frame needs some refurbishment. Drawings exist for parts fabrication so that only a small engineering effort is needed here.

The DIRC and barrel calorimeter present transportation challenges. In both cases transport without full disassembly is preferred. In

the case of the DIRC, the central support tube will be separated from the strong support tube and transported as an assembly, assuming that engineering studies indicate that this is possible. The transport cradle for the central support tube has had no design effort yet. The bar boxes have a storage container which provides a dry environment. Whether this can be used for air transport, or a newly designed and fabricated container is required, remains to be determined. Disassembly of the bar boxes exposes the precious bars to damage; it is not considered a viable option.

In the case of the EMC, there are two environmental constraints on shipment of the device or its components. The glue joint that attached the photodiode readout package to the back face of the crystal has been tested, in mock-up, to be stable against temperature swings of $\pm 5^\circ\text{C}$. During the assembly of the endcap calorimeter, due to a failure of an air conditioning unit, the joints on one module were exposed to double this temperature swing. Several glue joints parted. The introduction of a clean air gap causes a light yield drop of about 25%. In order to avoid this reduction in performance, temperature swings during transport must be kept small. Since the crystals are mildly hygroscopic, it is best that they be transported in a dry environment to avoid changes in the surface reflectivity, and consequent modification in the longitudinal response of the crystal. Individual *BABAR* endcap modules constructed in the UK were successfully shipped to the USA in specially constructed containers that kept the temperature swings and humidity acceptably small.

Disassembly of the barrel calorimeter for shipment presents a substantial challenge. Both the disassembly and assembly sites need to be temperature and humidity controlled. The disassembly process requires removal of the outer and inner cylindrical covers, removal of cables that connect the crystals with the electronics crates at the ends of the cylinder, splitting of the cylinder into its two component parts and removal of the 280 modules for shipment. Though much of the tooling is still in hand, the environmentally

conditioned buildings used in calorimeter construction at SLAC no longer exist, though alternative facilities could be outfitted. The cooling and drying units used in the module storage/calorimeter assembly building continue to be available.

The clear preference is to ship the barrel calorimeter as a single unit by air. With tooling support stand and environmental conditioning equipment, the load is likely to exceed 30 tons. It is anticipated that such a load could be transported in the same way as the superconducting coil and its cryostat, but verification is needed. Detailed engineering studies, which model accelerations and vibrations involved with flight that might cause the crystal containing carbon fiber modules to strike against one another, are needed to determine if the calorimeter can be safely transported. It may be that a module restraint mechanism will need to be engineered and fabricated. A transport frame must be designed and its performance modeled. Engineering studies have begun.

10.4 Detector Assembly

Assembly of the Super B detector is the inverse of the disassembly of the $BABAR$ detector. Ease

of assembly will be influenced by the facilities which are available. In the case of $BABAR$, the use of the IR2 hall, which was "too small", led to engineering compromises in the design of the detector. Assembly was made more complicated by the weight restrictions posed by the 50 ton crane. Upgrades were made more difficult because of limitations in movement imposed by the size of the hall.

The preferred dimensions for the area around the Super B detector when it is located in the accelerator housing are 16.2m transverse to the beamline, 20.0m along the beamline, 11.0m from the floor to the bottom of the crane hook, 15.0m from floor to ceiling, and 3.7m from the floor to the beamline. The increased floor to beamline height relative to $BABAR$ -PEP-II, will require redesign effort for the underpinnings of the detector cradle. However, this will permit improved access for installation of cable and piping services for the detector, as well as make possible additional IFR absorption material for improved μ detector performance below the beamline. In order to facilitate detector assembly, the preferred capacity for the two hook bridge crane is 100/25 tons.

11 Budget and Schedule

The Super*B* detector cost and schedule estimates, presented in this chapter, rely heavily on experience with the *BABAR* detector at PEP-II. The reuse and refurbishing of existing components has been assumed whenever technically possible and financially advantageous. Though these Super*B* estimates are based on a bottoms-up evaluation using a detailed work breakdown schedule, it should be emphasized that the detector design is still incomplete, with numerous technical decisions remaining to be made, and limited detailed engineering to date, so that that cost and schedule can not yet be evaluated at the detailed level expected in a technical design report.

The costing model used here is similar to that already used for the Super*B* CDR. The components are estimated in two different general categories; (1) “LABOR” and, (2) M&S (Materials and Services). M&S cost estimates are given in 2010 Euros and include 20% of Value Added Tax (VAT). The “LABOR” estimates comprise two sub categories which are kept and costed separately as they have differing cost profiles; (1) EDIA (Engineering, Design, Inspection, and Administration) and (2) Labor (general labor and technicians). Estimates in both categories are presented in manpower work units (Man-Months) and not monetized, as a monetary conversion can only be attempted after institutional responsibilities have been identified and the project timescale is known. The total project cost estimate can be calculated, once the responsibilities are identified, by summing the monetary value of these three categories.

Given the long term nature of this multinational project, there are several challenging general issues in arriving at appropriate costs including (1) fluctuating currency exchange rates, and (2) escalation. M&S costs and factory quotes that have been directly obtained in Euros can be directly quoted. M&S estimates in US Dollars are translated from Dollars to Euros using the exchange rate as of Jun 1, 2010

(0.8198 Euros/US\$). For costs in Euros that were obtained in earlier years, the yearly escalation is rather small. For simplicity, we use a cost escalation rate of 2% per year which is consistent with the long term HICP (Harmonized Index of Consumer Prices) from the European Central Bank. Costs given in 2007 Euros are escalated by the net escalation rate (1.061) for three years to arrive at the 2010 cost estimates given here [1].

For all items whose cost basis is *BABAR*, we accept the procedure outlined in the Super*B* CDR which arrived at the costs given there in 2007 Euros. This procedure escalated the corresponding cost (including manpower) from the PEP-II and *BABAR* projects from 1995 to 2007 using the NASA technical inflation index [2] and then converted from US Dollars to Euros using the average conversion rate over the 1999—2006 period [3]. The overall escalation factor in the CDR from 1995 Dollars to 2007 Euros is thus $1.21 = 1.295 \times 0.9354$.

Similarly, the replacement values (“Rep.Val.”) of the reused components, *i.e.*, how much money would be required to build them from scratch, as presented in separate columns of the cost tables, have been obtained by escalating the corresponding *BABAR* project cost (including manpower) from 1995 to 2007. Though it is tempting to sum the two numbers to obtain an estimate of the cost of the project if it were to be built from scratch, this procedure yields somewhat misleading results because of the different treatment of the manpower (rolled up in the replacement value; separated for the new cost estimate) and because of the double counting when the refurbishing costs are added to the initial values.

Contingency is not included in the tables. Given the level of detail of the engineering and the cost estimates, a contingency of about 35% would be appropriate.

11.1 Detector Costs

The costs, detailed in Table 9, are presented for the detector subsystem at WBS level 3/4.

Table 9: SuperB detector budget.

WBS	Item	EDIA mm	Labor mm	M&S kEuro	Rep.Val. kEuro
1	SuperB detector	4037	2422	52953	48922
1.0	Interaction region	21	12	860	0
1.0.1	Be Beampipe	10	4	260	0
1.0.1.1	Vertex chamber design	4	0	0	0
1.0.1.2	Finalize Physics Req.mnts	1	0	0	0
1.0.1.3	Fab method	1	0	0	0
1.0.1.4	Design Review	1	0	0	0
1.0.1.5	Chamber detailing	2	0	0	0
1.0.1.6	Support procurement	2	0	5	0
1.0.1.7	Procure Beampipe Assembly	0	0	243	0
1.0.1.8	Procure Vx chamber Misc parts	0	0	12	0
1.0.1.9	Assemble Vx chamber, test, clean	0	2	0	0
1.0.2	Tungsten Shield	9	6	540	0
1.0.2.1	Shield optimization	3	0	0	0
1.0.2.2	Shield detailing and integration	3	0	0	0
1.0.2.3	Shield procurement	1	0	540	0
1.0.2.4	Shield assembly and installation	2	6	0	0
1.0.3	Radiation monitors	2	2	60	0
1.1	Tracker (SVT + Strip + MAPS)	408	442	6444	0
1.1.1	SVT	222	309	4326	0
1.1.1.1	Mechanical	48	129	399	0
1.1.1.2	Cooling	8	10	155	0
1.1.1.3	Silicon Wafers and Fanout	24	120	2642	0
1.1.1.4	On-detector electronics	72	42	1013	0
1.1.1.5	Detector monitoring	4	4	92	0
1.1.1.6	Detector assembly	6	4	0	0
1.1.1.7	System Engineering	60	0	24	0
1.1.2	L0 Striplet option	36	55	542	0
1.1.2.1	Mechanical	12	30	60	0
1.1.2.2	Cooling	3	3	48	0
1.1.2.3	Silicon Wafers and Fanout	16	18	327	0
1.1.2.4	On-detector electronics	5	4	108	0
1.1.3	L0 MAPS option	150	78	1576	0
1.1.3.1	Mechanical	18	48	90	0
1.1.3.2	Cooling	6	6	96	0
1.1.3.3	MAPS Modules Components	126	24	1390	0
1.1.4	L0 Hybrid Pixel option	156	84	1684	0
<i>1.1.4.1</i>	<i>Mechanical</i>	<i>18</i>	<i>48</i>	<i>90</i>	<i>0</i>
<i>1.1.4.2</i>	<i>Cooling</i>	<i>6</i>	<i>6</i>	<i>96</i>	<i>0</i>
<i>1.1.4.3</i>	<i>Hybrid Pixel Modules Components</i>	<i>132</i>	<i>30</i>	<i>1498</i>	<i>0</i>
1.2	DCH	165	139	3421	0
1.2.1	System engineering	24	0	60	0
1.2.2	Endplates	16	6	660	0
1.2.3	Inner cylinder	8	2	200	0
1.2.4	Outer cylinder	6	2	120	0
1.2.5	Wire	4	6	308	0
1.2.6	Feedthroughs	9	10	439	0
1.2.7	Endplate systems	8	0	385	0
1.2.8	Assembly & Stringing	74	96	960	0
1.2.9	Gas System	10	8	240	0
1.2.A	Test	6	9	48	0

Continued on next page

Table 9 – continued from previous page

WBS	Item	EDIA mm	Labor mm	M&S kEuro	Rep.Val. kEuro
1.3	PID	116	236	5820	7138
1.3.1	DIRC Barrel (Focusing DIRC)	116	236	5820	7138
1.3.1.1	Radiator Support Structure	4	4	10	2516
1.3.1.2	Radiator box/FBLOCK assembly	14	40	2819	4515
1.3.1.3	New Camera mechanical boxes	14	28	305	0
1.3.1.4	Photodetector assembly	18	32	2607	0
1.3.1.5	Calibration System	2	4	59	0
1.3.1.6	Mechanical Utilities	4	8	20	107
1.3.1.7	System Integration	60	120	0	0
1.4	EMC	219	360	12147	31574
1.4.1	Barrel EMC	20	5	205	31574
1.4.1.1	Crystal Procurement	0	0	0	21742
1.4.1.2	Light Sensors & Readout	0	0	0	2654
1.4.1.3	Crystal Support Modules	0	0	0	2875
1.4.1.4	Barrel Structure	0	0	0	3419
1.4.1.5	Calibration Systems	0	0	0	650
1.4.1.6	Project Management	0	0	0	233
1.4.1.7	Barrel Transport	20	5	205	0
1.4.2	Forward EMC	171	312	11565	0
1.4.2.1	Crystal Procurement	25	102	9403	0
1.4.2.2	Light Sensors & Readout	47	70	992	0
1.4.2.3	Crystal Support Modules	26	64	450	0
1.4.2.4	Endcap Structure	26	52	444	0
1.4.2.5	Calibration Systems	24	24	156	0
1.4.2.6	Project Management	24	0	120	0
1.4.3	Backward EMC	28	43	377	0
1.4.3.1	Scintillator	2	10	121	0
1.4.3.2	Radiator	1	4	22	0
1.4.3.3	Fibers	4	8	18	0
1.4.3.4	Photodetectors	2	5	46	0
1.4.3.5	Mechanical support	17	15	146	0
1.4.3.6	Project Management	2	2	24	0
1.5	IFR	37	184	1374	0
1.5.1	Scintillators	0	0	266	0
1.5.2	WLS fibers	0	0	362	0
1.5.3	Photodetectors and PCBs	1	2	685	0
1.5.4	Mechanics (Production and QC)	16	62	60	0
1.5.5	Module Installation	20	120	0	0
1.6	Magnet	93	59	3767	10210
1.6.0	System Management	36	0	0	612
1.6.1	Superconducting solenoid	0	0	0	2421
1.6.2	Mag. Power/Protection	0	0	0	181
1.6.3	Cryogenics	34	36	1753	0
1.6.4	Cryo monitor/Control	17	11	214	0
1.6.5	Flux return	6	12	1800	6481
1.6.6	Installation/test equipment	0	0	0	515
1.7	Electronics	994	342	9234	0
1.7.1	SVT	11	21	561	0
1.7.2	DCH	74	76	1668	0
1.7.3	PID Barrel (32k channels)	136	18	612	0
1.7.4	EMC	110	164	2726	0
1.7.5	IFR	38	51	1487	0
1.7.6	Infrastructure	4	12	314	0

Continued on next page

Table 9 – continued from previous page

WBS	Item	EDIA mm	Labor mm	M&S kEuro	Rep.Val. kEuro
1.7.7	Systems Engineering	12	0	0	0
1.7.8	Hardware Trigger	97	0	678	0
1.7.9	ETD (without Trigger)	512	0	1188	0
1.8	Online System	912	24	2074	0
1.8.1	Event Flow	282	0	1676	0
1.8.2	Run Control / Slow Controls / ECS	270	0	53	0
1.8.3	Infrastructure	48	12	246	0
1.8.4	Software Triggers	216	0	0	0
1.8.5	Coordination and Commissioning	72	12	0	0
1.8.6	Online System R&D	24	0	98	0
1.9	Installation and integration	353	624	7596	0
1.9.1	Disassembly	95	161	612	0
1.9.2	Assembly	222	463	3984	0
1.9.3	Structural analysis	36	0	0	0
1.9.4	Transportation	0	0	3000	0
1.A	Project Management	720	0	216	0
1.A.1	Project engineering	300	0	120	0
1.A.2	Budget, Schedule and Procurement	300	0	48	0
1.A.3	ES & H	120	0	48	0

The SuperB detector is not completely defined: some components, such as the forward PID, have overall integration and performance implications that need to be carefully studied before deciding to install them; for some other components, such as the SVT Layer0, promising new technologies require additional R&D before they can be definitively used in a full scale detector. The cost estimates list the different technologies separately, but the rolled-up value includes the baseline detector choice that is considered most likely to be used. Technologies that are not included in the rolled-up value are shown in italics.

11.2 Basis of Estimate

Vertex Detector and Tracker: System cost is estimated based on experience with the *BABAR* detector and vendor quotes. A detailed estimate is provided for the cost of the main detector (layers 1 to 5). The costs associated with Layer0 are analyzed separately. The costing model assumes that a triplet detector will be installed initially – followed by a second generation upgrade to a pixel detector, which could either be either a MAPs or hybrid pixel device. Substantial R&D on these new technologies is needed in either case before such a detector can be built. The total SVT cost is obtained by summing the baseline detector cost (with triplets for Layer0) to the MAPS Layer0 cost.

Drift Chamber: The DCH costing model is based on a straightforward extrapolation of the actual costs of the existing *BABAR* chamber to 2010, since, as discussed in Sec. 4 the main design elements are comparable, and many related components, such as the length of wire, number of feedthroughs, duration of wire stringing, etc., can be reliably estimated. Although the cell layout is still being finalized, the total cell count will likely be about 25% larger. The endplates will be fabricated from carbon fiber composites instead of aluminum. Though this will require a somewhat longer period of R&D and engineering design, it is unlikely to result in significantly larger production costs for the final endplates.

The DCH electronics on Table 9 assumes standard readout as discussed in Sec. 8.4.2. A *cluster counting* readout option is under R&D, but is not yet sufficiently advanced that costs can be provided.

Particle Identification: Barrel PID costs and replacement values are derived from *BABAR* costs as extrapolated to 2010, with updated quotes from vendors. The main new component of the barrel FDIRC is its new camera. For each module, the optical portion consists of the focusing block (FBLOCK), an addition to the wedge (the New Wedge) and possibly a Micro-Wedge. We have contacted about twelve optics companies and received four preliminary bids. We use the average bid in the present budget. We hope to continue to refine the values through further R&D. The photon detector cost estimate is based on the Hamamatsu bid for 600 H-8500 MaPMTs. No budget estimate is included at this time for a forward endcap PID. Though several options are being studied, their performance and cost are yet to be well understood, and the overall performance gains and losses of including a forward PID in the detector are as yet unsettled. However, as a general principle, given the limited solid angle covered by such a device, the cost of a forward PID detector must be a modest fraction of the barrel.

Electromagnetic Calorimeter: There are four components to the calorimeter cost: (1) the barrel calorimeter from *BABAR*; (2) the forward calorimeter; (3) the replacement of the front-end preamps in the barrel; and (4) the backward calorimeter. As described in the calorimeter section, there are a number of uncertainties remaining in the design. The present cost estimate is for our baseline design.

The reuse value of the barrel calorimeter is based on the actual cost of the barrel escalated for inflation from the time of construction to the current year. Manpower estimates for the barrel construction were obtained by using the costs for EDIA and Labor, knowledge of the mix

of engineers and technicians who contributed to the design and fabrication of individual components, and knowledge of their salaries. Manpower and costs for engineering and tooling required for the removal and transport of the barrel EMC from SLAC are engineering estimates.

The main cost driver for the forward endcap is the cost of LYSO crystals. This is estimated based on guideline quotes from vendors. The next largest element is the APD photodetectors, with a cost based on a quote from the vendor. The estimate for the crystal support modules is based on costs for the beam test prototype. Estimates for the remaining smaller items are based on estimator experience and judgment.

The cost estimate for replacing the preamplifiers in the barrel calorimeter is based on the endcap preamplifier cost as well as the cost of dealing with the mechanical issues.

For the backward endcap, the scintillator, lead, wavelength-shifting fiber, and readout MPPC costs, as well as some other minor materials, are all based on vendor quotes. Other items are based on experience and estimator judgment.

Instrumented Flux Return: The IFR cost is based on quotations received for the prototype construction appropriately scaled to the real detector dimensions. While the active part of the detector is quite inexpensive the total cost is driven by the electronics and the photodetectors. The current baseline design allows the reuse of the *BABAR* iron structure with some modification that needs to be taken into account. Manpower and cost for engineering and module installation is based on the *BABAR* experience.

Electronics, Trigger, DAQ and Online: The cost for the Electronics and Trigger subsystems is estimated with a combination of scaling from the *BABAR* experience and from direct estimates. For items expected to be similar to those used in *BABAR* (such as infrastructure, high and low voltage or the L1 trigger) costs are scaled from *BABAR*. The same methodology is used to es-

timate EDIA and Labor costs for the Online system. However, some modifications based on “lessons learned” are applied. In particular, we are including costs for development work that, in our opinion, should have been centralized across sub-detectors in *BABAR* (but wasn’t) and work that should have been done upfront but was only done or completed as part of *BABAR* Online system upgrades.

The readout systems for which the higher data rates require redesigned electronics are estimated from the number of different components and printed circuit boards, and their associated chip and board counts. This methodology is also used for the possible new detectors (forward EMC, backward EMC, forward PID) and for the elements of the overall system architecture that are very different from *BABAR*.

The hardware cost estimates for the Online computing system (including the HLT farm) are, very conservatively, based on the current prices of hardware necessary to build the system, with the assumption that Moore’s Law will result in future systems with the same unit costs but higher performance. This is justified by our observation that for COTS components, constraints from system design, topology and networking are more likely to set minimum requirements for the *number* of devices than for the per-device performance.

Transportation, installation, and commissioning: Installation and commissioning estimates, including disassembling and reassembling *BABAR*, are based on the *BABAR* experience, and engineering estimates use a detailed schedule of activities and corresponding manpower requirements. The transportation costs have been estimated from costs associated with disassembling and transporting *BABAR* components for dispersal, if they were not to be reused.

11.3 Schedule

The detector construction schedule is shown in Fig. 48. The construction starts with design finalization and a technical design report, after which the fabrication of the detector subsystems

can proceed in parallel. At the same time the *BABAR* detector is disassembled, transported to the new site, and reassembled. The detector subsystems will be installed in sequence. An extended detector commissioning period, including a cosmic ray run, will follow to ensure proper operation and calibration of the detector. The total construction and commissioning time is estimated to be a little over five years.

References

- [1] Euro Inflation Rates, <http://www.ecb.int/stats/prices/hicp/html/index.en.html>.
- [2] NASA Inflation Calculator, <http://cost.jsc.nasa.gov/inflation/nasa/inflateNASA.html>.
- [3] Federal Reserve Foreign Exchange Rates, <http://www.federalreserve.gov/releases/g5a/>.

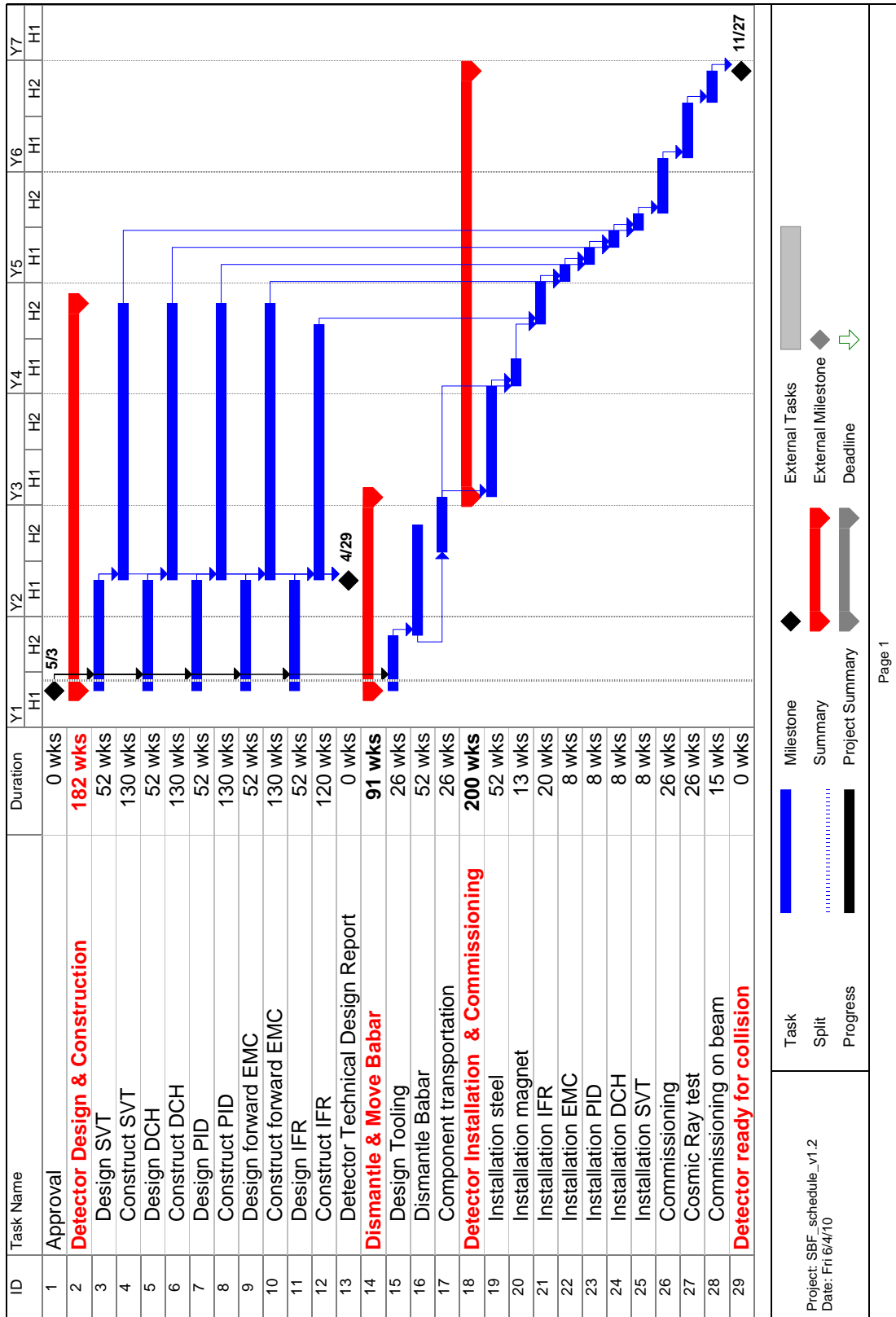


Figure 48: Schedule for the construction of the SuperB detector.